

Dissertation  
submitted to the  
Combined Faculties for the Natural Sciences and for Mathematics  
of the Ruperto-Carola University of Heidelberg, Germany  
for the degree of  
Doctor of Natural Sciences

Put forward by  
Dipl.-Phys. Mathias Gergely  
Born in Mannheim, Germany  
Oral examination: 2nd November 2011



# Snow Characterization by Optical Properties

Referees:

Prof. Dr. Kurt Roth

Prof. Dr. Bernd Jähne



**Charakterisierung von Schnee anhand der optischen Eigenschaften** Die Schneemikrostruktur ist entscheidend für den Strahlungstransport und für mechanische Wechselwirkungen innerhalb der Schneedecke und an der Oberfläche. Das Ziel dieser Arbeit ist es zu bestimmen, inwieweit Strahlungstransport und die tatsächliche 3D Mikrostruktur von Schnee vereinfacht werden können, um den Strahlungstransport immer noch hinreichend zu beschreiben. Die Auswertung konzentriert sich auf die optischen Eigenschaften Reflexions- und Transmissionsgrad für nahe Infrarotstrahlung sowie die Mikrostrukturparameter spezifische Oberfläche (entspricht der Schneekorngröße) und Dichte. Drei verschiedene Konzepte für den Strahlungstransport werden untersucht. Sie zeichnen sich aus durch (i) die Annahme einer gleichwertigen Mikrostruktur bestehend aus einer zufälligen Ansammlung von Eiskugeln mit derselben spezifischen Oberfläche und Dichte wie von der tatsächlichen Mikrostruktur, (ii) Raytracing angewandt auf die tatsächliche und gleichwertige Mikrostruktur und (iii) eine asymptotische Lösung für unendlich ausgedehnte Schneeböcke basierend auf der gleichwertigen Mikrostruktur. Die Reflexionsmessungen können innerhalb der natürlichen Variabilität des Schnees von 18% erklärt werden, wenn Modell (i) und (ii) kombiniert werden und die genaue Geometrie des kompakten Messinstruments berücksichtigt wird. Die Transmissionsmessungen von natürlichem Schnee stimmen gut mit den Ergebnissen für die Modelle (i) und (ii) überein. Lediglich der Transmissionsgrad von künstlich hergestelltem Schnee kann nicht durch Modell (i) wiedergegeben werden. Die Ergebnisse zeigen, dass spezifische Oberfläche und Dichte die beiden entscheidenden Eigenschaften für den Strahlungstransport in Schnee sind. Schließlich wird noch eine kombinierte hochauflösende Messmethode vorgestellt, mit der diese beiden Mikrostrukturparameter im Feld anhand eines Schneeprofilfotos bestimmt werden können.

**Snow characterization by optical properties** Snow microstructure is crucial for radiative transfer and mechanical interactions inside the snow cover and at the snow surface. The aim of this thesis is to determine which simplifications to general radiative transfer theory and to the true 3D snow microstructure can be assumed to still guarantee an adequate description of radiative transfer in snow. The analysis focuses on the optical properties reflectance and transmittance at near-infrared wavelengths and on the snow microstructural parameters specific surface area (equivalent to snow grain size) and density. Three different approaches to radiative transfer are analyzed. They are characterized by (i) assuming an equivalent microstructure of a random collection of ice spheres with the same specific surface area and density as the true microstructure, (ii) ray tracing applied to the true microstructure or the equivalent microstructure and (iii) an asymptotic solution for infinite snow blocks of the equivalent microstructure. Reflectance measurements can only be explained within the natural snow variability of 18% by a combination of models (i) and (ii) if the exact geometry of the compact measuring tool is implemented. Transmittance measurements of natural snow agree well with results for approach (i) and (ii). Only transmittance of highly anisotropic machine-made snow cannot be described by model (i). The results show that specific surface area and density are the two crucial properties that determine radiative transfer in snow. Finally, a combined high-resolution measurement method of these two microstructural parameters in the field is presented based on snow-profile photography.



# Contents

<b>1</b>	<b>Introduction</b>	<b>1</b>
1.1	Snow . . . . .	1
1.2	Quantitative measurement methods of snow microstructure . . . . .	4
1.2.1	Micro-computed tomography (micro-CT) . . . . .	4
1.2.2	Optical measurement methods . . . . .	5
1.3	Goals and outline . . . . .	7
<b>2</b>	<b>The Radiative Transfer Equation (RTE)</b>	<b>9</b>
2.1	Scattering . . . . .	11
2.2	Absorption and extinction . . . . .	12
2.3	Emission . . . . .	14
<b>3</b>	<b>Modeling Radiative Transfer in Snow</b>	<b>17</b>
3.1	Approximating snow microstructure by equivalent ice spheres . . . . .	18
3.2	Discrete-ordinate-method radiative transfer (DISORT) . . . . .	22
3.2.1	Single-scattering properties . . . . .	22
3.2.2	Multiple-scattering radiative transfer solution . . . . .	23
3.3	Ray tracing . . . . .	24
3.3.1	Monte Carlo radiative transfer based on micro-CT (CTMC) . . . . .	25
3.3.2	FRED: an optical engineering software based on 3D CAD . . . . .	27
3.4	Asymptotic flux extinction (AFE) . . . . .	28
3.5	Model results for five real snow samples . . . . .	30
3.5.1	Snow sample microstructural characterization . . . . .	30
3.5.2	Particle- and pore-level radiative properties . . . . .	31
3.5.3	Macroscopic snow-slab radiative properties . . . . .	37
3.5.4	First conclusions and outlook . . . . .	46
<b>4</b>	<b>InfraSnow: Diffuse NIR Reflectance Measurements to Determine Snow Grain Size (OED)</b>	<b>47</b>
4.1	Design requirements and realization . . . . .	48
4.2	Reflectance calibration . . . . .	50
4.3	Reflectance measurements and analysis . . . . .	50
4.3.1	Measurement variability for non volume-scattering materials . . . . .	51
4.3.2	Measurement variability for snow . . . . .	52
4.3.3	Comparison between measurements and models for snow . . . . .	53
4.4	Conclusions and outlook . . . . .	59
<b>5</b>	<b>Diffuse NIR Transmittance Measurements of Snow</b>	<b>63</b>

5.1	Measurement method and experimental setup . . . . .	64
5.2	Measurement results and analysis . . . . .	69
5.2.1	Measurements vs. DISORT and AFE models . . . . .	69
5.2.2	Measurements vs. CTMC model . . . . .	73
5.3	Conclusions . . . . .	74
<b>6</b>	<b>Outlook: Reflectance and Translucent Snow-Profile Photography</b>	<b>77</b>
6.1	Measurement method and experimental setup . . . . .	77
6.1.1	Snow OED measurement by NIR reflectance photography . . . . .	77
6.1.2	Snow density measurement by translucent snow-profile photography	79
6.2	Results and analysis of one Antarctic snow profile . . . . .	82
6.3	Conclusions . . . . .	85
<b>7</b>	<b>Summary</b>	<b>87</b>
<b>A</b>	<b>Snow Characterization by Facet Number and Size from Snow-Pit Wall Photographs</b>	<b>93</b>
A.1	Introduction . . . . .	93
A.2	Snow-pit wall photography . . . . .	94
A.2.1	Background . . . . .	94
A.2.2	Method . . . . .	94
A.3	Test results . . . . .	95
A.4	Conclusions and outlook . . . . .	99
<b>B</b>	<b>Bibliography</b>	<b>101</b>

# List of Figures

1.1	Snow precipitation crystals and snow on the ground . . . . .	1
1.2	Snow-profile measurements . . . . .	3
2.1	Fundamental effects of radiative transfer theory . . . . .	10
2.2	Henyey-Greenstein phase function . . . . .	12
2.3	Ice refractive index . . . . .	13
3.1	Micro-CT scans of 6 snow samples . . . . .	19
3.2	Mean curvature histograms of 6 snow samples . . . . .	21
3.3	DISORT geometry . . . . .	24
3.4	Possible FRED geometry . . . . .	28
3.5	AFE solution geometry . . . . .	29
3.6	Micro-CT scans of 5 snow samples for radiative transfer calculations . . .	32
3.7	Scattering coefficients for 5 snow samples . . . . .	33
3.8	Extinction coefficients for 5 snow samples . . . . .	35
3.9	Phase functions for 5 snow samples . . . . .	36
3.10	Reflectance and transmittance for 5 snow samples . . . . .	38
3.11	Difference DISORT-to-CTMC model in reflectance and transmittance . .	40
3.12	Comparison CT-IOSS-DISORT for 2 snow types . . . . .	42
3.13	Comparison AFE- vs. DISORT-calculated transmittance and reflectance .	45
4.1	InfraSnow reflectance measurement principle . . . . .	49
4.2	InfraSnow top and bottom view . . . . .	49
4.3	InfraSnow reflectance calibration . . . . .	50
4.4	InfraSnow results for non volume-scattering materials . . . . .	51
4.5	InfraSnow measurement variability for snow . . . . .	52
4.6	InfraSnow measurements, AFE and DISORT results for 4 snow blocks . .	54
4.7	Penetration depth for 2 snow types and NIR wavelengths . . . . .	55
4.8	InfraSnow model visualization and calibration in FRED . . . . .	56
4.9	InfraSnow measurements, FRED and DISORT results for 4 snow blocks .	57
4.10	InfraSnow density effect by FRED model . . . . .	59
5.1	Transmittance measurement principle . . . . .	65
5.2	Overview of transmittance measurement setup . . . . .	68
5.3	Example of raw transmittance spectra . . . . .	68
5.4	Transmittance measurements compared to AFE and DISORT models . . .	71
5.5	Boundary effect of snow thickness . . . . .	72
5.6	Micro-CT scans of 3 snow samples . . . . .	73

5.7	Transmittance measurements compared to CTMC and DISORT models . . . . .	74
6.1	NIR reflectance-photography setup . . . . .	78
6.2	NIR photography: snow OED vs. reflectance . . . . .	79
6.3	Transmittance analysis at NIR and visible wavelengths for 7 snow slabs . . . . .	80
6.4	Reflectance and translucent snow-profile photography principle . . . . .	81
6.5	Correlation between snow density, OED and transmittance . . . . .	82
6.6	Snow-profile normalized intensity images of reflected and transmitted light . . . . .	83
6.7	OED and density along one vertical snow-profile line . . . . .	84
A.1	Experimental setup for snow-pit wall photography . . . . .	94
A.2	Micro-CT scan of depth hoar with highlighted facets . . . . .	96
A.3	Micro-CT scans of samples used for snow-pit wall photography . . . . .	96
A.4	Highlight area histograms for snow-pit wall photography . . . . .	98

# List of Tables

3.1	Comparison OED vs. CED for 6 snow samples . . . . .	20
3.2	Classification of 5 snow samples for radiative transfer calculations . . . . .	31
3.3	Density, SSA and OED for 5 snow samples . . . . .	31
3.4	Radiative transfer modeling results for 5 snow samples . . . . .	43
4.1	InfraSnow snow samples characterization . . . . .	53
5.1	Overview of samples used for transmittance measurements . . . . .	70
5.2	Comparison transmittance measurements vs. DISORT calculations . . . . .	72
A.1	Snow properties of samples used for snow-pit wall photography . . . . .	97
A.2	Micro-CT facet analysis . . . . .	97
A.3	Highlight analysis of snow-pit wall photograph . . . . .	97

# Notation

## Abbreviations

AFE	Asymptotic flux extinction
CAD	Computer-aided design
CED	Curvature-equivalent grain size
CT	Computed tomography
CTMC	CT-based Monte Carlo radiative transfer
def,defII	Decomposing and faceted snow samples · and II
DF	Decomposing and fragmented precipitation particles
DH	Depth hoar snow
dh,dhII	Depth hoar snow sample · and II
DISORT	Discrete-ordinate-method radiative transfer
DOI	Diffuse optical imaging
ds	Decomposing snow sample
FC	Faceted snow crystals
FOV	Field of view
GO	Geometrical optics
IOSS	Identical overlapping semi-transparent spheres
lmf,mf	Large and small melt forms snow sample
mI,mII	Metamorphosed snow sample I and II
MF	Melt snow forms
MM	Machine-made snow
mm	Machine-made snow sample
NIR	Near-infrared

OED	Optical equivalent grain size
rI,rII	Rounded snow sample I and II
REV	Representative elementary volume
rf	Rounded and faceted snow sample
RG	Rounded snow grains
rg	Rounded grains snow sample
RTE	Radiative transfer equation
SSA	Specific surface area
wns	Wet and refrozen new snow sample
ws	Wet snow sample

**Lowercase Greek Symbols**

$\beta$	Extinction coefficient [ $\text{m}^{-1}$ ]
$\varepsilon$	Porosity [-]
$\theta$	Polar angle [-]
$\kappa$	Absorption coefficient [ $\text{m}^{-1}$ ]
$\kappa_t$	Emission coefficient [ $\text{m}^{-1}$ ]
$\lambda$	Wavelength [m]
$\mu$	Cosine of polar angle $\cos(\theta)$ [-]
$\xi$	Normalized 2-norm [-]
$\rho$	Mass density [ $\text{kg m}^{-3}$ ]
$\sigma_s$	Scattering coefficient [ $\text{m}^{-1}$ ]
$\tau$	Normal optical depth [-]
$\varphi$	Azimuth angle [-]
$\omega$	Albedo [-]

**Uppercase Greek Symbols**

$\Theta$	Scattering angle [-]
$\Phi$	Phase function [-]

$\Phi_{\text{HG}}$  Henyey-Greenstein phase function [–]

$\Omega$  Solid angle [–]

**Lowercase Roman Symbols**

$c$  Speed of light [ $\text{m s}^{-1}$ ]

$d$  Sphere diameter [m]

$g$  Phase function asymmetry parameter [–]

$h$  Planck constant [J s]

$k_{\text{B}}$  Boltzmann constant [ $\text{J K}^{-1}$ ]

$k$  Imaginary part of refractive index [–]

$k_{\text{ext}}$  Asymptotic flux extinction coefficient  $\text{m}^{-1}$

$\hat{\mathbf{n}}$  Unit vector [–]

$n$  Real part of refractive index [–]

$n_{\text{V}}$  Number density (number per volume) [ $\text{m}^{-3}$ ]

$q$  Radiative flux [ $\text{J s}^{-1} \text{m}^{-2}$ ]

$\mathbf{r}$  Position vector [m]

$r$  Radius [m]

$s$  Length or thickness [m]

$t$  Time [s]

$x$  Size parameter [–]

$z$  Distance in  $z$ -direction [m]

**Uppercase Roman Symbols**

$\mathbf{A}$  Vector field

$A$  Area [ $\text{m}^2$ ]

$A_0$  Specific surface area [ $\text{m}^{-1}$ ]

$B$  Planck function for thermal emission [ $\text{J s}^{-1} \text{m}^{-3}$ ]

$H$  Mean curvature [ $\text{m}^{-1}$ ]

$I$  Specific intensity [ $\text{J s}^{-1} \text{m}^{-3}$ ]

$I_t$	Specific intensity of thermal emission [ $\text{J s}^{-1} \text{ m}^{-3}$ ]
$R$	Reflectance [-]
$T$	Temperature [K]
$Tr$ (or $T_{type}$ )	Transmittance (calculated with model <i>type</i> )[-]



# 1 Introduction

## 1.1 Snow

Snow forms in the atmosphere by cloud-droplet freezing induced by freezing nuclei and subsequent deposition of water vapor. Depending on the degree of water vapor supersaturation and temperature snow crystals of different shape and size develop (Figure 1.1(a)). The most prominent of these shapes are stellar dendrites, which resemble stars with a hexagonal symmetry. While the principles of radiative transfer described in Chapters 2 and 3 also apply to snow in the atmosphere the subject of this thesis is snow on the ground. The physical processes that determine the snowpack formation on the ground differ starkly from the processes that drive snow formation in the atmosphere.

Once the snow accumulates on the ground or on top of an already present snowpack the snowpack densifies due to gravity, called settlement, originally separated snowflakes sinter and the original shapes of the snowflakes change according to the present environmental conditions (Figure 1.1(b)). These conditions are determined by the current solar radiation,

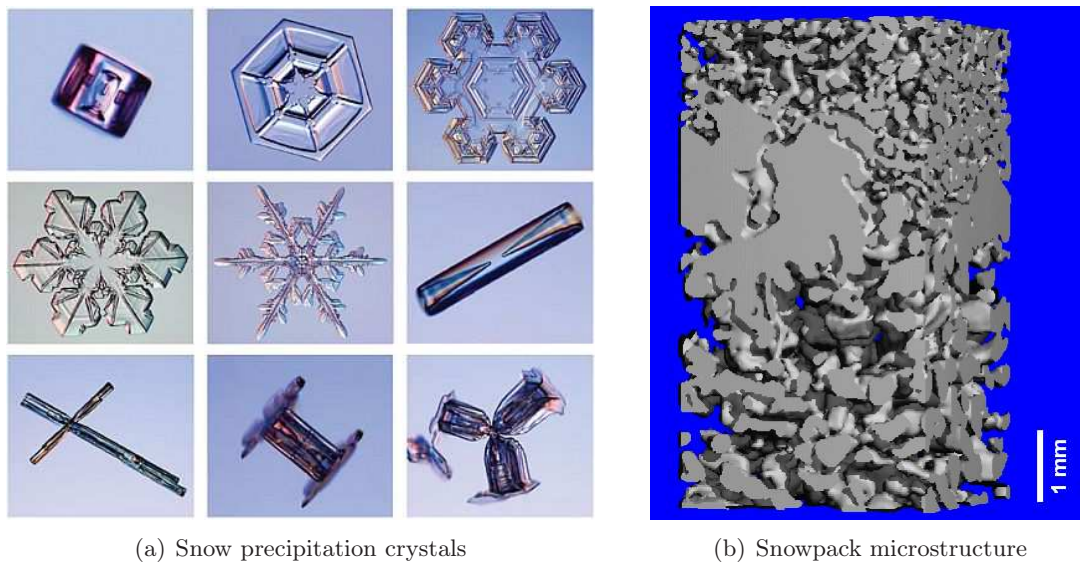


**Figure 1.1:** What does snow look like? **(a)** Various snowflake shapes in the atmosphere. The largest extension of each snowflake is between 50 and 150  $\mu\text{m}$ . Dendritic snowflakes can reach up to several mm. Photos taken by K. G. Libbrecht, snowcrystals.com. **(b)** Snow on the ground. Ice matrix is shown in grey on blue background, air phase is transparent. Three distinct regions can be identified: (from the top down) wind-pressed small-grained rounded snow, large melt-freeze clusters and weak faceted snow. Image adapted from M. Schneebeli.

wind speed and direction as well as current temperature and temperature differences inside the snowpack. This snow metamorphism starts instantly and continues until the snow melts.

Snow consists mainly of ice and air. Due to sintering and if the air fraction is larger than about 15% both ice matrix and air phase are continuous making snow on the ground a bicontinuous material with a complex 3D ice structure (Good, 1987; Coléou *et al.*, 2001). Other constituents of snow include aerosols, soot, sand or algae. The volume fraction of these impurities is usually very small. Nevertheless, they can become significant as can already be seen by eye when snow takes on a grayish color or turns black next to roads due to a high soot concentration. Other examples include layers of sandy snow where storms can transport and deposit substantial amounts of sand or snow algae which can cause the snow to take on various hues.

During metamorphism regions within the snowpack can undergo transformations to rounded ice structures, shapes with planar faces, called facets, or large crystal clusters. The characteristic ice structure size, commonly called grain size, usually varies from a tenth of a mm to several mm. Fierz *et al.* (2009) compiled a classification of all snow types and various snow properties. Snow metamorphism is driven by temperature, temperature gradient and the minimization of the interfacial surface free energy which all determine the water vapor diffusion field (Schneebeli and Sokratov, 2004; Kaempfer and Schneebeli, 2007; Pinzer, 2009). Due to the high homologous temperature of ice, i.e. ice generally exists close to its melting point at 0°C, snow sinters and the ice structure changes very rapidly. This leads to a highly-structured snowpack with predominantly horizontal layers of similar snow microstructure within the same layer (Colbeck, 1991). In general, the scale of spatial variability ranges from few mm to dm (Schneebeli *et al.*, 1999; Harper and Bradford, 2003). Examples for a high variability include a thin crust (see melt-freeze clusters in the center of Figure 1.1(b)), a thin layer of surface hoar or refrozen water which originally infiltrated into the snow cover in narrow preferentially vertical flow paths.

Snowpack structure and snow microstructure define the radiative and mechanical properties of the present snowpack. The radiative properties determine the albedo and hence the remitted fraction of sunlight as well as the energy absorption inside the ice matrix and thus the onset and extent of snowmelt (Wiscombe and Warren, 1980; Aoki *et al.*, 2000; Painter and Dozier, 2004; Flanner and Zender, 2006; Warren *et al.*, 2006; Kuipers Munneke *et al.*, 2009; Gardner and Sharp, 2010). Seasonal snow covers up to a third of the Earth's land surface and perennial glaciers and ice-sheets cap another 10%. So, snow on the ground contributes substantially to the radiation and overall energy balance between the Earth and its atmosphere. The differences in snow microstructure account for a possible spectral remission range from 30 to 95% of incoming solar radiation for a snowpack without significant impurity content (Wiscombe and Warren, 1980). Gardner and Sharp (2010) calculated broadband albedos of 40% to 90% from optical properties of white ice, dirty and pure snow. The average remission across the entire Earth is only 30%. Thus, an adequate description of the snow microstructure is important for global and regional climate models in order to calculate a reasonable energy balance (Roesch *et al.*, 2002). As an example for mechanical properties, friction on the snow surface and inside the snowpack determines the gliding characteristics of a ski (Colbeck, 1992; Fauve *et al.*, 2008; Theile *et al.*, 2009) and avalanche fracture characteristics

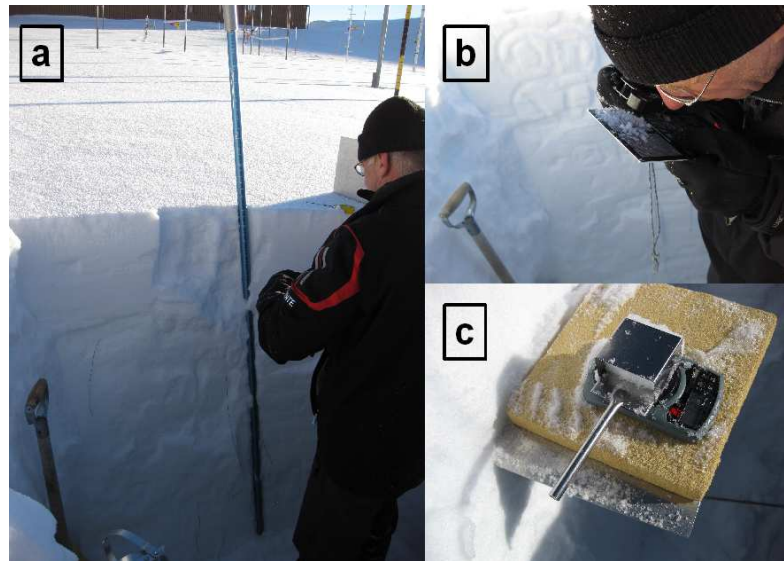


**Figure 1.2:** Snow-profile analysis in the field. (a) Snow-pit vertical wall prepared for analysis. (b) Estimating mean snow grain size and predominant grain shape by visual inspection of snow crystals on a grid card with a magnifying lens. The snow crystals have been scratched off the snow-pit wall with the card and thus are fragments of the true snow microstructure (Fig 1.1(b)). (c) Density measurement by weighing a known snow volume, which has been cut from the snow-pit wall by a small scoop of  $6 \times 5.5 \times 2 \text{ cm}^3$ .

(Schweizer *et al.*, 2003; Reiweger *et al.*, 2009), respectively. Here, snow microstructure and more specifically density, hardness, snow type and a characteristic size are crucial parameters for the frictional force at the snow-to-ski interface and within a snow layer or at a snow layer interface.

Traditionally, snow microstructural properties have been estimated by hand measurements along a snow-pit wall (illustrated in Figure 1.2): Snow type and grain size, hardness, wetness and density are estimated by visual inspection, hand tests and weighing. These are ‘guesses’ rather than quantitative measurements as the results depend heavily on the observer (Pielmeier and Schneebeli, 2003; Painter *et al.*, 2007). A great experience is needed for a usable interpretation of the gathered data. And even results of experienced observers usually differ significantly from one another. The results from these methods are often sufficient for qualitative statements about snowpack stability and snow water content. However, more rigorous and high-resolution scientific measurement methods are needed to understand the underlying physical processes of metamorphism and radiative transfer and correlate them to the snow microstructure. For example, visually determined snow grain size does not correlate with the optical equivalent grain size (OED) (defined in Section 1.2.2) that can be used as a crucial input parameter for modeling reflectance of snow (Painter *et al.*, 2007).

## 1.2 Quantitative measurement methods of snow microstructure

In recent years, several scientific methods have been developed to analyze snow microstructural parameters. *Schneebeli et al.* (1999) measured the force needed to break ice structures within the snow by a high-resolution penetrometer. They were able to correlate the penetration resistance to snow-type characteristics for measurements in the laboratory and the field. *Legagneux et al.* (2002) measured snow specific surface area (SSA,  $A_0$ ), i.e. the ratio of ice surface area to ice volume in snow, by methane adsorption at 77 K. In the following section another quantitative measurement method will be explained which is used extensively during this thesis: micro-computed tomography. Then a short overview of current optical methods to analyze various materials and snow microstructure in particular will be given.

### 1.2.1 Micro-computed tomography (micro-CT)

A well-established method to measure snow microstructural properties is micro-computed tomography (micro-CT) (*Coléou et al.*, 2001; *Brzoska et al.*, 2001; *Flin et al.*, 2004; *Schneebeli and Sokratov*, 2004; *Kaempfer and Schneebeli*, 2007; *Kerbrat et al.*, 2008). Here, small snow samples of several  $\text{mm}^3$  to  $\text{cm}^3$  can be observed non-intrusively by X-ray absorption tomography. The output is a high-resolution 3D image of the actual snow microstructure (data of one snow sample is visualized in Figure 1.1(b)), which can then be used for further analysis. The principle is the same as for medical X-ray tomography with the main difference that for micro-CT of snow the sample is rotated instead of the detector. The two phases ice and air are separated by segmenting the greyscale histograms of the tomograms. A threshold is chosen manually or by fitting two Gaussian curves, representing the two phases, to the greyscale histogram and calculating the intersection point.

The X-ray source of the used Scanco  $\mu\text{CT}$  40 computer tomograph emits at 45 kV acceleration voltage. A  $2048 \times 256$  element CCD detector captures the absorption signal. The resolution depends on the scanned snow volume and is chosen according to the measured snow types for this study. For fine-grained snow the maximum resolution of  $6 \mu\text{m}$  is used. For other snow samples the voxel size is 10 to  $15 \mu\text{m}$ . Using a Scanco  $\mu\text{CT}$  80 computer tomograph with a resolution of  $18 \mu\text{m}$  *Kerbrat et al.* (2008) showed that only fresh snow contains features which cannot be adequately observed by micro-CT at this resolution. *Coléou et al.* (2001) and *Kaempfer et al.* (2005) found representative elementary volumes (REVs) for snow micro-CT measurements of density between  $1.25^3$  and  $2.5^3 \text{mm}^3$  depending on snow coarseness. *Kaempfer et al.* (2005) determined an REV for tortuosity in snow of about  $5^3 \text{mm}^3$ .

The  $\mu\text{CT}$  40 is a desktop scanner inside a cold laboratory at temperatures between  $-5$  and  $-20^\circ\text{C}$  to facilitate snow measurements at various temperatures. With this setup snow samples can be stored in a separate cold laboratory or a freezer at the desired temperature conditions: constant temperature, a temperature variation in time or a spatial temperature gradient within the sample. For the measurement time of several hours, depending on the size of the captured sample volume, the samples are placed inside the micro-CT and afterwards returned or subjected to other environmental conditions.

Thus, the evolution of the snow microstructure can be tracked at a high temporal and spatial resolution under controlled conditions without destroying the original sample. This is the great advantage compared to other high-resolution methods like thin sections and microscopy. However, micro-CT is restricted to a laboratory and an expensive and time-demanding measurement technique.

### 1.2.2 Optical measurement methods

Optical measurement methods are well-established in diverse areas of research as they offer fast quantitative results by affordable and portable measurement tools. Both visible and near-infrared (NIR) light is used. NIR offers additional and often crucial information on the observed materials which is not evident from a visual inspection. Diffuse reflectance and transmittance spectroscopy plays an important role in quality control for industrial and agricultural production (*McGlone and Martinsen, 2004; Baptista et al., 2008; Gaston et al., 2010*). Furthermore, NIR diffuse reflectance can be used to discriminate between original and counterfeit goods like e.g. medicines (*Moffat et al., 2010*).

In most applications of traditional NIR spectroscopy measured reflectance or transmittance is compared to a great number of calibration measurements which have been performed in advance. Thus, reflectance or transmittance can be correlated to the desired material property. Generally, the calibration measurements are time-consuming and expensive. A more desirable method is to directly correlate measurement results to modeled results. So, time and costs of a usage-specific calibration process can be minimized or skipped altogether.

Diffuse optical imaging (DOI) in medical application aims at correlating diffuse NIR reflectance or transmittance with the concentration of red and white blood cells in body tissue (*Arridge, 1999; Boas et al., 2001; Gibson et al., 2005*). The concentration of blood cells is an indicator for the presence of a tumor or internal bleeding while the ratio of red to white blood cells shows how well an organ is supplied with oxygen. Diffusion theory is employed to explain the detected reflected and transmitted light intensity distribution and derive absorption and scattering properties of the probed tissue.

For snow a similar approach, i.e. measurements explained by a radiative transfer model, has been successful in determining snow OED, a crucial microstructural parameter (*Matzl and Schneebeli, 2006; Painter et al., 2007; Gallet et al., 2009; Arnaud et al., 2011*). OED is the diameter of a sphere with the same SSA as the true 3D snow microstructure. This leads to the relation

$$\text{OED} = \frac{6}{\text{SSA}} . \quad (1.1)$$

Typical OEDs for real snow range from about 100  $\mu\text{m}$  to 1 mm. The lower part of the OED range corresponds to fine-grained fresh snow and the higher end to large clusters of melted and refrozen snow. So, snow grain size is much bigger than all optical wavelengths which are used for the analysis of snow in this thesis.

*Matzl and Schneebeli* (2006) developed a spatially-continuous measurement method based on photography with a resolution of a few mm. *Painter et al.* (2007) used contact spectroscopy of a snow-pit wall with a stable halogen light source and *Gallet et al.* (2009) built an integrating sphere setup with collimated illumination of small snow samples

( $\sim 20 \text{ cm}^3$ ) to deduce OED from snow reflectance. The latter two methods are point measurements with a spatial resolution of several cm. *Arnaud et al.* (2011) developed a method based on *Gallet et al.* (2009) to measure SSA profiles along a bore-hole inside the snow cover down to  $\sim 20 \text{ m}$ . They all share a common principle: Reflectance is measured at NIR wavelengths, where impurities have only a weak influence on the reflectance of snow (*Warren and Wiscombe*, 1980). At all these wavelengths and for a sufficiently thick snow block there exists a strong correlation between reflectance and OED according to multiple-scattering radiative transfer theory (*Wiscombe and Warren*, 1980; *Grenfell and Warren*, 1999; *Neshyba et al.*, 2003; *Zhou et al.*, 2003a; *Grenfell et al.*, 2005). *Domine et al.* (2006) found the highest correlation coefficients  $\approx 1$  near  $1.5\mu\text{m}$ . Nevertheless, OED has also been measured successfully at shorter wavelengths and by analyzing a continuous spectral region within the entire NIR spectrum as demonstrated by *Matzl and Schneebeli* (2006); *Painter et al.* (2007); *Gallet et al.* (2009).

Recent reflectance calculations by *Xie et al.* (2006) and *Picard et al.* (2009) also show a significant dependence on grain shape. In all cited works snow is considered as a collection of ice particles consisting of only one specific geometric grain shape like spheres, cubes or cylinders with the same OED. In contrast to the simulation results by *Xie et al.* (2006) and *Picard et al.* (2009), *Gallet et al.* (2009) found the effect of grain shape to be of minor importance for their reflectance experiments with natural snow.

A first approach to account for the true 3D snow microstructure was introduced in radiative transfer studies based on micro-CT (*Kaempfer et al.*, 2007; *Bänninger et al.*, 2008). In both studies ray tracing is used to model radiative transfer. *Kaempfer et al.* (2007) already used 3D tomography images of the snow microstructure as input for their reflectance and transmittance calculations. However, those studies are limited to relatively small volumes due to the great number of computationally-intensive scattering calculations that have to be performed at every ice-to-air interface for every traced light ray within the snow volume. Besides, they do not yield volumetric radiative properties like extinction coefficients or scattering phase functions, which are crucial for modeling radiative transfer in macroscopic snow samples effectively.

In addition to reflectance measurements, visible-light transmittance in snow has been used to analyze the stratigraphy of natural snowpacks in translucent snow profiles (*Good et al.*, 1991; *Harper and Bradford*, 2003). Here, a snow slab of a few cm thickness is backlit while a picture is taken of the front side. Different layers and inhomogeneities can be identified on the picture at a resolution of a few mm. Due to the combined influence of snow density, SSA and impurity content on visible-light transmittance no quantitative analysis of these translucent snow profiles has been successful so far.

Transmittance measurements at a high spectral resolution for visible and NIR light have been performed as well (*Beaglehole et al.*, 1998; *Meirolid-Mautner and Lehning*, 2004; *Warren et al.*, 2006). However, the results have not been used to derive snow microstructural parameters. *Warren et al.* (2006) derived ice absorption coefficients for visible light, and *Beaglehole et al.* (1998) focused on a general qualitative study of scattering parameters. *Meirolid-Mautner and Lehning* (2004) measured and calculated snow transmittance from 350 to 1050 nm in Greenland. They used hand measurements of grain size and density in the field as input to their model and introduced a scaling factor for grain size to fit their model to their measurements.

## 1.3 Goals and outline

The summary of the previous works in Section 1.2 raises two main questions with regard to snow characterization by optical properties in general:

- To what extent can radiative transfer theory and the true snow microstructure be simplified while still yielding an adequate description of radiative transfer in snow?
- Which microstructural properties of snow can be derived from optical measurements?

Specifically, the presented analysis focuses on the microstructural properties snow SSA (or OED by Equation 1.1) and density to describe radiative transfer in snow.

As snow optics is still a young and small area of research a better understanding of the correlation between snow microstructure and optical properties is paramount. This is the main goal of this thesis. To this end, radiative transfer models based on the true or an equivalent snow microstructure of OED ice spheres are compared for real snow samples and the agreement between reflectance and transmittance measurements and simulations for those models is analyzed.

In Chapter 2 the fundamental Radiative Transfer Equation (RTE) is introduced. Absorption, scattering and emission properties of the material are included in the RTE and explained briefly with examples of pure ice and air, the two non-scattering constituents of pure snow. To solve the RTE for snow several models are presented in Chapter 3: a widely-used radiative transfer code named DISORT, two different implementations of Monte-Carlo ray tracing and a simpler diffuse flux extinction approximation where all boundary effects due to the finite extension of a snow block are neglected. Radiative transfer calculation with those models are compared for 5 real snow samples. The topic of Chapter 4 is the InfraSnow device, a hand-held tool for fast snow reflectance measurements in the field. Transmittance measurements of real snow slabs are compared to simulations with the presented models in Chapter 5. The experiments are performed in the laboratory with diffuse light source and a spectrometer as detector. For the simulations of both Chapter 4 and 5 microstructural parameters are measured by micro-CT and then used as model input. Finally, Chapter 6 gives an outlook to combined high-resolution measurements of snow OED and density along a snow-pit wall by reflectance and transmittance photography in the field.

The Appendix A contains another investigation on optical characteristics of snow: First experiments are shown to correlate specular reflections on snow-pit wall photographs with snow facet number and facet size.



## 2 The Radiative Transfer Equation (RTE)

Research on radiation transport in scattering media consisting of a random collection of independently scattering particles dates back to the late 19th century. Traditionally, *Schuster* (1905) has been cited as the first who introduced a simple form of the fundamental equation to describe radiation transport in such media, the so-called radiative transfer equation (RTE). He investigated the effect of a scattering atmosphere on a stellar emission spectrum and concluded that scattering within the atmosphere could have a significant effect on the observed absorption and emission lines of a stellar spectrum. Since then the problem of radiative transfer in scattering atmospheres has been studied in various fields of research where radiation transport is crucial or where measurement methods based on radiative transfer can be useful.

Electromagnetic energy is written as  $I(\mathbf{r}, \hat{\mathbf{n}}, \lambda)d\lambda dt dA d\Omega$  with specific intensity  $I(\mathbf{r}, \hat{\mathbf{n}}, \lambda)$  of monochromatic radiation with wavelength  $\lambda$ . The radiation propagates in a time interval  $dt$  in the direction  $\hat{\mathbf{n}}$  confined to the solid angle  $d\Omega$  through the surface element  $dA$  normal to  $\hat{\mathbf{n}}$  and located at  $\mathbf{r}$ . A phenomenological approach to radiative transfer theory in a homogeneous, scattering medium by ensuring conservation of electromagnetic energy then leads to the RTE for the specific intensity (e.g. derived from *Chandrasekhar*, 1950)

$$\begin{aligned} \hat{\mathbf{n}} \cdot \nabla I(\mathbf{r}, \hat{\mathbf{n}}, \lambda) = & - \underbrace{\beta(\lambda)I(\mathbf{r}, \hat{\mathbf{n}}, \lambda)}_{\text{Extinction by scattering and absorption}} \\ & + \underbrace{\int_{\Omega} d\hat{\mathbf{n}}' \sigma_s(\lambda)\Phi(\hat{\mathbf{n}}, \hat{\mathbf{n}}', \lambda)I(\mathbf{r}, \hat{\mathbf{n}}', \lambda)}_{\text{Scattering enhancement in direction } \hat{\mathbf{n}}} \\ & + \underbrace{\kappa_t(\lambda)B(\lambda, T(\mathbf{r}))}_{\text{Thermal emission}} . \end{aligned} \quad (2.1)$$

Here,  $\beta$ ,  $\sigma_s$  and  $\kappa_t$  are extinction, scattering and thermal emission coefficient, respectively. Assuming a homogeneous medium of randomly arranged scattering centers these coefficients are independent of position and direction. The directional dependence is included in the scattering phase function  $\Phi$ .  $B(\lambda, T(\mathbf{r}))$  is the Planck function for thermal emission. All fundamental characteristics of radiative transfer theory will be explained in detail in Sections 2.1 to 2.3. First, we will focus on a general explanation of the RTE and put it in the context of classical electrodynamics.

In Equation (2.1) the first term on the right-hand side specifies the extinction, i.e. the attenuation of radiation by both scattering out of the original direction  $\hat{\mathbf{n}}$  and absorption within the medium. Analogous to scattering, absorption can be characterized by an absorption coefficient  $\kappa$ . The integral over the solid angle specifies the radiation enhance-

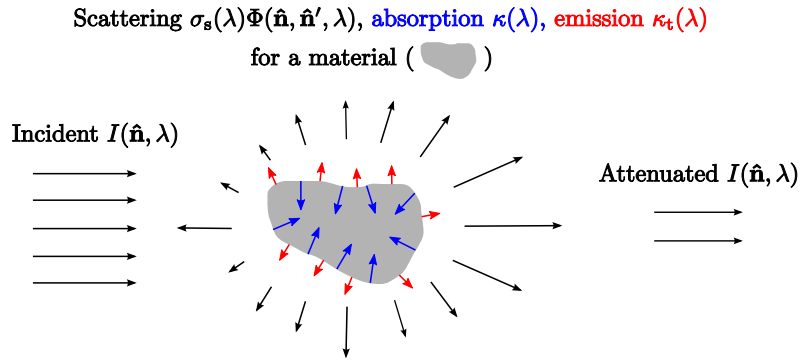


**Figure 2.1:** Sketch of the three fundamental effects of radiative transfer theory for a homogeneous scattering medium. This can be a single particle, a fixed or a random cluster of particles. Number and length of arrows represent the angular intensity distribution. The intricate radiation field inside the scattering medium is not shown, only the net effects on the incident radiation  $I(\hat{\mathbf{n}}, \lambda)$  in the far field of the scattering medium.

ment in direction  $\hat{\mathbf{n}}$  by scattering out of all directions  $\hat{\mathbf{n}}'$  into  $\hat{\mathbf{n}}$ . The third term represents the thermal emission according to the Planck distribution. Figure 2.1 illustrates these three fundamental effects of radiative transfer theory.

In this form the RTE (2.1) only accounts for the radiation intensity and does not include polarization effects and coherent scattering. While it can be generalized to also include polarization effects this phenomenological approach becomes increasingly shaky and confusing the more effects are included. It is therefore important to also look at the RTE in the context of classical electrodynamics. *Mishchenko* (2002) was the first to present a rigorous microphysical derivation of the vector RTE for non-emitting media from statistical electromagnetics. His approach starts with the electric field for an incoming plane wave or a slowly fluctuating monochromatic parallel beam of light. The Maxwell equations are the only governing laws of electromagnetic interaction. Instead of only analyzing the radiation intensity the Stokes vector is introduced composed of the four Stokes parameters to describe the intensity and polarization characteristics of electromagnetic radiation. Along with statistical averaging over all interaction events this naturally leads to the vector RTE which yields radiation intensity distribution as well as polarization and coherent scattering effects. An explanation of fundamental electromagnetic principles and a detailed derivation and analysis can also be found in *Mishchenko et al.* (2002) and *Mishchenko* (2008).

The derivation from the Maxwell equations is based on several assumptions: The analyzed medium consists of a homogeneous, transparent host medium and discrete finite scattering and absorbing particles of arbitrary shape; all thermal emission is ignored; electromagnetic scattering is assumed to be elastic, i.e. there is no frequency shift during scattering; all optical constants are assumed to be independent of the electric and magnetic fields; any changes in scattering-particle positions and reorientation occur on a time scale much larger than the inverse of the radiation frequency. While these assumptions might seem rather restrictive they are actually applicable to many radiative transfer problems, e.g. to dilute suspensions or atmospheric clouds and short-wave solar radiation.

For snow in particular, the most arguable assumption is to postulate a discrete random medium consisting of many dilute scattering particles, each of which is in the far-field zone of all other particles to guarantee independent scattering. As already illustrated in Figure 1.1(b) this is clearly not true for the bicontinuous snow microstructure. The importance of the exact snow microstructure will be discussed in Chapter 3. For now, it can be noted that the RTE can not only be understood by the principle of energy conservation but also be strictly derived from the fundamental principles of classical electrodynamics under the assumptions stated above. This should present a firm basis for using the RTE for radiative transfer problems of unpolarized visible and NIR radiation in Chapters 3 to 6. First however, the optical properties which were introduced in the RTE (2.1) are discussed in detail.

## 2.1 Scattering

Scattering is the process where electromagnetic radiation deviates from its original trajectory due to heterogeneities in the medium where the radiation propagates. Examples for such heterogeneities are interfaces between different materials like particles in a suspension, density fluctuations within the same medium or interfaces between crystals of the same material but different orientation.

In general, scattering depends on the position inside the scattering medium, incident and observation direction and radiation wavelength and polarization. Neglecting polarization effects in a homogeneous medium of randomly located and oriented scattering particles as it was assumed for the RTE (2.1) scattering is an effective material property and independent of position  $\mathbf{r}$ . Traditionally, the directional and wavelength dependence are written as a product  $\sigma_s(\lambda)\Phi(\hat{\mathbf{n}}, \hat{\mathbf{n}}', \lambda)$ . The scattering coefficient  $\sigma_s(\lambda)$  describes the attenuation of the radiation over a length  $ds$  due to scattering out of the original direction:

$$dI = -\sigma_s I ds . \quad (2.2)$$

The phase function  $\Phi(\hat{\mathbf{n}}, \hat{\mathbf{n}}', \lambda)$  specifies the angular distribution of the scattered radiation with the normalization condition

$$\int_{\Omega} d\hat{\mathbf{n}}' \Phi(\hat{\mathbf{n}}, \hat{\mathbf{n}}', \lambda) = 1 . \quad (2.3)$$

One phase function which has found wide use in radiative transfer problems is the Henyey-Greenstein distribution (*Henyey and Greenstein, 1941*)

$$\Phi_{\text{HG}}(\Theta, \lambda) = \frac{1}{4\pi} \frac{1 - g(\lambda)^2}{(1 + g(\lambda)^2 - 2g(\lambda) \cos(\Theta))^{3/2}} . \quad (2.4)$$

Here, the scattering angle  $\cos(\Theta) = \hat{\mathbf{n}} \cdot \hat{\mathbf{n}}'$  between incident and scattering directions  $\hat{\mathbf{n}}'$  and  $\hat{\mathbf{n}}$  is introduced for scattering which is independent of the azimuth angle. The asymmetry parameter  $g(\lambda)$  is defined as

$$g(\lambda) = \langle \cos(\Theta) \rangle = \int_{\Omega} d\Omega \cos(\Theta) \Phi(\Theta, \lambda) . \quad (2.5)$$

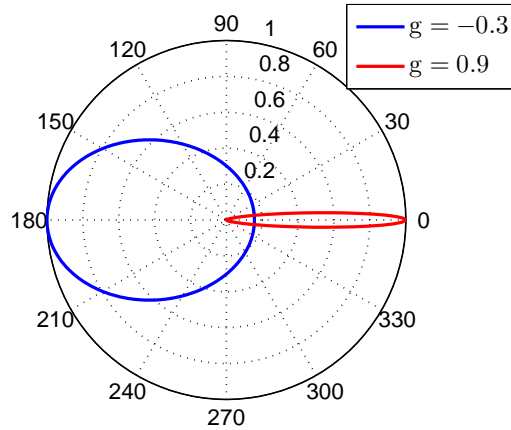


**Figure 2.2:** Polar plot of Henyey-Greenstein phase function against the scattering angle for two asymmetry parameters  $g$ . Plotted values are computed at an angular resolution of 0.01 and are normalized to the maximum of each of the two distributions.

Thus,  $g$  varies between 1 and  $-1$ , with the extreme values corresponding to complete forward and backward scattering, respectively. For isotropic scattering  $g = 0$ , i.e. the radiation is scattered in any direction with the same probability. Figure 2.2 shows the Henyey-Greenstein phase function for two values of  $g$ : One predominantly backward-scattering distribution with  $g = -0.3$  and one highly forward-scattering with  $g = 0.9$ .

In any scattering medium both radiation attenuation and enhancement are affected by scattering. In the RTE 2.1 scattering is included in the extinction term (see Section 2.2 for an explanation) and in the second term as enhancement. For extinction, the exact angular distribution of the scattered radiation is not important as the only interesting quantity is the net loss of radiation due to scattering out of the observation direction. So, the phase function does not appear in the extinction term. Scattering into the observation direction, however, can only be quantified correctly if the sum of all scattered radiation is reproduced. For non-isotropic scattering this requires a correct description of the complete angular distribution of scattering and thus the inclusion of the phase function in addition to the scattering coefficient.

For snow, scattering is the dominant effect of radiative transfer (Chapter 3). But, ice and air, i.e. both constituents of pure snow, exhibit no significant scattering for visible and NIR light. For both homogeneous materials  $\sigma_s \approx 0$  over this spectrum. Only the high number of interfaces between ice and air which are crossed by a light path turn snow into a highly-scattering material.

## 2.2 Absorption and extinction

In contrast to scattered radiation, absorbed radiation in a medium is completely removed from the incident radiation and not just attenuated due to redirection. Absorption is

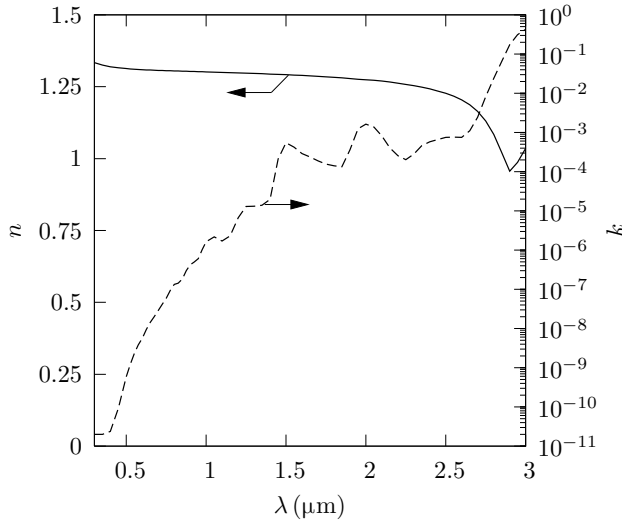


**Figure 2.3:** Real (solid line) and imaginary (dashed line) part of the refractive index of ice for visible, NIR to the start of thermal infrared wavelengths according to *Warren and Brandt (2008)*.

described analogous to Equation (2.2):

$$dI = -\kappa I ds . \quad (2.6)$$

This is known as the Lambert-Beer law. The absorption coefficient  $\kappa$  only depends on the radiation wavelength  $\lambda$  for homogeneous media. It is related to the complex refractive index  $n + ik$  by

$$\kappa = \frac{4\pi}{\lambda} k . \quad (2.7)$$

In air,  $\kappa \approx 0$  while for ice absorption is highly dependent on the radiation wavelength (Figure 2.3). The imaginary part of the refractive index shows a strong increase with wavelength in the visible and NIR part of the spectrum from about 0.5 to 1.5  $\mu\text{m}$ . Finally, in the thermal infrared ice absorbs very strongly and becomes ‘black’ in contrast to its transparent appearance at visible wavelengths. Hence, all absorption in snow is due to absorption inside the ice matrix.

As shown in Equation (2.1) absorption and scattering are often combined to yield the total extinction coefficient

$$\beta(\lambda) = \kappa(\lambda) + \sigma_s(\lambda) . \quad (2.8)$$

The albedo  $\omega$  defines the ratio of scattering to total extinction:

$$\omega(\lambda) = \frac{\sigma_s(\lambda)}{\beta(\lambda)} . \quad (2.9)$$

For a non-scattering medium like pure ice  $\omega = 0$ . Snow, on the other hand, has an albedo close to one for visible light. This is easily seen by the high reflectance and thus only low absorption of sunlight for a fresh snow cover.

## 2.3 Emission

All materials which are not at a temperature of 0 K emit a continuous spectrum of electromagnetic radiation. The specific intensity distribution of this thermal emission  $I_t$  is given by the product of thermal emissivity  $\frac{\kappa_t(\lambda)}{\beta(\lambda)}$  and isotropic Planck function for black-body radiation

$$B(\lambda, T) = \frac{2hc^2}{\lambda^5} \frac{1}{e^{hc/\lambda k_B T} - 1} . \quad (2.10)$$

According to Kichhoff's law of thermal radiation emissivity is equal to absorptivity in thermal equilibrium and thus  $\kappa_t = \kappa$ . For scattering materials and the definition of albedo in Equation (2.9)

$$I_t(\lambda, T) = (1 - \omega(\lambda)) B(\lambda, T) . \quad (2.11)$$

With Equations (2.10) and (2.11) it is now possible to estimate the thermal emission of a volume of ice, air or snow. A comparison with the absorption of a block of ice for a characteristic irradiation calculated from Equations (2.6) and (2.7) can then be used as an order of magnitude approximation for the importance of those two effects at visible and NIR wavelengths. Intuitively, one would expect only weak absorption for an ice block due to its optical transparency and a very weak emission at the low snow temperature compared to an incandescent lamp or the sun.

Assuming the maximum possible emission of a black body  $\kappa_t = \kappa = \beta$  Equation (2.11) reduces to the Planck function (Equation (2.10)). Furthermore, an emitting cube with a surface area of 1 m<sup>2</sup> is assumed as a simple geometry. Integrating the Planck function over the entire solid angle  $4\pi$  then yields an emitted power on the order of  $10^{-50}$  to  $10^{-8}$  W for temperatures between  $-10$  and  $0^\circ\text{C}$  and wavelengths between 350 and 1000 nm.

Those values are compared to absorption calculations for an incident radiation of a halogen lamp and the solar irradiation at the Earth's surface. Both exhibit a power spectrum on the order of about 1 W m<sup>-2</sup> per nm wavelength from 350 to 1000 nm. For those wavelengths and the complex refractive indices of ice compiled by *Warren and Brandt* (2008) the ice absorption coefficients are computed with Equation (2.7). The absorbed part of the radiation inside the ice block can then be calculated by the exponential intensity decrease according to the Lambert-Beer law (Equation (2.6)) for the cube edge length  $s \approx 0.4$  m. The resulting absorbed power ranges from  $10^{-4}$  W at 350 nm to an absorbed power  $> 0.99$  W at 1000 nm for the incident power of 1 W.

This simple estimation shows clearly that absorption in ice is more significant than emission by many orders of magnitude for radiative transfer at the temperatures and wavelengths discussed in this thesis. Transferring this conclusion to snow, however, demands further thoughts. Total emission in snow does not surpass the maximum possible emission of a black body as it was already assumed in estimating emitted power, here. But, in comparison to absorption in solid ice absorption in snow is lower for the same volume as only part of the snow volume is filled by ice (about 5 to 50%) and the rest is filled by transparent air. At the same time, absorption inside the ice fraction is enhanced compared to a homogeneous ice block of the same ice volume due to scattering in snow. Scattering causes light paths to be highly tortuous and to travel a longer distance than the linear dimension of the snow block before emerging. While these two effects do not

offset each other, exactly, they do not yield an estimated absorption in snow which differs by several orders of magnitude compared to pure ice.

The order of magnitude estimate of emitted and absorbed power by pure ice combined with the special considerations for snow lead to the conclusion that emission can be neglected when modeling radiative transfer in snow for visible and NIR radiation.



## 3 Modeling Radiative Transfer in Snow

To include all electromagnetic effects modeling radiative transfer should rely as heavily as possible on solving the fundamental Maxwell equations for the exact geometry of the modeled system. Due to the immense need for computing power this direct approach in the form of a numerical solution is still limited to small or simple macroscopic volumes. Thus, modeling radiative transfer in snow on the ground with its complex morphology (Figure 1.1(b)) requires a simplification to the complete electromagnetic theory and/or the snow microstructure.

In general, the solution of the radiative transfer problem in scattering media involves two steps:

- Obtaining the microscopic single-scattering properties of the medium: For a random particle collection of known particle size and shape the single-scattering radiative properties are determined by solving the Maxwell equations for one single particle. For scattering media with a more complex microstructure, the microscopic radiative properties are calculated for a small sub-volume where the radiation field is still characterized by only one interaction event and multiple-scattering can be neglected.
- Calculating the macroscopic radiative properties of the medium: Using the microscopic single-scattering properties as input the RTE is solved for the entire medium considering the correct boundary conditions.

In this chapter, three different models for radiative transfer in snow are presented which share this two-step approach but still differ strongly in the exact methodology. First, the DISORT model is introduced in Section 3.2. Here, the snow microstructure is approximated by a collection of ice spheres. Reasoning behind this approximation is discussed in Section 3.1. For DISORT, the full RTE is then solved for the equivalent snow microstructure. The ray-tracing model described in Section 3.3, on the other hand, calculates the microscopic radiative properties of the true 3D microstructure or an equivalent microstructure while approximating the full electromagnetic theory by geometrical optics (GO). Finally, in Section 3.4 both electromagnetics and snow microstructure are simplified. As for DISORT the snow microstructure is replaced by an equivalent collection of ice spheres. Additionally, the radiation field is assumed to be unperturbed by boundary effects, i.e. by sharp transitions within the snow or from snow to the surrounding medium. Results of radiative transfer calculations for these three models are compared in Section 3.5.

### 3.1 Approximating snow microstructure by equivalent ice spheres

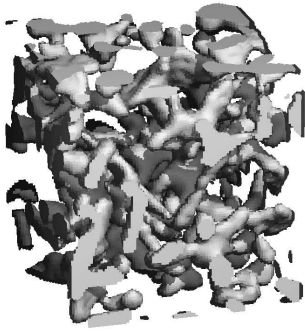
The fundamental assumption for the use of DISORT (*Stamnes et al.*, 1988, see also Section 3.2 for a description) in radiative transfer calculations is that it is possible to approximate the microstructure of the scattering medium by a collection of randomly distributed spheres with according OED and mass density. It has already been mentioned briefly in Section 1.2.2 that this model has proven successful in describing snow albedo.

Including but not limited to snow, calculations have shown that particle shape can have a significant effect on the resulting optical properties of a single particle and a collection of identical particles (*Macke et al.*, 1995; *Macke and Mishchenko*, 1996; *Kokhanovsky and Nakajima*, 1998; *Nakajima et al.*, 1998; *Kokhanovsky and Zege*, 2004; *Bänninger et al.*, 2006; *Kolokolova et al.*, 2006; *Xie et al.*, 2006; *Picard et al.*, 2009). The studies specifically investigating ice clouds and snow found the most significant discrepancies in the single-scattering properties and in the angular distribution of the reflected, absorbed and transmitted radiation for particle collections. Hemispherically averaged optical properties like albedo exhibit less striking discrepancies between particle collections of different particle shapes (*Grenfell and Warren*, 1999; *Neshyba et al.*, 2003; *Grenfell et al.*, 2005).

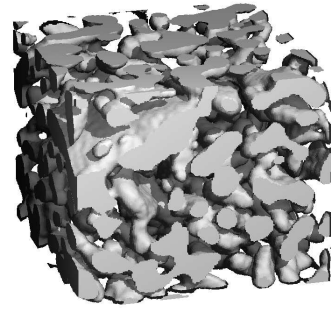
In addition to radiative transfer simulations in snow, experimental works have been performed to correlate macroscopic optical properties to snow microstructural parameters. However, all studies have either not investigated the effect of introducing an equivalent microstructure of spherical snow grains (*Nolin and Dozier*, 2000; *Meirolid-Mautner and Lehning*, 2004; *Matzl and Schneebeli*, 2006; *Painter et al.*, 2007) or found that this effect could not explain the discrepancy between measurements and model calculations (*Domine et al.*, 2006; *Gallet et al.*, 2009). Snow reflectance simulations and measurements by *Painter and Dozier* (2004) show better agreement for snow types composed of rounded structures than for fine-grained snow types but the effect was not investigated in more detail.

Looking at the true 3D microstructure of snow on the ground (e.g. in Figures 1.1(b) or 3.1 in contrast to atmospheric snow in Figure 1.1(a)) it is clear that all snow types consist of a wide variety of characteristic ice-structure shape and size. While faceted crystals with planar surfaces and sharp edges can be observed in depth hoar and coarse-grained melt-freeze snow rounded shapes predominate even for these snow types. Thus, if snow microstructure is simplified by a single equivalent grain shape a sphere is an obvious choice. This also makes sense from a computational point of view as for a sphere all radiative properties can be calculated exactly by Mie theory (*Mie*, 1908), an analytical solution to the Maxwell equations for spheres. For other particle shapes an exact solution to the scattering problem of arbitrary particle size and irradiation wavelength has not been found or is computationally intensive (*Wielgaard et al.*, 1997).

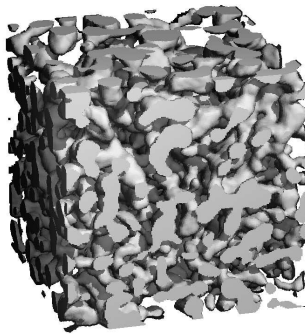
To add more scientific relevance to this discussion snow OED can be compared to a grain size deduced from the mean curvatures of the true snow microstructure. To this end six snow samples are scanned by micro-CT. The respective morphology is shown in Figure 3.1. After a  $3^3$ -voxel smoothing operation the normal vectors of all ice surface voxels are calculated. Then, the curvatures are computed for each voxel. Assuming



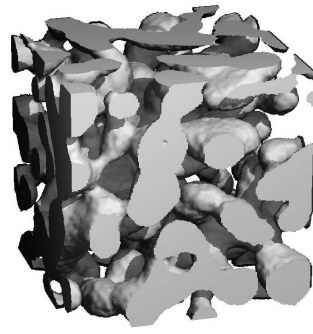
(a) Decomposing and fragmented (DF)



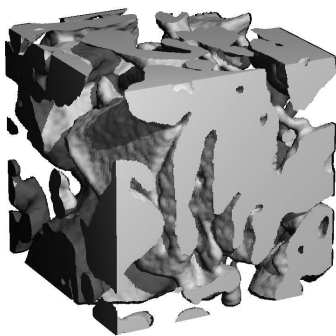
(b) Machine made (MM)



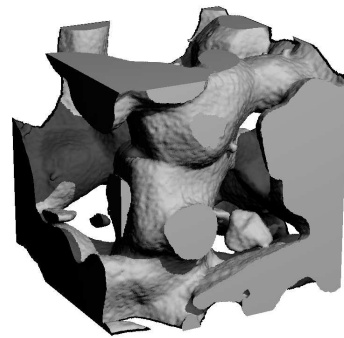
(c) Rounded and faceted (RG+FC)



(d) Rounded (RG)



(e) Depth hoar (DH)



(f) Melt forms (MF)

**Figure 3.1:** Snow microstructure for 6 snow samples scanned by micro-CT. Snow type is indicated for each sample according to *Fierz et al.* (2009). Edge length of the pictured snow cubes is 1.5 mm (DF), 2 mm (MM) and 3 mm (RG+FC, RG, DH, MF). The voxel size of the micro-CT scans is  $10^3$  to  $15^3 \mu\text{m}^3$ .

equivalent spheres of radius  $r_{\text{ice}}$  with mean curvature  $H$  leads to the relation

$$H = \frac{1}{r_{\text{ice}}} . \quad (3.1)$$

The respective curvature-equivalent grain size ( $\text{CED} = 2 \cdot \overline{r_{\text{ice}}}$ ) can be derived from the curvature histograms shown in Figure 3.2 and then compared to the OED computed from the micro-CT data by Equation (1.1). In a strict sense, a valid comparison of CED to OED demands that  $H$  be averaged according to the correct relation between OED and snow optical properties. However, this is not possible for a single general case as the dependence on grain size varies according to irradiation wavelength and analyzed optical property. At visible and NIR wavelengths, reflectance can be approximated by  $\text{OED}^{-\frac{1}{p}}$  with  $p$  depending on the analyzed wavelength. *Domine et al.* (2006), for example, found a good linear correlation between snow reflectance and  $\text{OED}^{-1}$  for 3 wavelengths between 1.6 and 2.3  $\mu\text{m}$  where ice is highly-absorbing. In Table 3.1 CED is calculated from the arithmetic mean of  $H$  and compared to OED.

**Table 3.1:** Comparison of OED and CED for the same snow samples as in Figures 3.1 and 3.2. To reduce the influence of the sample volume for DH and MF due to the very large ice structures compared to the total sample volume, OED and CED are the respective arithmetic mean for two samples of the same size.

Snow type sample	OED [mm]	CED [mm]	$\frac{\text{CED}-\text{OED}}{\text{OED}}$
DF	0.17	0.20	0.18
MM	0.25	0.32	0.28
RG+FC	0.29	0.36	0.24
RG	0.43	0.54	0.26
DH	0.73	1.82	1.49
MF	1.60	2.10	0.31

Table 3.1 shows that for all samples CED is higher than OED. The relative difference is clearly the largest for DH snow with 149%. This is not surprising as DH snow is generally characterized as snow consisting of coarse faceted ice structures with plane faces (see Figure 3.1(e)). Here, the simplification as equivalent spheres (used for OED) is the furthest removed from the true microstructure (used to derive CED). Nevertheless, the relative difference between CED and OED for all other samples ranges from 18 to 31% which is a good agreement considering the simple derivation of both equivalent grain sizes CED and OED from the 2 different microstructural parameters  $H$  and SSA, respectively.

For a more complete picture however, the entire curvature histograms should be analyzed instead of only one basic mean value. Figure 3.2 shows a smooth mean curvature distribution with only one possible peak at  $H = 0$  for all snow samples. Calculated Gaussian curvatures are 0 for all voxels where  $H = 0$ . This implies that for the samples all voxels with zero mean curvature are part of a facet, i.e. a plane face, and not saddle points of the ice matrix. Hence, for snow exclusively composed of faceted crystals, e.g. cubes only, one would expect  $H = 0$  for all voxels except edge voxels where the mean curvature would then assume very high values depending on the resolution of the scans and the size

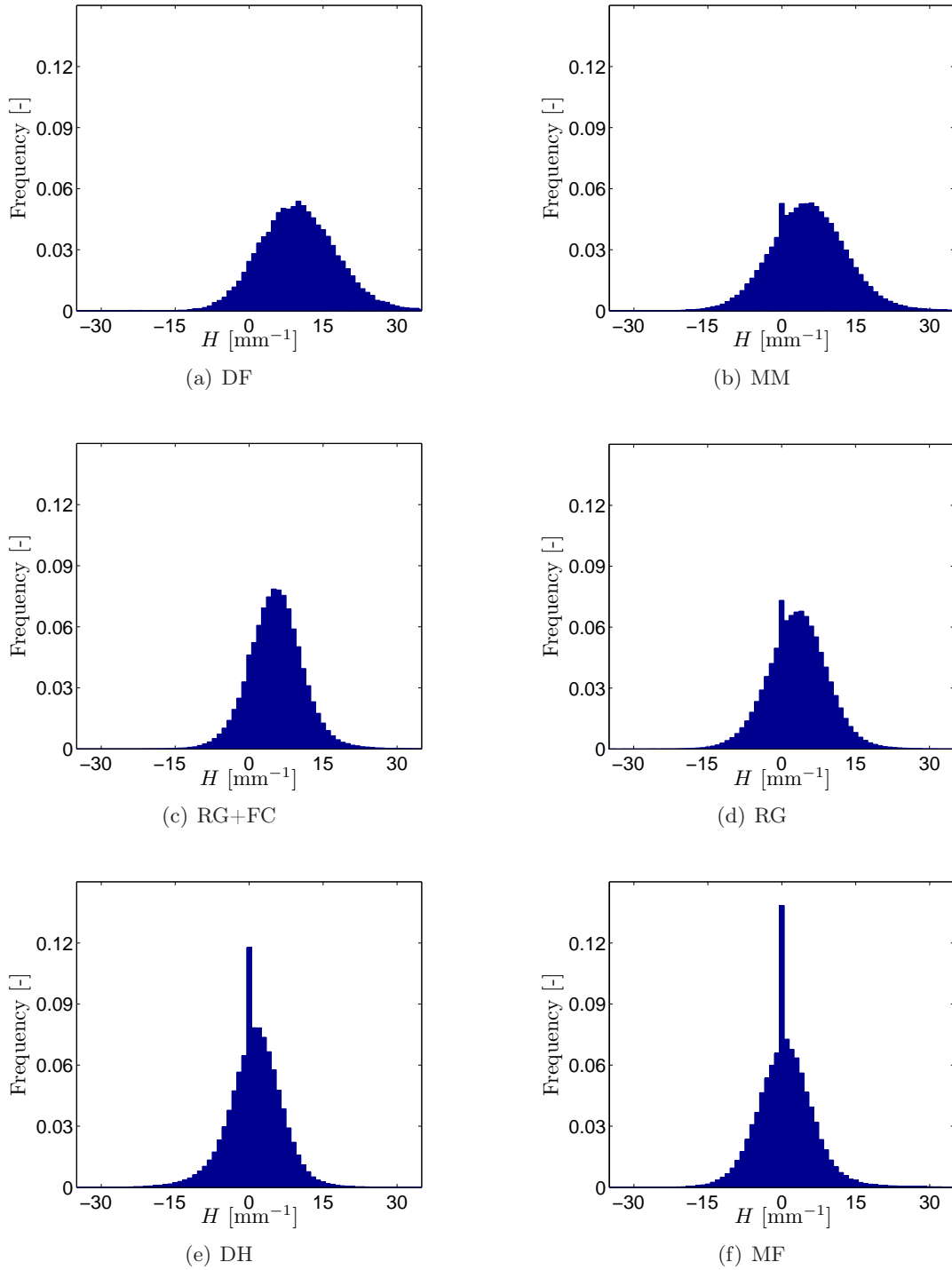


**Figure 3.2:** Mean curvature histograms for the 6 snow samples as shown in Figure 3.1. The histograms plot the relative frequency of the mean curvature  $H$  at a resolution of 1 bin per  $\text{mm}^{-1}$ . A peak at  $H = 0$  indicates a snow type which is characterized by facets, i.e. plane ice faces.

of the smoothing window to calculate the mean curvatures. As expected DH snow shows a sharp peak at  $H = 0$ . For fine-grained snow this peak is not visible anymore except for the peculiar MM snow with its many plate-like features (see Figure 3.2(b) and a more detailed description in Chapter 5). However, except for the possible spike at  $H = 0$  all snow samples show a smooth mean curvature distribution which indicates that no snow sample has a pure or even predominantly faceted character.

The most unexpected finding from the curvature histograms is that there exist many facets for RG and especially MF snow. This finding is evident from the mean curvature histograms plotted in Figure 3.2. Traditionally, these snow types have been assumed to exhibit the closest resemblance to a simplified microstructure of ice spheres and thus to be approximated by OED spheres better than other snow types for radiative transfer problems. Here it is shown that this mainly heuristic assumption is not supported by actual snow-microstructural data.

So, the influence of approximating the true 3D snow microstructure by equivalent ice spheres on radiative transfer in snow ultimately has to be investigated by comparing radiative transfer calculations by different models among each other and with experiments.

## 3.2 Discrete-ordinate-method radiative transfer (DISORT)

### 3.2.1 Single-scattering properties

As input for the multiple-scattering radiative transfer solution (detailed in Section 3.2.2) the three single-scattering properties extinction coefficient  $\beta$ , albedo  $\omega$  and asymmetry parameter  $g$  have to be computed. They fully describe one interaction event between radiation and scattering medium within radiative transfer theory. The computations are done by Mie theory (*Mie*, 1908). This yields an exact solution to the scattering problem of one single sphere of arbitrary size with refractive index  $n + ik$  surrounded by transparent air for incident radiation at wavelength  $\lambda$ . Due to the dependance on the refractive index all three single-scattering properties depend on sphere size and radiation wavelength (see Figure 2.3 for the refractive index of ice). A detailed summary of Mie theory is given in *van de Hulst* (1957). A short outline is presented in the following paragraphs.

Mie theory starts with the Maxwell equations and the derivation of the electromagnetic wave equation

$$\left(\Delta - \frac{1}{c^2} \frac{\partial^2}{\partial t^2}\right) \mathbf{A} = 0 . \quad (3.2)$$

Here, the vector field  $\mathbf{A}$  can be the electric or the magnetic field. For a spherical symmetry, the scalar components of the solution to Equation (3.2) can be written as a combination of infinite series of Legendre polynomials and spherical Bessel functions. This is true for the incident wave, the wave inside the scattering sphere and the outgoing scattered wave. All three desired single-scattering properties  $\beta$ ,  $\omega$  and  $g$  at a large distance from the scattering sphere can then be computed from the coefficients of the infinite series describing the outgoing scattered wave.

A crucial step of this approach is the truncation of the infinite series, which form the basis of the solution. The number of terms to be included depends on the size parameter  $x$ ,

i.e. the ratio of sphere circumference to radiation wavelength:

$$x = \frac{2\pi r_{\text{ice}}}{\lambda} . \quad (3.3)$$

With increasing size parameter more terms have to be included in the solution and the calculations require an increasing computation power. Typical size parameters for snow at visible or NIR wavelengths range from  $x = 60$  to  $x \geq 10^4$ .

In addition to  $r_{\text{ice}}$  and  $\lambda$ , the extinction coefficient also depends on snow density  $\rho_{\text{snow}}$ :

$$\beta = f(r_{\text{ice}}, \lambda) \frac{\rho_{\text{snow}}}{\rho_{\text{ice}} r_{\text{ice}}} . \quad (3.4)$$

For natural snow and visible or NIR lighting  $f(r_{\text{ice}}, \lambda) \approx \text{constant}$ , which describes the geometrical limit for grain radii  $r_{\text{ice}} \gg \lambda$  or  $x \gg 2\pi$ .  $\rho_{\text{ice}} = 917 \text{ kg m}^{-3}$  is the density of ice at  $0^\circ\text{C}$ . A rigorous solution for a spherical scattering particle leads to the exact expressions for  $f(r_{\text{ice}}, \lambda)$  in Equation (3.4),  $\omega$  and  $g$ . These are involved infinite series and integrals which do not add significantly to a deeper understanding. So, they will not be given in a general form here. Results of the single-scattering properties for real snow samples are presented in Section 3.5.

### 3.2.2 Multiple-scattering radiative transfer solution

With the single-scattering properties calculated by Mie theory the RTE (2.1) can now be solved to obtain the macroscopic multiple-scattering optical properties. The DISORT model only covers radiative transfer for plane-parallel layered atmospheres, i.e. 1D atmospheres. In the following it will be assumed that layering is in the  $z$ -direction with polar angle  $\theta$  and azimuth  $\varphi$ . While thermal emission can be included in DISORT, in this study thermal radiation is neglected for all DISORT simulations due to its estimated insignificance at the considered snow temperatures (see Chapter 2.3). Additionally, the normal optical depth  $\tau$  is introduced:

$$\tau(\lambda) = \int_0^z \beta(\lambda, z') dz' . \quad (3.5)$$

Geometry and input parameters of the considered radiative transfer problem are illustrated in Figure 3.3. Each snow layer is characterized by normal optical depth  $\tau$ , albedo  $\omega$  and phase function  $\Phi$  with asymmetry parameter  $g$ . For monochromatic radiation and with  $\mu = \cos(\theta)$  the RTE (2.1) can be rewritten for every layer in the form (*Chandrasekhar, 1950; Stamnes et al., 1988*)

$$\mu \frac{dI(\tau, \mu, \varphi)}{d\tau} = I(\tau, \mu, \varphi) - \omega(\tau) \int_0^{2\pi} d\varphi' \int_{-1}^1 d\mu' \Phi(\tau, \mu, \varphi, \mu', \varphi') I(\tau, \mu', \varphi') . \quad (3.6)$$

This is an integro-differential equation and cannot be solved analytically. Instead, Equation (3.6) is solved numerically by the discrete ordinate approximation: The surface integral which describes scattering enhancement is approximated by a quadrature sum converting Equation (3.6) into a system of coupled ordinary differential equations. A

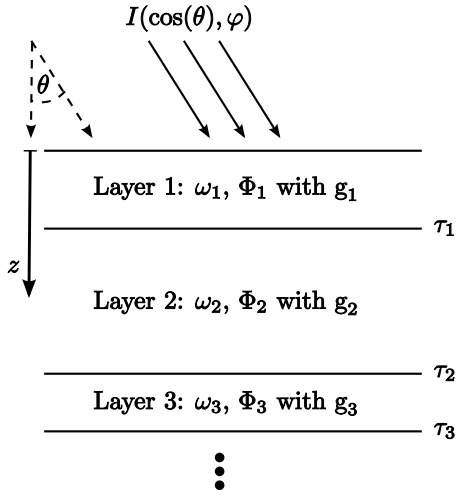


**Figure 3.3:** DISORT model geometry and input parameters as they are used in this study. A suitable bottom boundary condition has to be chosen according to the considered problem.

higher number of quadrature points (for DISORT these are the polar directions  $\mu$ ) gives a higher precision of the solution. User-defined incident illumination (direct beam or diffuse) and computation and output data depths (for flux and intensity calculations) make this model useful for a vast number of radiative transfer applications (e.g. *Nolin and Dozier, 2000; Zhou et al., 2003a; Painter and Dozier, 2004; Domine et al., 2006; Gallet et al., 2009*).

Here, only reflectance and transmittance calculations of macroscopic snow samples are performed for either diffuse or collimated irradiation parallel to the  $z$ -axis. For highly-scattering media like snow or tissue the Henyey-Greenstein phase function  $\Phi_{\text{HG}}$  (introduced in Chapter 2.1) has been used widely. *Aoki et al. (2000)* calculated and measured angularly resolved bidirectional reflectance of a flat snowfield in Japan. They used both  $\Phi_{\text{HG}}$  and the Mie phase function for multiple scattering of a collection of OED ice spheres and found a better agreement between reflectance measurements and calculations when using  $\Phi_{\text{HG}}$ .

Hence, all DISORT calculations in this thesis are done using the Henyey-Greenstein phase function. Using other phase functions only has a minor effect on overall reflectance and transmittance calculations and does not change the fundamental conclusions. Only angularly resolved intensities vary significantly among calculations at a resolution of few degrees for different phase functions (*Aoki et al., 2000*).

### 3.3 Ray tracing

In contrast to DISORT, ray tracing does not yield an exact solution to the considered radiative transfer problem with the chosen input parameters. Instead, by tracing light rays the wave nature of light is neglected and radiative transfer is implicitly approximated by geometrical optics (GO). This can be justified by the high size parameters of snow at visible and NIR lighting (see Section 3.2.1). For those size parameters the complete electromagnetic description does not lead to significantly different results than the GO

approximation when calculating single-scattering properties of highly-scattering particles of various shapes (Ungut *et al.*, 1981; Macke *et al.*, 1995; Wielaard *et al.*, 1997; Zhou *et al.*, 2003b). Additionally, only overall reflectance and transmittance are compared in the presented thesis instead of angularly resolved intensities, which are highly dependent on viewing direction. Finally, the various shapes present in the microstructure of any snow type as seen in Figures 3.1 and 3.2 and the high number of scattering events in a macroscopic snow sample of several  $\text{mm}^3$  lead to a blurring of wave effects, which are not captured by GO.

Two different ray-tracing models are used in this study:

- A Monte Carlo model based on micro-CT (CTMC) which offers the possibility to use the true 3D microstructure from CT scans as input for the radiative transfer calculations.
- Another Monte Carlo model based on 3D CAD called FRED which allows a greater flexibility in setting the geometrical boundary conditions of the problem.

### 3.3.1 Monte Carlo radiative transfer based on micro-CT (CTMC)

*Petrasch et al.* (2007) and *Haussener et al.* (2009) developed a CTMC model to analyze thermal radiative properties of porous ceramics and packed beds of  $\text{CaCO}_3$  and to ultimately improve the understanding of solar-driven thermochemical processes in packed-bed reactors. This methodology is adapted to calculate radiative properties in snow at visible and NIR wavelengths on the pore scale and then for the continuum domain, i.e. macroscopic snow samples. Pore-scale and continuum domains correspond to single-scattering and multiple-scattering radiative transfer regimes for the DISORT model explained in Section 3.2.

The CTMC model explicitly considers radiative transfer in each constituent and at each interface of the scattering medium according to the respective imaginary refractive indices. This means that in a two-phase medium like snow the RTE (2.1) has to be valid in each of the two bulk materials. For snow these are the two phases ice and air. Volume averaging leads to two coupled RTEs (*Lipiński et al.*, 2010a,b) for the volume-averaged intensity  $I_i$ :

$$\begin{aligned} \hat{\mathbf{n}} \cdot \nabla I_i(\mathbf{r}, \hat{\mathbf{n}}, \lambda) = & -\beta_i(\lambda)I_i(\mathbf{r}, \hat{\mathbf{n}}, \lambda) + \kappa_{t,i}(\lambda)B(\lambda, T(\mathbf{r})) \\ & + \int_{\Omega} d\hat{\mathbf{n}}' \sigma_{s,ii}(\lambda)\Phi_{ii}(\hat{\mathbf{n}}, \hat{\mathbf{n}}', \lambda)I_i(\mathbf{r}, \hat{\mathbf{n}}', \lambda) \\ & + \int_{\Omega} d\hat{\mathbf{n}}' \sigma_{s,ji}(\lambda)\Phi_{ji}(\hat{\mathbf{n}}, \hat{\mathbf{n}}', \lambda)I_j(\mathbf{r}, \hat{\mathbf{n}}', \lambda), \end{aligned} \quad (3.7)$$

where  $i, j = 1, 2 \wedge i \neq j$ . The nomenclature is analogous to Chapter 2 except for the additional indices to explicitly describe the two phases air ( $i, j = 1$ ) and ice ( $i, j = 2$ ). In contrast to DISORT calculations in this study all CTMC calculations contain thermal emission. As already shown in Chapter 2.3, however, the inclusion of thermal radiation has a negligible effect on overall radiative transfer in snow.

### Pore-scale domain radiative properties

The pore-scale radiative properties in Equation (3.7), namely extinction, emission and scattering coefficients  $\beta_i$ ,  $\kappa_{t,i}$  and  $(\sigma_{s,ii}, \sigma_{s,ji})$  as well as scattering phase functions  $\Phi_{ii}$  and  $\Phi_{ji}$  have to be obtained before calculating the macroscopic properties reflectance and transmittance.

Absorption in ice is specified by the absorption coefficient  $\kappa_2$  according to Chapter 2.2. Internal scattering is assumed to be zero. For air internal scattering is neglected as well. Additionally, the refractive index is characterized by  $n_1 = 1$  and  $k_1 = 0$  and thus  $\kappa_1 = 0$ . This only leaves internal reflections at the phase interfaces characterized by  $\sigma_{s,ii} = \sigma_{s,\text{refl},i}$  and  $\Phi_{ii} = \Phi_{\text{refl},i}$  and interfacial refractions from phase  $j$  to phase  $i$  with  $i \neq j$  characterized by  $\sigma_{s,ji}$  and  $\Phi_{ji}$  as scattering properties to be computed. Directional reflection and refraction at the air-to-ice interfaces are calculated by the Fresnel equations (e.g in *Born and Wolf*, 1999). With Equation (2.8) extinction can be written as

$$\beta_i = \kappa_i + \sigma_{s,\text{refl},i} + \sigma_{s,ij} . \quad (3.8)$$

All these pore-scale radiative properties are obtained by the collision-based Monte Carlo ray-tracing method (*Farmer and Howell*, 1998). Here, a large number of uniformly distributed stochastic rays are emitted isotropically within an REV of the scattering medium, here a snow sample. The rays undergo refraction and reflection at the phase interfaces and are attenuated inside the ice matrix according to Equation (2.6). The distance between emission and collision points and the ray incident direction are recorded for each ray to compute probability density functions for extinction, scattering and incident angle which are uniquely related to the pore-scale radiative properties (*Haussener et al.*, 2009).

While this methodology was developed to be used with the true 3D microstructure of the scattering medium as input it is also possible to apply it to an equivalent microstructure, e.g. an equivalent snow microstructure consisting of OED spheres with the correct density. Both possibilities will be explored in Section 3.5.3.

### Continuum domain radiative properties

With all known pore-scale radiative properties reflectance and transmittance can now be calculated by solving Equation (3.7) for a macroscopic volume. For the CTMC approach this is once again achieved by the Monte Carlo method, but now rays are scattered and absorbed according to pore-scale radiative properties and ray path length in ice and air instead of differing refractive indices and their distribution (*Petrasch et al.*, 2010). This means that the entire scattering medium is now considered as a homogeneous bulk material characterized by the scattering, absorptive and emissive properties of the REV which was used to calculate these characteristics on the pore-scale.

The geometry of the CTMC continuum-domain model approach is the same as the DISORT geometry with only one layer: a 1D snow slab of thickness  $s_{\text{slab}}$  in the  $z$ -direction and infinite lateral extension. There are now 2 contributions to all calculated radiative properties of the medium: one contribution from each phase  $i = 1, 2$ .

With a homogeneous incident radiation flux  $q_{\text{in}}$  from the top and downward and upward directions labeled by ‘+’ and ‘-’ signs reflectance  $R$  and transmittance  $Tr$  of a snow slab

can be written as

$$R = \frac{\overline{q_1^-}(z=0) + \overline{q_2^-}(z=0)}{q_{\text{in}}}, \quad (3.9)$$

$$Tr = \frac{\overline{q_1^+}(z=s_{\text{slab}}) + \overline{q_2^+}(z=s_{\text{slab}})}{q_{\text{in}}}. \quad (3.10)$$

The overbars in Equations (3.9) and (3.10) denote averaging over the cross-sectional area.

To compare CTMC results to DISORT simulations the same two irradiation conditions are considered: (i) diffuse and (ii) collimated incident flux  $q_{\text{in}}$  in the  $z$ -direction.

### 3.3.2 FRED: an optical engineering software based on 3D CAD

FRED is a commercial software (available at <http://www.photonengr.com/software>) to simulate radiative transfer by ray tracing in a computational domain designed by CAD. Radiation sources, scattering media or detector geometries can be specified by a built-in 3D CAD graphical user interface or imported from another CAD software. Optical properties like refractive indices, scattering coefficients or coatings with a specific optical characteristic (e.g. reflective or absorbing coatings) can be assigned to all components of the designed radiative transfer problem. Thermal emission of all components is ignored, which is only an insignificant restriction for radiative transfer simulations in snow (see Chapter 2.3). Figure 3.4 illustrates one basic radiative transfer problem whose geometry is easily drawn and implemented in FRED but cannot be implemented in the previously introduced models DISORT (see Section 3.2) or CTMC (see Section 3.3.1). This is due to the orientation of the two snow slabs: They are not layered in the  $z$ -direction and extend infinitely in the lateral directions but the layer boundary runs along the  $z$ -direction so that lateral boundary effects contribute significantly to radiative transfer in the vicinity of the layer boundary. Additionally, only a part of the surface at  $z=0$  is irradiated as indicated by the red ellipse instead of the entire surface.

Radiative transfer calculations on the basis of the true 3D snow microstructure imported from CT-scans are not feasible with FRED due to the high demand for computing power. However, ray-tracing simulations of bulk materials which are described by one scattering coefficient, phase function with asymmetry parameter and absorption coefficient each can be performed within a reasonable time frame. Thus, FRED is only used based on the latter approach and only whenever DISORT and CTMC model cannot be applied due to the problem geometry (in Chapter 4).

The methodology requires that the true 3D snow microstructure be approximated in order to obtain effective radiative properties. Here, this is achieved by making the same assumptions as for the DISORT approach: Snow is considered as a random collection of OED spheres with the correct density. So, the single-scattering radiative transfer properties are determined by Mie theory for this equivalent snow microstructure as was already explained for the DISORT model in Section 3.2.1.

To calculate intensities and eventually reflectance and transmittance the RTE (2.1) without thermal emission term is solved by Monte Carlo ray tracing for the user-defined boundary conditions: radiation source angular intensity distribution, scattering medium

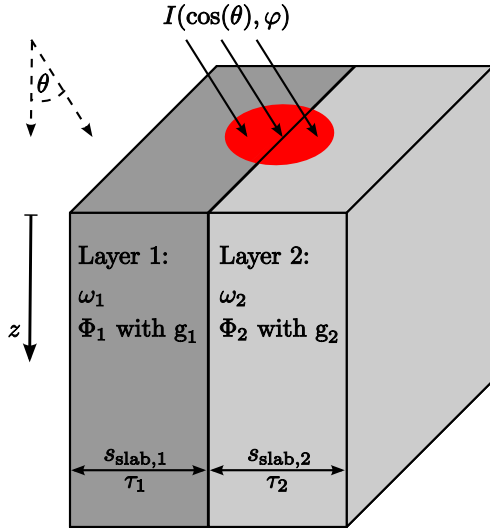


**Figure 3.4:** A radiative transfer problem geometry that can only be implemented in the FRED model: In contrast to Figure 3.3 snow slabs of thickness  $s_{\text{slab}}$  are layered along the  $z$ -direction and irradiated by a spot light.

composition and detector surface size and orientation. Scattering and absorption inside the scattering medium are computed according to the ray path length inside each bulk material and the assigned single-scattering properties. This is similar to the CTMC approach for calculating the continuum domain radiative properties. However, in contrast to the CTMC model considering only one effective scattering medium instead of a two-phase medium and neglecting thermal emission are elements found only in the DISORT multiple-scattering solution (see Sections 3.3.1 and 3.2.2).

### 3.4 Asymptotic flux extinction (AFE)

The AFE solution to the radiative transfer problem is not an entirely different model but can be seen as a further simplification of the DISORT model for one snow layer (Warren, 1982). Here, the description follows the general outline of Bohren (1987).

All boundary effects which arise due to the finite extension of the snow cover are ignored. Additionally, as the name already suggests only (hemispherical) fluxes are considered instead of (angularly resolved) intensities. Integrating all intensities in downward ( $\downarrow$ ) and upward ( $\uparrow$ ) flux  $q_{\downarrow, \uparrow}$  for the DISORT geometry leads to a two-stream model. The resulting geometry of the considered radiative transfer problem is illustrated in Figure 3.5.

For this two-stream model the phase function  $\Phi$  consists of four components  $\Phi_{ij}$  with  $ij = (\downarrow\downarrow, \downarrow\uparrow, \uparrow\downarrow, \uparrow\uparrow)$  which describe the probability of scattering radiation from direction  $i$  into direction  $j$ . Further assuming an isotropic medium the following relations hold:  $\Phi_{\downarrow\downarrow} = \Phi_{\uparrow\uparrow}$  and  $\Phi_{\downarrow\uparrow} = \Phi_{\uparrow\downarrow}$ . This should not be confused with the much more restricting cases of isotropic scattering or isotropic radiation.

The asymmetry parameter  $g$  can be written as  $g = \Phi_{\downarrow\downarrow} + \Phi_{\downarrow\uparrow}$  and also  $g = \Phi_{\uparrow\uparrow} + \Phi_{\uparrow\downarrow}$  according to its definition in Equation (2.5).

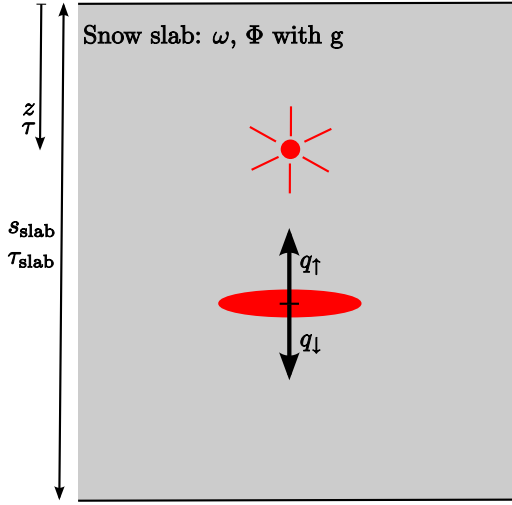


**Figure 3.5:** AFE solution geometry and input parameters. Radiation source (indicated by a red sun) and analysis area (indicated by red ellipse) are located deep inside one thick snow slab.

Then, the energy balance equations for  $q_{\downarrow}$  and  $q_{\uparrow}$  are

$$\frac{dq_{\downarrow}}{d\tau} = -q_{\downarrow} + \omega \frac{1+g}{2} q_{\downarrow} + \omega \frac{1-g}{2} q_{\uparrow} \quad (3.11)$$

and

$$\frac{dq_{\uparrow}}{d\tau} = q_{\uparrow} - \omega \frac{1+g}{2} q_{\uparrow} - \omega \frac{1-g}{2} q_{\downarrow} . \quad (3.12)$$

These equations are analogous to Equation (3.6) for only two hemispherically integrated fluxes in directions  $\downarrow$  and  $\uparrow$ .

Adding and subtracting Equations (3.11) and (3.12) leads to

$$\frac{d}{d\tau}(q_{\downarrow} - q_{\uparrow}) = -(1-\omega)(q_{\downarrow} + q_{\uparrow}) \quad (3.13)$$

and

$$\frac{d}{d\tau}(q_{\downarrow} + q_{\uparrow}) = -(1-\omega g)(q_{\downarrow} - q_{\uparrow}) . \quad (3.14)$$

Differentiating Equations (3.13) and (3.14) once again with respect to  $\tau$  and substituting the first derivatives in the resulting equations by Equations (3.14) and (3.13) yields

$$\frac{d^2}{d\tau^2}(q_{\downarrow} - q_{\uparrow}, q_{\downarrow} + q_{\uparrow}) = (1-\omega)(1-\omega g)(q_{\downarrow} - q_{\uparrow}, q_{\downarrow} + q_{\uparrow}) . \quad (3.15)$$

Solutions to these two equations at depth  $z$  with reference depth  $z_0$  inside the snow slab and the boundary conditions  $q_{\downarrow, \uparrow}(z = z_0) = q_{\downarrow, \uparrow}^0$  and  $\tau = \tau(z) - \tau(z_0)$  are:

$$q_{\downarrow, \uparrow}(\tau) = q_{\downarrow, \uparrow}^0 \exp(-k_{\text{ext}}\tau) . \quad (3.16)$$

For simplicity the asymptotic flux extinction coefficient  $k_{\text{ext}}$  is introduced in Equation (3.16):

$$k_{\text{ext}} = \sqrt{(1-\omega)(1-\omega g)} . \quad (3.17)$$

Then, transmittance  $Tr$  is given by

$$Tr = \frac{q_{\downarrow,\uparrow}(\tau)}{q_{\downarrow,\uparrow}^0} = \exp(-k_{\text{ext}}\tau) . \quad (3.18)$$

With Equations (3.13) and (3.14) reflectance  $R$  is calculated as

$$R = \frac{q_{\uparrow}^0}{q_{\downarrow}^0} = \frac{\sqrt{(1-\omega g)} - \sqrt{(1-\omega)}}{\sqrt{(1-\omega g)} + \sqrt{(1-\omega)}} . \quad (3.19)$$

Equation (3.16) shows that one formula easily derived from the single-scattering properties is able to describe radiative fluxes inside a snow slab both in the upward and the downward direction. However, in a strict sense the AFE solution is only valid for radiative flux calculations of large snow blocks where both radiation source and detector are located inside the snow block far away from all boundaries. How deep inside the snow block irradiation source and detector have to be positioned in order to describe radiative transfer for this geometry ultimately depends on snow type, density and radiation wavelength.

To actually use the AFE solution for radiative transfer calculations in snow  $k_{\text{ext}}$  can be obtained by Mie theory computations for an equivalent snow microstructure of OED ice spheres as described in Section 3.2.1. By this method *Warren et al.* (2006) derived ice absorption coefficients from snow transmittance measurements for ultraviolet and visible radiation. They compared calculated transmittance with spectrometer measurements inside the Antarctic snow cover using a reference depth  $z_0 = 40$  cm.

The simplicity of the AFE solution is the great attraction of this approach to radiative transfer modeling in contrast to the DISORT and ray tracing models (presented in Sections 3.2 and 3.3). However, it has to be seen if the strict assumptions in its derivation do not limit the validity of the AFE solution to few radiative transfer problems with practical use in this study. Thus, AFE theory will also be tested to analyze five real snow samples and compared to the other models in the next Section 3.5.

## 3.5 Model results for five real snow samples

The DISORT, CTMC ray-tracing and AFE methodologies introduced in Sections 3.2 to 3.4 are tested on five snow samples. The CTMC calculations were done by Sophia Haussener at the ETH Zurich. Part of the results have been submitted for publication to the *Journal of Geophysical Research* together with part of the measurement analysis in Chapter 5.

### 3.5.1 Snow sample microstructural characterization

Sample classification and preparation procedures are indicated in Table 3.2. Three samples were prepared by sieving fresh snow into boxes and stored at different temperatures to permit isothermal metamorphism at different rates. The remaining two snow samples were collected in the field.

Micro-CT is used to obtain the true 3D snow microstructure of all collected snow samples as described in Chapter 1.2.1. The CT-scanned subvolumes of the samples are

**Table 3.2:** Overview of 5 snow samples for later radiative transfer calculations. Classification according to *Fierz et al. (2009)* and Figure 3.1.

Id	Snow type	Classification	Preparation
ds	decomposing snow	DF	fresh snow stored at $-50^{\circ}\text{C}$ for 8 days
mI	metamorphosed I	RG	fresh snow stored at $-17^{\circ}\text{C}$ for 14 days
mII	metamorphosed II	RG	fresh snow stored at $-3^{\circ}\text{C}$ for 17 days
dh	depth hoar	DH	snow from the field
ws	wet snow	MF	snow from the field soaked in ice water

shown in Figure 3.6. For those sample volumes the microstructural parameters density, SSA and OED are compiled in Table 3.3. Comparing Tables 3.3 and 3.2 it can be seen that storing snow at a warmer temperature and for a longer time leads to faster settling and faster isothermal metamorphism: Density increases while SSA decreases from ds to mI and mII snow.

**Table 3.3:** Density, SSA and OED of the snow samples listed in Table 3.2 and pictured in Figure 3.6.

Id	Density [ $\text{kg m}^{-3}$ ]	SSA [ $\text{mm}^{-1}$ ]	OED [ $\mu\text{m}$ ]
ds	137.5	54.5	110
mI	146.7	40.3	149
mII	183.4	27.4	219
dh	302.6	8.4	714
ws	605.2	4.6	1304

The presented morphological data contain all microstructural input parameters needed to calculate microscopic and macroscopic radiative transfer properties for snow slabs consisting of those five snow types with the models introduced in Sections 3.2 to 3.4.

### 3.5.2 Particle- and pore-level radiative properties

For ray tracing, particle- and pore-level radiative properties are calculated for an REV of the respective true 3D snow microstructure shown in Figure 3.6. The CTMC model is used which is described in Section 3.3.1. Both DISORT and the AFE solution rely on Mie theory to calculate the particle- and pore-level radiative properties of the equivalent snow microstructure (explained in Section 3.2.1). Here, the single-scattering properties of OED spheres are obtained for the respective snow sample density and OED data in Table 3.3.

The scattering coefficients are shown in Figure 3.7 as a function of wavelength in the visible and NIR part of the spectrum: 4 scattering coefficients for the CTMC model ( $\sigma_{s,\text{refl},i}$  for scattering in each phase  $i$  and  $\sigma_{s,ij}$  for scattering at the phase interfaces) and one apparent scattering coefficient  $\sigma_{s,a}$  for Mie theory applied to OED ice spheres, which are used as input for DISORT and the AFE solution.

A common feature of the 5 calculated  $\sigma_s$  in Figure 3.7 is that snow types with higher

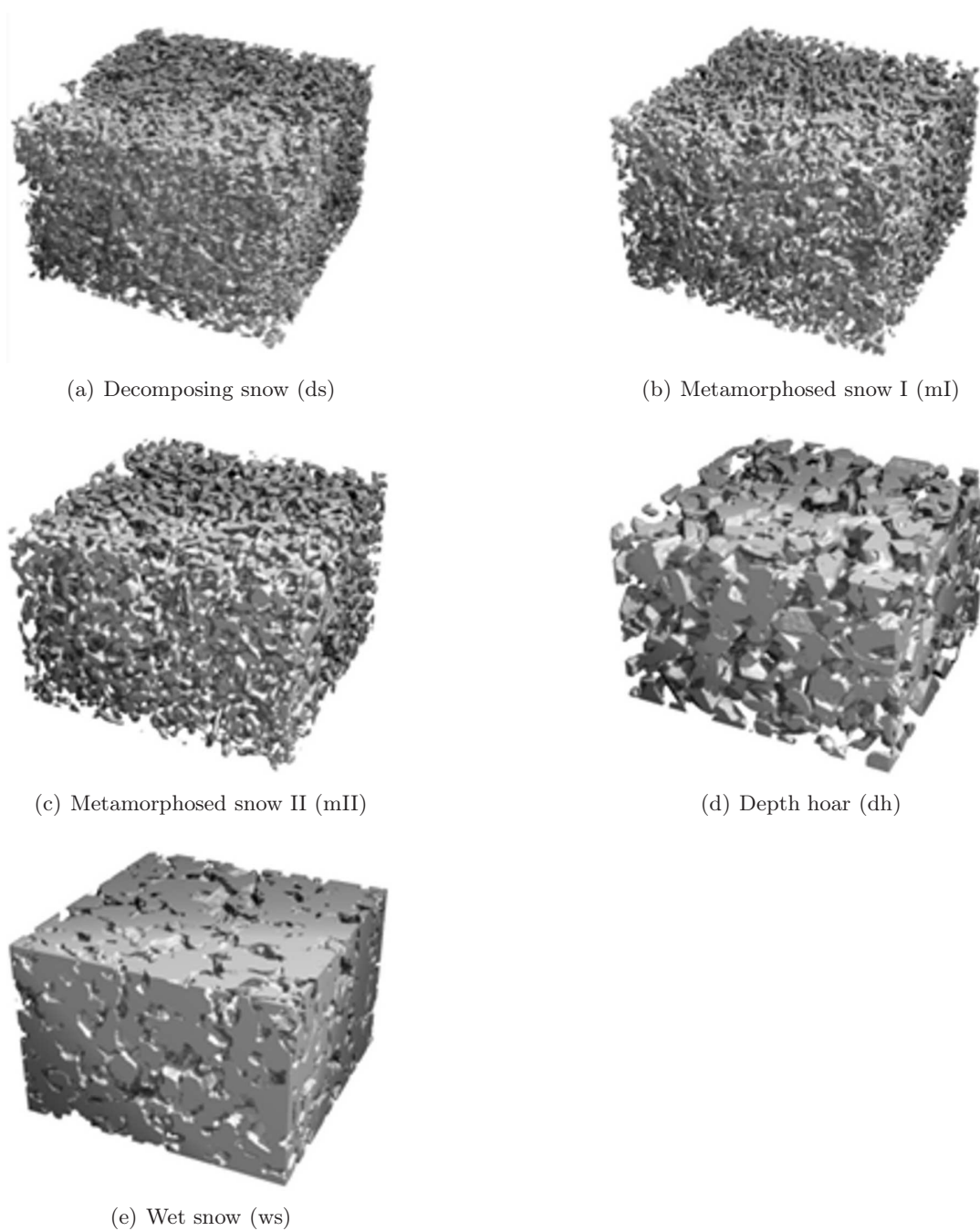


**Figure 3.6:** Snow microstructure of 5 snow samples scanned by micro-CT. Snow type and sample Id are indicated for each sample according to Table 3.2. Sample volumes are:  $6 \times 6 \times 4 \text{ mm}^3$  for (a)–(c),  $10.8 \times 10.8 \times 7.2 \text{ mm}^3$  for (d)–(e).

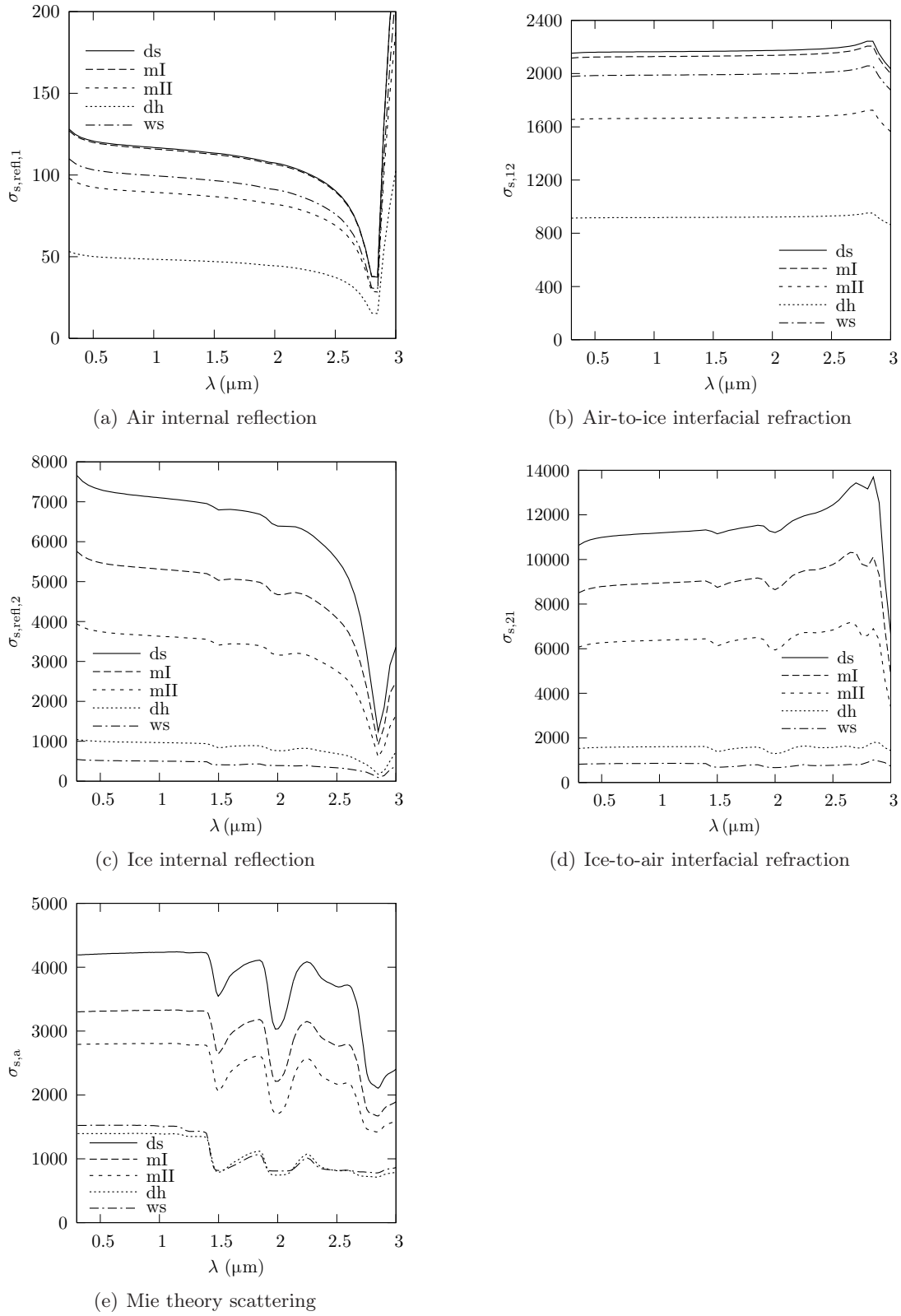


**Figure 3.7:** Scattering coefficients  $\sigma_s$  [ $\text{m}^{-1}$ ] according to CTMC model (a)–(d) and Mie theory for DISORT and AFE solution (e). Scaling of  $\sigma$  varies to resolve the 5 snow types.

SSA and thus lower OED generally exhibit higher scattering coefficients. The only snow sample which does not always fit this observation is ws snow.

As expected for the CTMC model, reflections in the air phase at the air-to-ice interface (plotted in Figure 3.7(a)) contribute the least to all possible scattering. The greatest contributions are caused by interfacial refraction and by reflections in the ice phase due to total reflection. Additionally, for both air and ice phase the trend of  $\sigma_{s,ij}$  is complementary to  $\sigma_{s,\text{refl},i}$ , since  $\sigma_{s,ij}$  describes the transmitted fraction of radiation across the interface, i.e. the radiation which is not already included in the reflected light by  $\sigma_{s,\text{refl},i}$ .

Comparing all  $\sigma_s$  for the CTMC model with  $\sigma_{s,a}$  for DISORT and the AFE solution, it is evident that  $\sigma_{s,a}$  values (in Figure 3.7(e)) lie in between the values of scattering in the air phase (in Figures 3.7(a) to 3.7(b)) and the values of scattering in the ice phase (Figures 3.7(c) to 3.7(d)) for all 5 snow samples. Additionally, the shape of  $\sigma_{s,a}$  differs clearly from  $\sigma_s$  of the ice and air phase.

Adding absorption to scattering according to Equations (2.8) and (3.8) the extinction coefficients are obtained: one each for air  $\beta_1$  and ice phase  $\beta_2$  in the CTMC model and one  $\beta_a$  for DISORT and the AFE solution. They are plotted for the 5 snow samples in Figure 3.8. Generally, the extinction coefficients increase with increasing SSA except for ws snow. This has already been seen for the scattering coefficients in Figure 3.7.

$\beta_1$  is independent of wavelength. High absorption with strong spikes at  $\lambda \gtrsim 1.5 \mu\text{m}$  in Figure 2.3 lead to a corresponding spiky trend in  $\beta_2$ . For  $\lambda > 2.7 \mu\text{m}$  absorption in ice strongly increases by several orders of magnitude and causes an equally increasing extinction in Figure 3.8(b). These observations suggest a strong domination of extinction by scattering at visible and NIR wavelengths up to  $\lambda \approx 2.5 \mu\text{m}$ .

Similar to the scattering analysis, the values for  $\beta_a$  calculated by Mie theory also lie in between the values of the extinction coefficients calculated by the CTMC ray-tracing model. In contrast to  $\sigma_{s,a}$  in Figure 3.7(e),  $\beta_a$  only shows a weak dependance on wavelength. This agrees with general results of Mie theory calculations for large size parameters, which is true for snow at the analyzed wavelengths since  $\text{OED} \gg \lambda$ .

The final particle- and pore-level radiative property to be determined for the 5 snow samples is the scattering phase function explained in Chapter 2.1. The results are shown in Figure 3.9(a) to 3.9(d) at two wavelengths  $\lambda = 0.5 \mu\text{m}$  and  $\lambda = 1.5 \mu\text{m}$  and plotted against the cosine of the scattering angle  $\mu_s$ . The phase functions  $\Phi_{ij}$  and  $\Phi_{\text{refl},i}$  are calculated by the CTMC model. For DISORT and the AFE solution  $\Phi_a$  is calculated by the Henyey-Greenstein phase function  $\Phi_a = \Phi_{\text{HG}}$  (in Equation (2.4)), which contains the asymmetry parameter  $g$  calculated by Mie theory and shown in Figure 3.9(e). All scattering phase functions for the CTMC model show the same trend independent of snow type and wavelength. For ceramics a low sensitivity on morphology has already been observed by *Haussener et al.* (2010). The sharp increase in  $\Phi_{\text{refl},2}$ , i.e. only in the ice phase, can be explained by total reflection, which leads to increased forward scattering. As expected, forward scattering dominates all phase functions both for the CTMC model and the DISORT and AFE approaches.

The closest resemblance to  $\Phi_a$  of the DISORT and AFE approaches is found for  $\Phi_{12}$ ,  $\Phi_{21}$  of the CTMC model as these phase functions describe scattering across the air-to-ice and ice-to-air interfaces. This is closely related to scattering according to Mie theory, where spherical inhomogeneities of ice are considered in air.

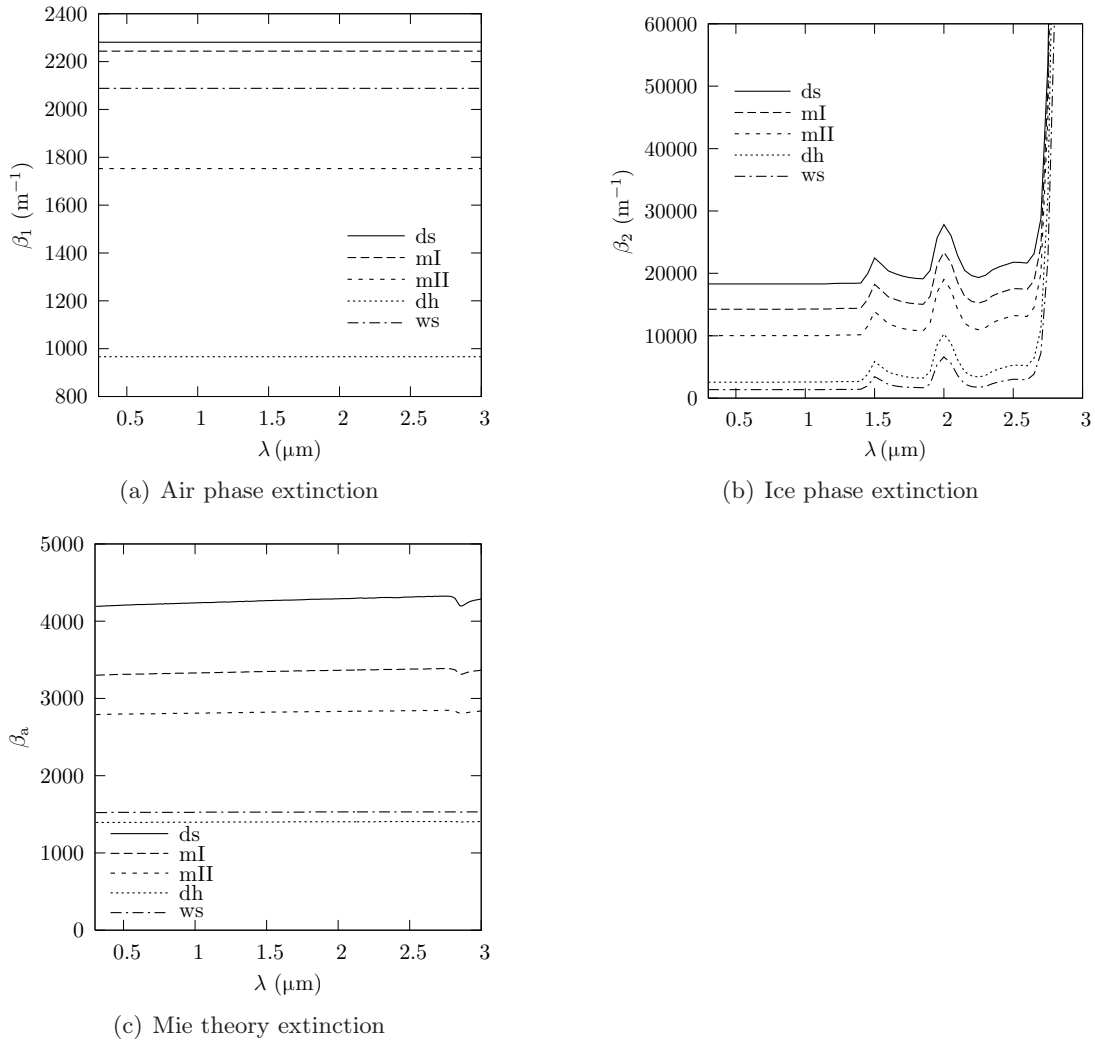


**Figure 3.8:** Extinction coefficients  $\beta$  [ $\text{m}^{-1}$ ] according to CTMC model (a)–(b) and Mie theory for DISORT and AFE solution (c). Scaling of  $\beta$  varies to resolve the 5 snow types in each plot.

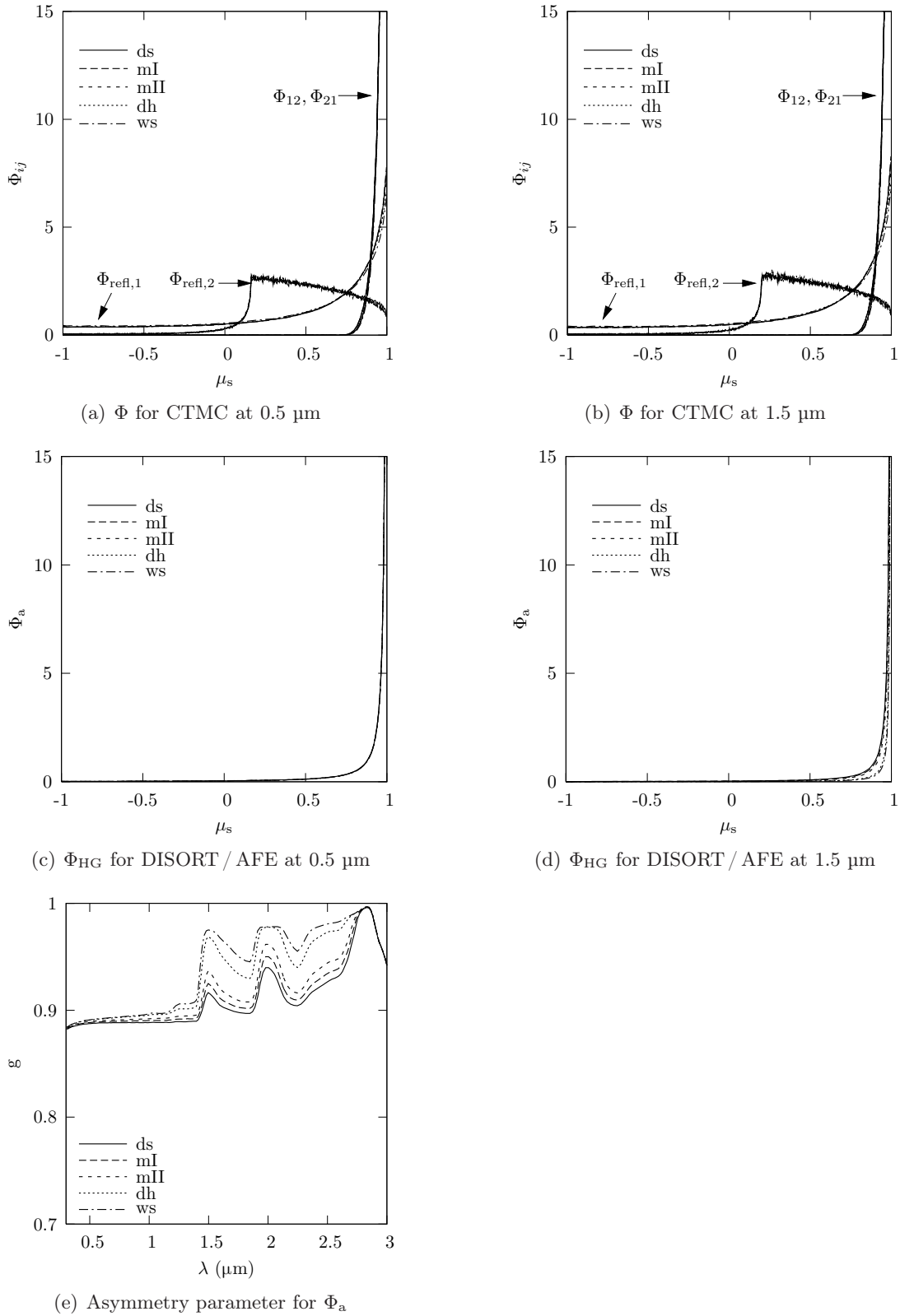


**Figure 3.9:** Phase functions  $\Phi$  [-] at  $\lambda = 0.5 \mu\text{m}$  and  $\lambda = 1.5 \mu\text{m}$  for CTMC model (a)–(b) and DISORT and AFE solution (c)–(d) as well as Mie theory asymmetry parameter  $g$  [-].

In contrast to all  $\Phi_{ij}$  for the CTMC model,  $\Phi_a$  does show a slight wavelength and snow type dependence: For snow samples with a low SSA (especially ws and dh) an even more-pronounced forward scattering can be discerned at  $\lambda = 1.5 \mu\text{m}$  in Figure 3.9(d), but not at  $\lambda = 0.5 \mu\text{m}$ . This phenomenon can be understood by the shape of  $g$  in Figure 3.9(e): For visible light (at  $\lambda = 0.5 \mu\text{m}$ )  $g$  is independent of SSA and thus snow type, but at longer wavelengths  $g$  starts to fan out (at  $\lambda = 1.5 \mu\text{m}$  the variation of  $g$  for the 5 snow samples is about 10%). Here,  $g$  increases with decreasing SSA (increasing OED) of the snow samples. Along with the asymmetry parameter the scattering phase function  $\Phi_a = \Phi_{\text{HG}}$  is more forward-scattering for snow samples with a lower SSA.

The comparison of all particle- and pore-level radiative properties for the three approaches to model radiative transfer in snow shows some qualitative similarities but also great differences. The disagreement is already seen in the respective number of resulting scattering phase functions, scattering and extinction coefficients. Due to the highly differing assumptions and calculation methodologies a direct quantitative comparison of these microscopic radiative properties is not feasible. However, the observed similarities and differences on the particle and pore scale can help to analyze and better understand possible discrepancies in macroscopic flux calculations between CTMC, DISORT and AFE simulations in Section 3.5.3.

### 3.5.3 Macroscopic snow-slab radiative properties

In contrast to the particle- and pore-scale radiative properties, flux calculations for a larger snow slab by CTMC, DISORT and AFE simulations can be compared directly. Here, this is done for the macroscopic radiative properties reflectance  $R$  and transmittance  $Tr$  as defined in Equations (3.9) and (3.10). The simulations are performed for snow slabs with thickness  $s_{\text{slab}} = 4 \text{ cm}$  and model input parameters calculated in Section 3.5.2 for the 5 snow types specified in Table 3.2 and Figure 3.6.

#### Comparison: CTMC for the true 3D microstructure and DISORT

First, CTMC and DISORT model are compared in detail. In Figure 3.10 spectral reflectance and transmittance are calculated by the CTMC model for a collimated incident flux along the snow surface normal and for a diffuse incident flux. As expected  $R$  increases and  $Tr$  decreases slightly for diffuse irradiation. This is due to two factors: (i) an increased path length of radiation which does not enter the snow slab in the normal direction to the snow surface and (ii) if radiation is transmitted through the entire snow slab more non-forward scattering events are required in the predominantly forward-scattering material snow (see phase functions in Figure 3.9). For the 5 presented snow types  $R$  increases by up to 15% and  $Tr$  decreases by up to 35% for  $\lambda < 1 \mu\text{m}$ . The general trend, however, remains the same for all snow types. Snow types with a higher SSA (lower OED) reflect more radiation and transmit less than snow types with a lower SSA. Deviations from this rule (e.g. ws vs. dh snow in Figure 3.10(b)) are observable only if the effect of higher absorption due to a higher snow density dominates.

In general, reflectance values are very high, with values around 0.9 at visible wavelengths, compared to other materials like water or soil. They only start to drop off signif-

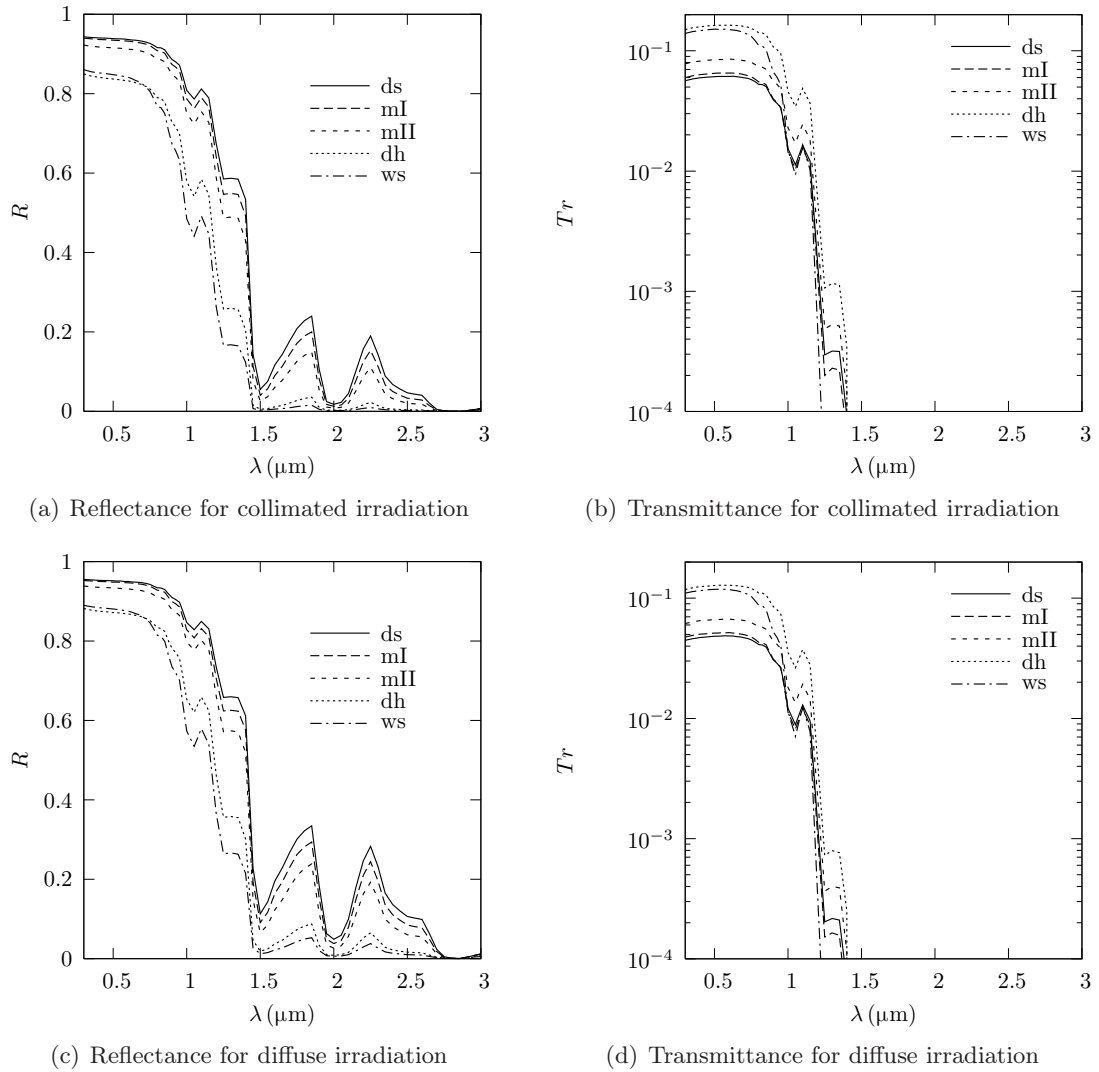


**Figure 3.10:** Reflectance  $R$  [–] and transmittance  $Tr$  calculated by the CTMC model for 5 snow types with snow slab thickness  $s_{\text{slab}} = 4$  cm.

icantly in the NIR spectrum at approximately 750  $\mu\text{m}$ , where absorption in ice increases significantly (see Figure 2.3). At this snow slab thickness of  $s_{\text{slab}} = 4$  cm transmittance is already low with values  $Tr \approx 0.1$  at visible wavelengths and decreases further in the NIR. These observations once again confirm that radiative transfer in snow is dominated by scattering in the visible and NIR part of the spectrum.

Normalized differences between DISORT and CTMC calculations of reflectance and transmittance are plotted in Figure 3.11. There are several striking differences.

For a collimated incident flux (shown in Figures 3.11(a) and 3.11(b)) at  $\lambda < 1$   $\mu\text{m}$  DISORT- and CTMC-calculated reflectance differs by up to 20% (for ws snow) while transmittance differs by up to 121% (for mI snow). For diffuse irradiation (Figures 3.11(c) and 3.11(d)) DISORT- and CTMC-modeled reflectance and transmittance values differ by up to 16% and 121%, respectively. In general, the trend and values are very similar for both considered incident fluxes, except for wavelengths where the calculated signals of all snow types are very low. This shows (for non-directional and normally incident radiation) that the differences in reflectance and transmittance calculations between the two models are not introduced by the chosen direction of incidence, a user-specified boundary condition. Instead, the differences are caused by the inherently different model approach.

At longer wavelengths the relative difference between DISORT and CTMC results increases. Here, small absolute changes in  $R$  and  $Tr$  can already mean a large relative difference due to the smaller absolute values of  $R$  and  $Tr$ . For all wavelengths where the signal is still strong enough to be analyzed reliably (for  $R$ :  $\lambda < 2.7$   $\mu\text{m}$ , for  $Tr$ :  $\lambda < 1.4$   $\mu\text{m}$ ) DISORT simulations yield a lower reflectance and a higher transmittance than the corresponding CTMC calculations.

The best agreement for reflectance values between both models is found for ds, mI and mII snow in Figures 3.11(a) and 3.11(c). This is expected as the DISORT assumptions of (i) a homogeneous scattering medium consisting of ice spheres and (ii) a dilute collection of spheres, i.e. independently scattering spheres, are least fulfilled for the coarser microstructure and higher density of ws and dh snow (Table 3.2 and Figure 3.6).

For transmittance the best agreement between DISORT and CTMC simulation results is still found for ds snow. Surprisingly, however, mI and mII snow with their low density and rounded microstructure show the worst agreement over most of the spectral range. Hence, this cannot be as readily explained as the reflectance results by a break-down of the DISORT assumptions. Here, other radiative transfer characteristics have to come into play, which are not as decisive for reflectance calculations. This could be the different relative contribution of absorption within the ice matrix to reflectance and transmittance calculations for the different snow types. This may ultimately lead to different agreement patterns for reflectance and transmittance for the different snow types.

### Comparison to CTMC for equivalent microstructure of OED spheres (IOSS)

To better separate and quantify the effects that lead to the differences in reflectance and transmittance between DISORT and CTMC approach a simplified snow microstructure of OED ice spheres can be used as input to CTMC simulations. The results then give the ray-tracing results according to the CTMC model (Section 3.3.1) for a snow microstructure as it is considered in DISORT (Section 3.2).

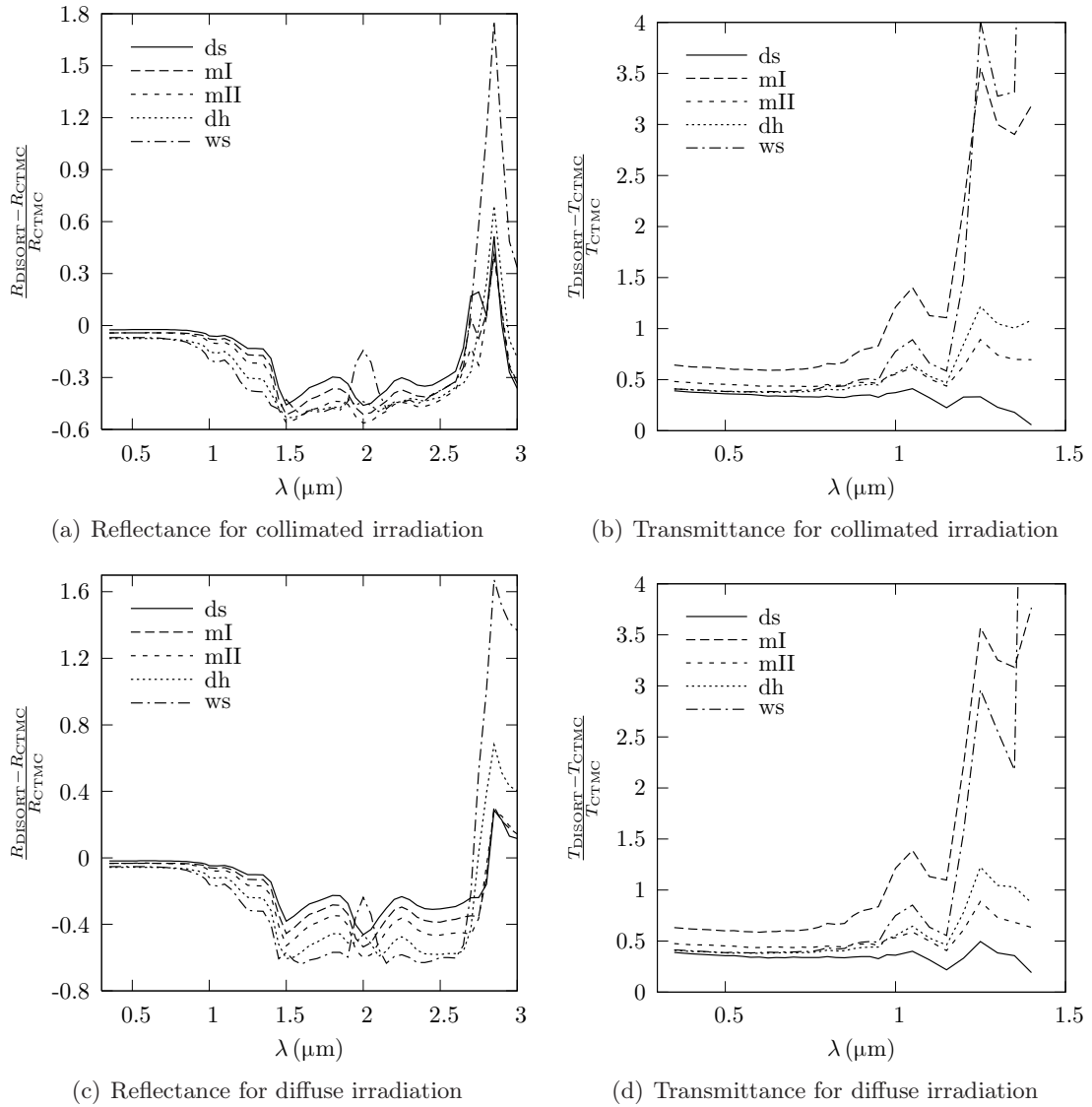


**Figure 3.11:** Normalized difference between DISORT and CTMC model for reflectance  $R_{\text{DISORT}/\text{CTMC}}$  and transmittance  $T_{\text{DISORT}/\text{CTMC}}$  calculations for 5 snow types. Reference CTMC values are plotted in Figure 3.10. For  $\lambda > 1.5 \mu\text{m}$  transmittance values are very low and thus yield very large relative differences. So, the plot is truncated at  $1.5 \mu\text{m}$ .

The two effects which are analyzed by this methodology are: (i) the introduction of an equivalent microstructure versus the incorporation of the exact snow sample morphology and (ii) the solution of only one effective RTE (3.6) versus two coupled RTEs (3.7).

The considered equivalent snow microstructure is an artificially generated packed bed of identical overlapping semi-transparent spheres (IOSS). For the IOSS morphology snow porosity  $\varepsilon = \frac{\rho_{\text{snow}}}{\rho_{\text{ice}}}$  and specific surface area  $A_0$  of IOSS are given by *Tancrez and Taine* (2004):

$$\varepsilon_{\text{IOSS}} = \exp\left(-\frac{\pi}{6}n_V d_{\text{IOSS}}^3\right), \quad (3.20)$$

$$A_{0,\text{IOSS}} = -\frac{6\varepsilon_{\text{IOSS}} \ln \varepsilon_{\text{IOSS}}}{d_{\text{IOSS}}}. \quad (3.21)$$

Here,  $n_V$  is the number of spheres per volume and  $d_{\text{IOSS}}$  is the diameter of the spheres.

Three types of IOSS are generated: (i) with  $\varepsilon_{\text{IOSS}}$  equal to the porosity of the corresponding CT-scan  $\varepsilon_{\text{CT}}$  (for the density given in Table 3.3) and with  $d_{\text{IOSS}} = d_{\text{CT}}$ , where  $d_{\text{CT}}$  is defined as the mean diameter of the biggest spherical structure element that fits fully inside the ice matrix obtained from Figure 3.6; (ii) with  $A_{0,\text{IOSS}}$  equal to the corresponding SSA  $A_{0,\text{CT}}$  of the snow samples in Table 3.3 and  $\varepsilon_{\text{IOSS}} = \varepsilon_{\text{CT}}$ ; and (iii) with  $A_{0,\text{IOSS}} = A_{0,\text{CT}}$  and  $d_{\text{IOSS}} = d_{\text{CT}}$ .

Reflectance and transmittance calculations with the CTMC model for these three IOSS morphologies are compared to CTMC results for the true CT-scanned microstructure and to DISORT simulations. The normalized 2-norm  $\xi$  is used to quantify the differences for the same 5 snow samples (characterized in Table 3.3 and Figure 3.6):

$$\xi_R = \frac{\|R_{\text{IOSS}/\text{DISORT}} - R_{\text{CT}/\text{DISORT}}\|}{\|R_{\text{CT}/\text{DISORT}}\|}, \quad (3.22)$$

$$\xi_{Tr} = \frac{\|T_{\text{IOSS}/\text{DISORT}} - T_{\text{CT}/\text{DISORT}}\|}{\|T_{\text{CT}/\text{DISORT}}\|}. \quad (3.23)$$

For a snow slab thickness  $s_{\text{slab}} = 4$  cm and collimated irradiation, Figure 3.12 shows the entire spectrally resolved reflectance and transmittance calculations for ds and ws snow. Table 3.4 then only lists the 2-norms according to Equations 3.22 and 3.23 for all 5 snow samples.

In Table 3.4 CTMC calculations of  $R$  show that for all 5 snow types IOSS with  $A_{0,\text{IOSS}} = A_{0,\text{CT}}$  and  $\varepsilon_{\text{IOSS}} = \varepsilon_{\text{CT}}$  best approximate the true snow morphology across the entire spectrum. This is the microstructural simplification by a collection of OED spheres as it is also assumed for the DISORT approach. The biggest deviation from the reflectance calculated with the corresponding true CT-scanned microstructure is found for a slab of ds snow with  $\xi_R = 0.13$ . Nevertheless, using IOSS with  $A_{0,\text{IOSS}} = A_{0,\text{CT}}$  and  $\varepsilon_{\text{IOSS}} = \varepsilon_{\text{CT}}$  significantly reduces the deviation to  $\xi_R = 0.02$ . This is comparable to deviations for all other snow types at this best-fitting equivalent IOSS snow microstructure. Calculating  $Tr$  generally leads to much bigger differences  $\xi_{Tr}$  since the absolute values of  $Tr$  are lower, especially at longer wavelengths (illustrated for ds and ws snow in Figure 3.12).

For  $Tr$  the best-fitting equivalent IOSS microstructure is also obtained with  $A_{0,\text{IOSS}} = A_{0,\text{CT}}$  and  $\varepsilon_{\text{IOSS}} = \varepsilon_{\text{CT}}$ . Only for ml snow IOSS with  $d_{\text{IOSS}} = d_{\text{CT}}$  and  $\varepsilon_{\text{IOSS}} = \varepsilon_{\text{CT}}$  clearly

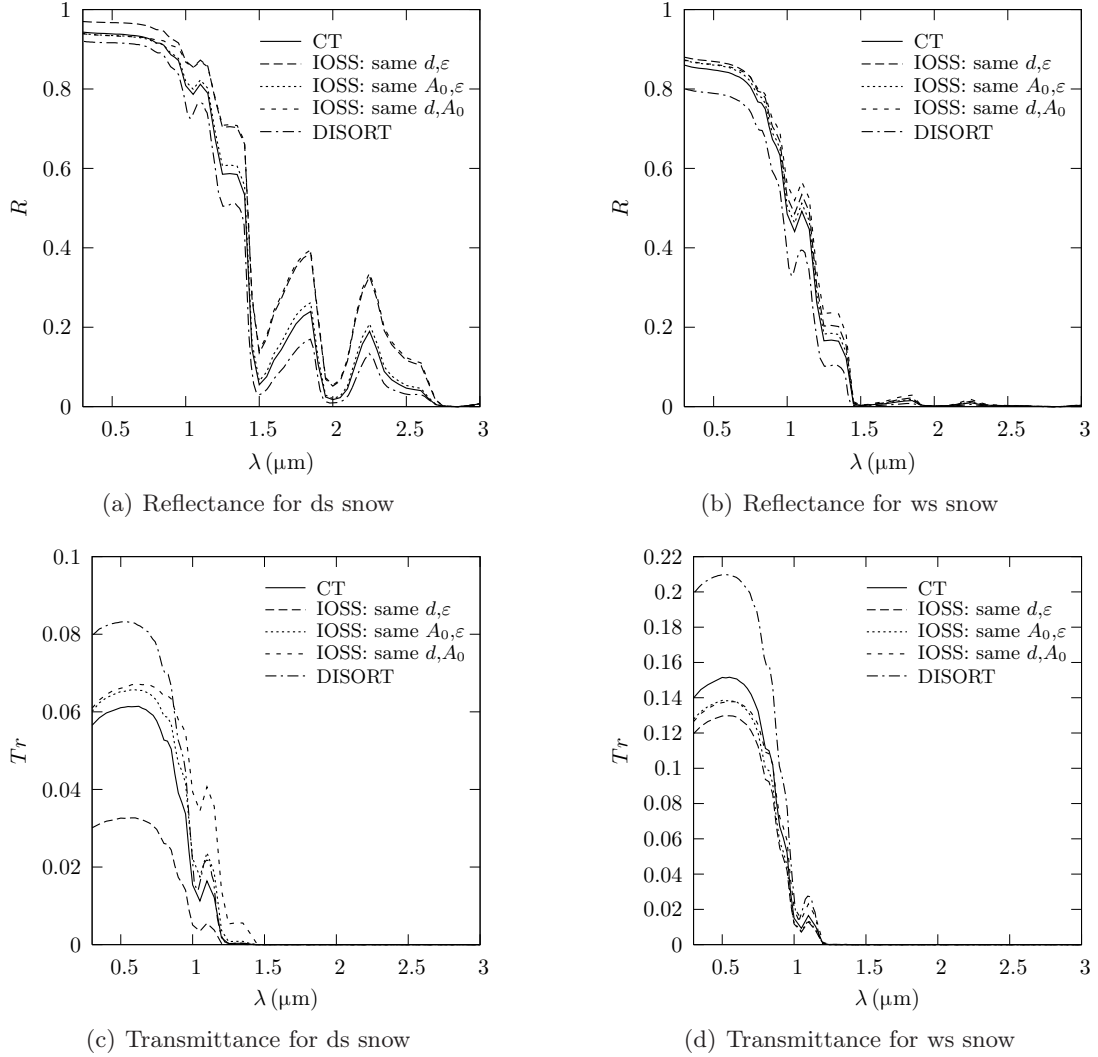


**Figure 3.12:** Reflectance  $R$  [–] and transmittance  $Tr$  for ds and ws snow samples (see Table 3.3 and Figure 3.6) and a snow slab thickness  $s_{\text{slab}} = 4$  cm. In each figure results are shown for the CTMC model based on the true 3D snow microstructure, CTMC simulations for an equivalent microstructure with 3 types of IOSS and the DISORT approach.

**Table 3.4:** Normalized 2-norms  $\xi$  for reflectance  $R$  and transmittance  $Tr$  of all 5 snow types (characterized in Table 3.3 and Figure 3.6). Values are calculated by the CTMC model based on the true 3D snow microstructure (CTMC), CTMC simulations for an equivalent microstructure with 3 types of IOSS (IOSS) and the DISORT approach. The type of IOSS is indicated by the IOSS parameters that match the corresponding parameters of the CT-scans.

Id	CTMC vs. $d, \varepsilon$ -IOSS		CTMC vs. $A_0, \varepsilon$ -IOSS		CTMC vs. $d, A_0$ -IOSS		DISORT vs. $A_0, \varepsilon$ -IOSS		CTMC vs. DISORT	
	$\xi_R$	$\xi_{Tr}$	$\xi_R$	$\xi_{Tr}$	$\xi_R$	$\xi_{Tr}$	$\xi_R$	$\xi_{Tr}$	$\xi_R$	$\xi_{Tr}$
ds	0.12	0.49	0.02	0.11	0.13	0.28	0.08	0.19	0.06	0.06
mI	0.08	0.23	0.02	0.31	0.09	0.49	0.09	0.21	0.08	0.29
mII	0.06	0.24	0.01	0.14	0.06	0.26	0.09	0.22	0.08	0.14
dh	0.09	0.30	0.02	0.05	0.07	0.19	0.13	0.32	0.10	0.10
ws	0.04	0.15	0.02	0.09	0.07	0.08	0.14	0.35	0.10	0.10

approximate the true snow morphology better. Transmittance calculations for snow slabs of ds, mI and mII snow yield higher deviations than those for the denser snow types dh and ws. Here, a slab of mI snow is worst approximated by IOSS ( $\xi_{Tr} = 0.23$ ) while a slab of dh snow is best approximated ( $\xi_{Tr} = 0.05$ ).

Solving one apparent RTE in DISORT instead of two coupled RTEs by ray tracing generally leads to an underestimation of  $R$  (illustrated for ds and ws snow in Figure 3.12). The biggest difference between DISORT and IOSS calculations with the same  $A_0$  and  $\varepsilon$  in Table 3.4 is found for ws snow with  $\xi_R = 0.14$ . A general trend can also be observed: The difference increases with decreasing porosity, i.e. the higher the snow density the worse is the assumption of dilute scattering snow grains in the DISORT model. For all snow slabs the normalized difference  $\xi_R$  for DISORT vs.  $A_0, \varepsilon$ -IOSS is a factor of 5 to 10 higher than for CTMC vs.  $A_0, \varepsilon$ -IOSS.

Corresponding to the underestimation of  $R$ , DISORT overestimates  $Tr$  compared to the CTMC results. As for reflectance, the biggest difference between DISORT and IOSS calculations with the same  $A_0$  and  $\varepsilon$  in Table 3.4 is found for ws snow with  $\xi_{Tr} = 0.35$ .  $\xi_{Tr}$  decreases with increasing porosity (decreasing density). Furthermore, the deviations which are introduced by simplifying the microstructure by IOSS are generally smaller by up to a factor of 6 than the deviations caused by solving only one apparent RTE in DISORT. Only for mI snow the influence of a simplified microstructure is approximately the same as the influence of simplified radiative transfer modeling ( $\xi_{Tr} = 0.23$  vs.  $\xi_{Tr} = 0.21$ , respectively).

One feature that is not observed in the reflectance analysis is the convergence of the two transmittance curves for DISORT and  $A_0, \varepsilon$ -IOSS calculations at wavelengths around 1  $\mu\text{m}$ . This is seen for the slabs of ds, mI and mII snow but not for the denser dh and ws snow types (Figure 3.12(c) vs. 3.12(d)). At NIR wavelengths the importance of absorption within the ice matrix increases. So, the explicit description of scattering by the model is less crucial for the calculated NIR transmittance. This means that the differences in transmittance at shorter wavelengths, which are caused by the respective scattering description within the DISORT and  $A_0, \varepsilon$ -IOSS CTMC model, are dominated

by the identical description of absorption at wavelengths  $\lambda > 1 \mu\text{m}$ . For the denser snow samples of dh and ws snow the a-priori assumption of dilute independently scattering spherical grains does not hold that well anymore. Thus, a convergence of the two models for the same equivalent snow microstructure cannot be expected for dense snow, even at longer wavelengths, where absorption dominates the transmittance characteristics.

The most important result of this analysis is that simplifying radiative transfer theory by solving only one RTE in DISORT has a stronger influence on reflectance and transmittance than simplifying the true snow microstructure by an equivalent collection of OED ice spheres. The latter effect accounts for a fraction of  $\sim 1$  to 20% in reflectance and 16 to 63% in transmittance of the entire deviation from the full CTMC simulations. Only for mI snow a larger  $\xi_{Tr}$  is found for CTMC vs.  $A_{0,\varepsilon}$ -IOSS calculations than for DISORT vs.  $A_{0,\varepsilon}$ -IOSS calculations.

### Comparison to AFE

The final part of analyzing current approaches to model radiative transfer in snow is the comparison of overall flux extinction calculations by the AFE solution (explained in Section 3.4) with reflectance and transmittance values obtained from the calculations thus far. Here, transmittance is again calculated for snow slabs of the same 5 snow types (characterized in Table 3.3 and Figure 3.6) and with a snow slab thickness  $s_{\text{slab}} = 4 \text{ cm}$ . Reflectance, however, can only be calculated for one snow slab thickness  $s_{\text{slab}} \rightarrow \infty$  with the AFE solution.

It is evident from the description in Section 3.4 that, in a strict sense, the problem geometry of a finite snow slab thickness and external light source is not included in the derivation of the AFE solution. Nevertheless, the simplicity of the AFE approach merits investigating whether it might still be possible to describe radiative transfer in snow with a sufficient accuracy to obtain usable results for later optical measurement methods.

Corresponding transmittance and reflectance values calculated by AFE theory in Equations (3.18) and (3.19) and by DISORT simulations are plotted in Figure 3.13. The results of both models differ significantly for all snow types. Here, the relative differences for transmittance calculations are bigger than for reflectance calculations.

As for all transmittance calculations so far,  $Tr$  values in Figure 3.13(a) approach zero at  $\lambda \approx 1.2 \mu\text{m}$  and are not analyzed for longer wavelengths. For the spectrum up to this wavelength, two major points can already be noted without a detailed analysis: (i) The two approaches to calculate transmittance yield different results for the same snow slabs by a factor of 5 to 10 across the entire visible and NIR part of the spectrum. And (ii) across most of the spectrum, the 5 transmittance curves calculated by the AFE solution can hardly be distinguished from each other compared to the clearly differing DISORT results, despite the strong differences in snow type characterization in Table 3.3.

It has already been demonstrated that DISORT calculations yield higher transmittance values than CTMC simulations. AFE results, however, far exceed these elevated DISORT-calculated transmittance values. This can be explained by the finite extension of the snow slab along the  $z$ -direction of irradiation. Thus, all radiation which reaches the snow slab boundaries is lost. This is analogous to putting a frame of totally absorbing black panels around the considered snow slab. This boundary effect gives rise to a lower transmittance

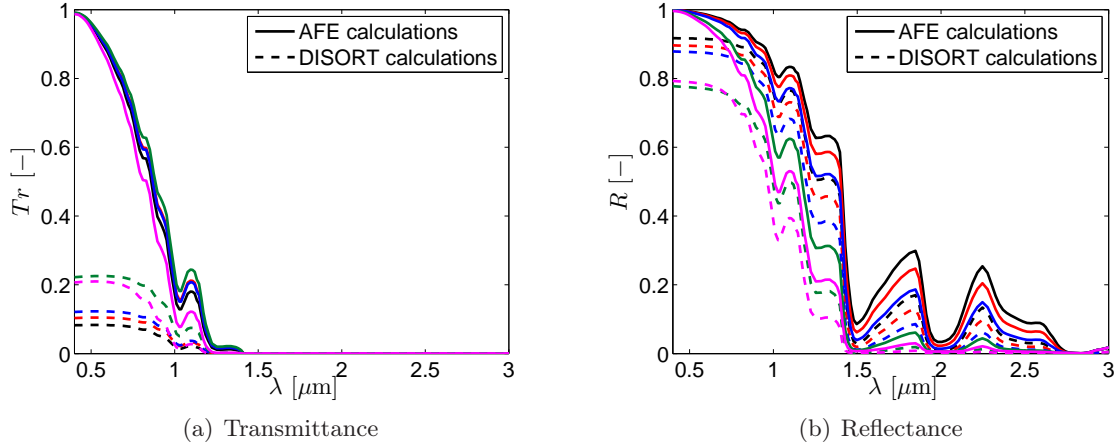


**Figure 3.13:** Comparison of AFE solution and DISORT radiative transfer simulations for 5 snow slabs with  $s_{\text{slab}} = 4$  cm. The 5 snow types (black: ds, red: mI, blue: mII, green: dh, magenta: ws snow) are characterized in Table 3.3 and Figure 3.6.

than for the conditions where the AFE Equations (3.17) and (3.18) strictly apply. For a finite snow slab of thickness  $s_{\text{slab}} = 4$  cm part of the radiation from the light source outside of the slab and all radiation reaching the depth  $s = 4$  cm away from the light source escapes from the snow slab and is lost. For an infinite snow slab as it is assumed in the derivation of the AFE solution part of the light is now scattered backwards due to the further extension of the snow slab. Further scattering into the opposite direction can then once again contribute to the radiative flux in between light source and  $s = 4$  cm.

Furthermore, DISORT results are much more sensitive to the model input parameters density and SSA which are used for both DISORT and AFE calculations. Especially at visible wavelengths the AFE transmittance curves for all 5 snow types are hardly separated. Only the high-density slab of ws snow ( $\rho = 605 \text{ kg m}^{-3}$ , plotted as magenta line in Figure 3.13) has a visibly lower transmittance across the entire spectrum than all other snow types according to the AFE solution. Other curves start to be distinguishable from each other by visual inspection in the NIR for  $\lambda \gtrsim 0.75 \mu\text{m}$ , until they finally collapse and vanish at  $\lambda \approx 1.2 \mu\text{m}$ . So, transmittance curves calculated by the AFE solution are only distinguishable where absorption inside the ice matrix dominates radiative transfer. This is caused either by a strong density difference in the low-absorption regime for visible light or by the strong increase in the imaginary part of the ice refractive index (see Figure 2.3) in the NIR.

Reflectance values calculated by the AFE solution and plotted in Figure 3.13(b) are also higher than the corresponding DISORT results. The absolute difference between the two models is 0.1 to 0.2 at visible and NIR wavelengths up to  $\lambda \approx 1.5 \mu\text{m}$ . This is surprising and may seem very unrealistic as adding reflectance and transmittance for the AFE solution yields values  $R + Tr > 1$ . This is caused by the different boundary conditions which are actually assumed in calculating  $R$  and  $Tr$  by the AFE solution: While the finite extension of the snow slab is considered in the transmittance calculation in the form of

the optical depth in Equation (3.18) it is completely neglected in the derivation of the reflectance formula Equation (3.19). Thus, plotted  $R$  is the reflectance of an infinite snow slab according to the AFE solution which clearly overestimates the reflectance of the snow slab with  $s_{\text{slab}} = 4$  cm. This is especially evident at shorter wavelengths. Here, light absorption inside the ice matrix is still weak which leads to a greater penetration depth of the radiation and to a greater effect of the boundary condition of a snow slab with finite thickness.

As already found for transmittance, DISORT reflectance simulations are more sensitive to the model input parameters than the corresponding AFE results. For AFE reflectance calculations, however, the only model input parameter is snow SSA (or OED). The a-priori assumption of an infinitely thick snow slab renders possible density effects irrelevant for reflectance in the AFE derivation.

#### 3.5.4 First conclusions and outlook

The comparison of the 3 presented approaches to model radiative transfer in snow suggests that the use of the AFE solution is indeed too limited to be used for general optical measurement methods of snow properties. CTMC and DISORT calculations, however, show a closer agreement between each other than compared to the AFE solution. Nevertheless, significant differences are still observed, especially in modeling transmittance.

The observed differences are mainly the result of simplifying radiative transfer theory in the form of the fundamental RTE. Applying the CTMC model to the true 3D snow microstructure and an equivalent collection of OED ice spheres suggests that approximating the true snow microstructure by this equivalent microstructure has a smaller effect on reflectance and transmittance calculations. Recent studies on radiative transfer in snow, however, have only focused on this important but less decisive aspect (*Xie et al.*, 2006; *Picard et al.*, 2009) of the analysis. Thus, a better understanding of the different approaches to solve the RTE and not only how to describe the scattering properties of the material snow is crucial for modeling radiative transfer in snow.

After analyzing different radiative transfer models, their results are compared to actual reflectance and transmittance measurements. Then, it can be determined which models agree best with the measurements and whether a model can not only be applied to obtain optical snow characteristics but also to derive other physical properties from optical measurements. This is investigated for snow SSA (or OED) and density in the next Chapters 4 to 6.

## 4 InfraSnow: Diffuse NIR Reflectance Measurements to Determine Snow Grain Size (OED)

Defined by Equation 1.1, snow grain size (OED) is equivalent to snow specific surface area (SSA). Hence, OED is one crucial microstructural parameter to describe the radiative and mechanical properties of snow as detailed in Chapter 1.

In recent years, several methods to determine snow OED by NIR reflectance measurements have been performed successfully (*Matzl and Schneebeli, 2006; Painter et al., 2007; Gallet et al., 2009; Arnaud et al., 2011*, explained in Chapter 1.2.2). They all found no effect of other microstructural parameters like density or a snow-structure shape parameter on their measurement methods. These optical and all non-optical measurement methods to determine OED outlined in Chapters 1.1 and 1.2 are not practical if many in-situ measurements at a high spatial and temporal resolution on the snow surface are desired. The InfraSnow (*Schneebeli et al., 2009*) has been developed to have a portable and affordable optical measurement device available which overcomes these limitations. While other methods require extracting a specified snow volume from the snow cover, cumbersome or expensive equipment like spectrometer, lasers or a large integrating sphere, the InfraSnow is designed with compact and standard optical and electronic components. This permits manufacturing costs < 10.000 USD and an easy assembly.

*Hug and Trunz (2006)* and *Frost (2008)* gave a detailed description of parts, assembly and the design at that time. They showed results of first test measurements on snow, too. However, they were not able to rigorously explain their optical measurements based on radiative transfer theory and modeling. Only a qualitative correlation between reflectance and OED could be established: measured reflectance increases with decreasing OED for most measurements.

A quantitative interpretation of the InfraSnow results including all defining microstructural parameters is the goal of this chapter. In contrast to classical NIR spectroscopy, a great part of usually expensive and time-intensive calibration measurements is avoided. Instead, the measurements are modeled by a fitting radiative transfer approach in snow to calibrate the measurement device. Only few calibration measurements by micro-CT are then required to validate this approach.

Here, the present design of the InfraSnow is introduced together with the measurement principles and requirements in Section 4.1. Then, the InfraSnow calibration is explained briefly in Section 4.2. The main focus will be on presenting and analyzing InfraSnow reflectance measurements for snow and standard materials in Section 4.3. Measurements and simulations show that an accurate and usable interpretation of the measurements is only possible if the optical properties of the measuring device, the probed material

snow and the interaction between the two are understood. Crucial factors that need to be considered in the interpretation are, primarily, a density- and OED-dependant snow sample volume and specular, i.e. mirror-like, reflections at the snow surface. It is not necessary, however, to (i) determine other parameters of the snow microstructure than OED and density or to (ii) use involved radiative transfer models based on the true 3D snow microstructure.

## 4.1 Design requirements and realization

Throughout this thesis only pure snow is considered. In order to neglect the influence of snow impurities like soot or sand on snow reflectance, NIR light has to be used for illumination (Chapter 1.2.2).

For consistent measurement results a closed unit with an internal well-characterized stable light source and a built-in detector is needed.

To measure consistent reflectance values across a macroscopically homogeneous snow sample, the influence of microscopic localized inhomogeneities should be minimized. E.g. a favorably-oriented snow crystal can lead to a bright highlight, which is caused by specular reflections at the ice-to-air interface. Including bright specular highlights in the overall reflectance signal complicates a correct interpretation, as these localized inhomogeneities have to be accounted for explicitly. A measurement method based on focused parallel illumination is more sensitive to possible localized inhomogeneities than a method based on diffusely illuminating a larger area. So, it is desirable to use diffuse illumination and only measure diffuse reflectance. To further reduce the influence of localized inhomogeneities, the measurement signal can be integrated over a large area.

These requirements are met by an experimental setup consisting of an LED inside an integrating sphere to diffusely illuminate the snow surface and another integrating sphere with built-in detector to measure the integrated diffuse reflectance. This design is well-known and has been tested in many applications of classical reflectance spectroscopy. However, the measuring principle of the *InfraSnow* differs from this traditional approach to permit a more compact design: One integrating sphere serves both as diffuse light source with a simple LED and as diffuse reflectance detector with a standard photodiode. A sketch of the optical measuring unit without electronics, user interface and housing is shown in Figure 4.1. A standard NIR LED at 950 nm (Siemens SFH 409) is chosen as light source and a Hamamatsu S2387 Si photodiode (sensitive to visible and NIR radiation) as detector. The footprint of the integrating-sphere opening is  $\sim 3$  cm in diameter.

A short measurement time and automated analysis are achieved by installing and wiring suitable compact electronic components (like microcontroller, signal amplifier, battery and LCD display) to trigger the measurements, perform an automated analysis and deliver an immediate measurement output (*Hug and Trunz, 2006*).

One measurement and analysis takes  $\sim 15$  s, which is fast enough to perform many measurements within a reasonable time frame. The output value is the mean of 35 separate measurements with an integration time of 100 ms each. This integration time permits a good signal power, while the number of 35 measurements to be averaged is high enough and commonly used in spectroscopy to obtain a good signal-to-noise ratio. For these settings and the used LED and detector the signal-to-noise ratio  $> 10^3$ .

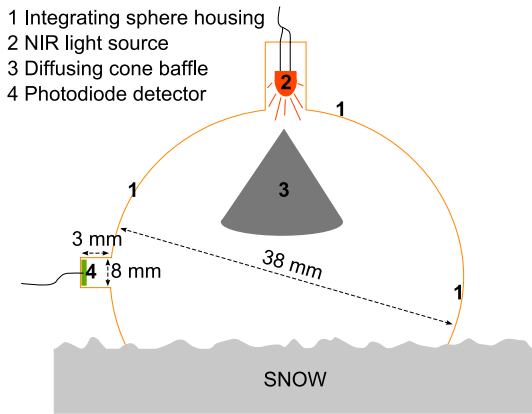


**Figure 4.1:** Sketch of InfraSnow measuring principle (not true to scale). One integrating sphere serves both as diffuse light source and as detector to measure diffuse reflectance.



**Figure 4.2:** Top and bottom view of the operational InfraSnow device. For measurements the InfraSnow is placed on the snow surface. The maximum lateral extensions are 23 cm x 13 cm. The top view reveals the user interface of LCD display and push buttons. On the bottom side the golden integrating sphere, illustrated in Figure 4.1, can be seen through the opening inside an aluminum frame.

Usability in the field demands that the device be portable, simple to operate and not disturbed by exterior influences like wet weather, cold, wind and solar radiation. Therefore, all electronic components are enclosed in a hard, sealed and weather-resistant outer casing to keep out humidity. A top and bottom view of the entire InfraSnow device is shown in Figure 4.2. The user interface consists of push buttons to start measurements and download calibration data from a PC or upload measurement data. The communication is handled by Bluetooth®.

For outdoor use in the field the temperature dependance of the electronic components has to be accounted for. To this end temperature sensors can be attached to key electronic components inside the device. One additional sensor can be installed on the outer casing to measure the snow surface temperature.

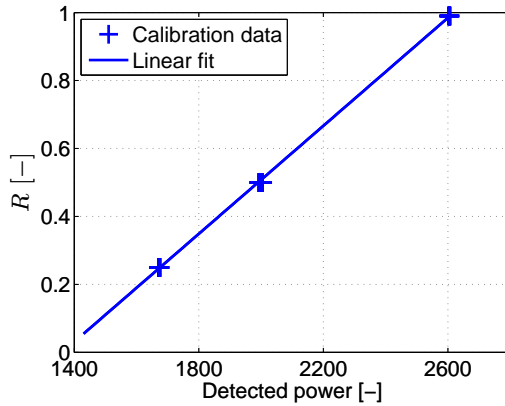


**Figure 4.3:** Calibration of the InfraSnow detected power against three reflectance standards of  $R = 25\%$ ,  $50\%$  and  $99\%$ . Each standard is measured 5 times. The coefficient of determination for the linear fit  $> 0.99$ .

## 4.2 Reflectance calibration

As mentioned in Section 4.1, a temperature calibration has to be performed in advance to account for a varying temperature during field measurements. The temperature calibration is obtained by fitting a linear relation between detected power and measured temperatures at two key locations inside the InfraSnow device. This is purely electronics and will not be considered in the following any more, since all optical test measurements in Section 4.3 are performed in a cold laboratory under equilibrium temperature conditions. A detailed description of the temperature calibration can be found in *Frost* (2008).

Calibration of the actual optical measurements is achieved by calibrating the output signal power against three diffuse reflectance standards of  $25\%$ ,  $50\%$  and  $99\%$  reflectance. A linear calibration curve is assumed according to the linear relation between detected light intensity and output current of a photodiode. The fit is excellent (Figure 4.3).

Once the correct relation between snow reflectance and OED is found by measurements and simulations for the InfraSnow (in Section 4.3.3), the calibration can be broadened to also determine snow OED instantly.

## 4.3 Reflectance measurements and analysis

Before performing reflectance measurements on snow, the InfraSnow device is tested on materials where radiative transfer is understood more easily. This is done in Section 4.3.1 for homogeneous materials where no significant volume-scattering occurs, i.e. where radiation is partially absorbed or reflected right at the surface of the probed material. For those materials, the inherent measurement stability of the InfraSnow device can be analyzed. Reflectance measurements for snow are presented in Sections 4.3.2 and 4.3.3. By understanding the InfraSnow results for non volume-scattering materials first, the effects caused by more complex radiative transfer in snow can be singled out and analyzed more clearly.

The aim of the presented analysis is to understand and quantify the impact of the InfraSnow device and all relevant microstructural parameters on the measured reflectance

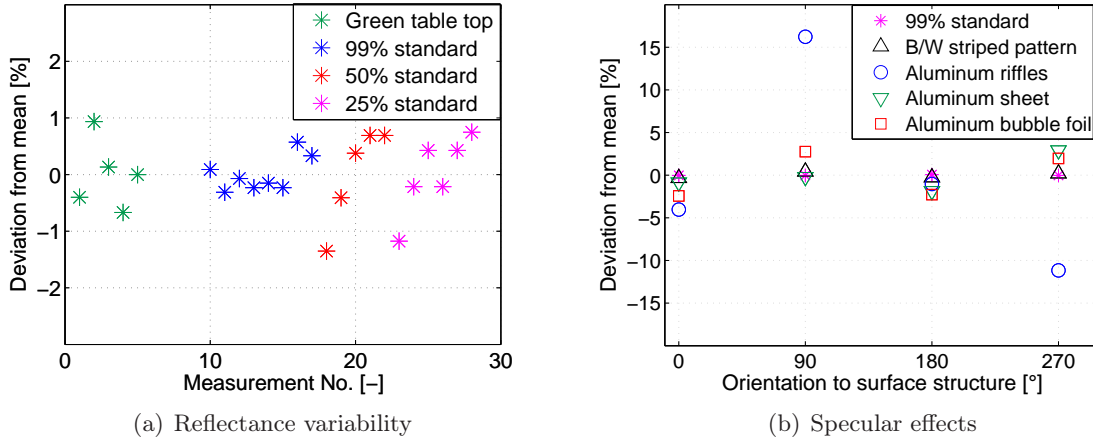


**Figure 4.4:** InfraSnow measurements on standard materials. **(a)** Relative reflectance variability for each measurement and from each material’s mean: a green table top (mean  $\approx 59\%$ ) and 3 Spectralon<sup>®</sup> diffuse reflectance standards. **(b)** Relative reflectance variability for 4 orientations of the InfraSnow in steps of  $90^\circ$ . Each marker represents the mean of 3 to 5 separate measurements at the same location and orientation, taken in rapid succession.

of snow. Then, snow OED can be determined by InfraSnow reflectance measurements once all other relevant microstructural parameters are known.

#### 4.3.1 Measurement variability for non volume-scattering materials

First, reflectance is measured on smooth, homogeneous surface-reflecting materials with the InfraSnow according to the calibration in Figure 4.3. The reflectance variability for a green table top and 3 perfectly diffuse reflectance standards is shown in Figure 4.4(a). The measurements are performed across the entire area of  $5 \times 5 \text{ cm}^2$  for the standards and across  $15 \times 15 \text{ cm}^2$  on the table top. A maximum relative measurement variability of less than 1.5% is found. This is the inherent measurement variability of the InfraSnow since all exterior influences can be neglected.

Figure 4.4(b) shows the reflectance measurement variability on uneven and optically inhomogeneous surface-reflecting materials. Orientation refers to the angle between InfraSnow longitudinal axis and the surface pattern of the probed material. The orientational variability for the optically inhomogeneous black-and-white-striped pattern on paper is not larger than the the variability seen for smooth and homogeneous materials in Figure 4.4(a) and the 99% diffuse reflectance standard.

However, all measurements on aluminum, a mirror-like specularly-reflecting surface, show a greater maximum relative variability than the 1.5% of inherent variability found in Figure 4.4(a). Uneven aluminum bubble foil and especially the V-shaped 3D aluminum ripple pattern cause a reflectance variability of up to 15%. Here, the variability is highly dependent on the orientation of the InfraSnow detector surface (see Figure 4.1) to the surface roughness features. This is a clear indication for a specular effect due to mirror reflections at the surface.

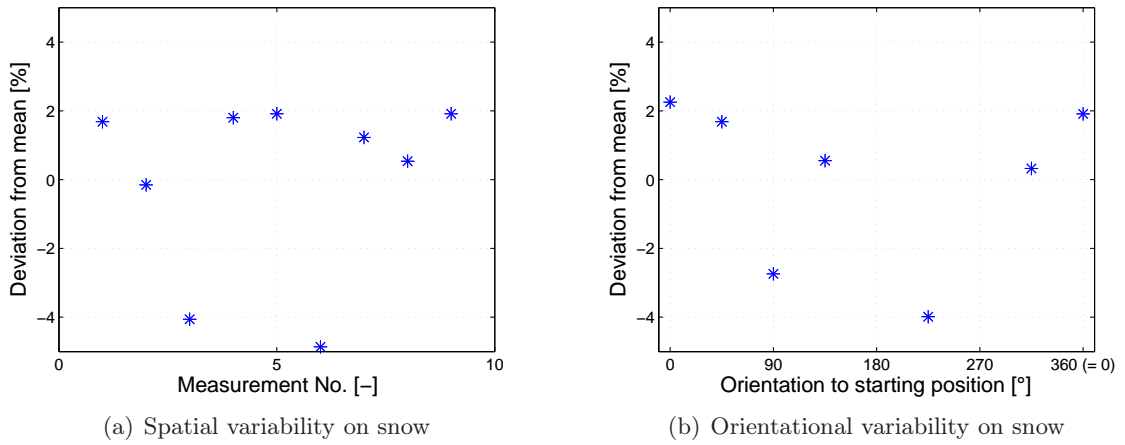


**Figure 4.5:** InfraSnow measurements of a natural snow block. **(a)** Relative reflectance variability across a  $10 \times 10 \text{ cm}^2$  patch on a smooth snow-block surface. **(b)** Relative reflectance variability at the same position for 6 orientations of the InfraSnow.

The symmetry of the aluminum bubble foil leads to the same measured reflectance at  $0^\circ$  and  $180^\circ$  and at  $90^\circ$  and  $270^\circ$ , respectively. This symmetry is not present for the slightly bent V-shaped elements of the self-made 3D aluminum ruffle pattern. Here, reflectance data show one orientation where the InfraSnow detector captures many specular reflections (at  $90^\circ$ , i.e. detector surface is orthogonal to the surface structure) and one where specular reflections are preferentially blocked (at  $270^\circ$ ) due to the bent structure elements.

These results lead to the conclusion that the InfraSnow reflectance measurements are very stable on smooth, homogeneous and diffusely-reflecting surfaces. However, the variability can increase significantly for uneven specularly-reflecting surface structures. This has to be remembered for a later analysis of InfraSnow measurements on snow. Pronounced roughness features like grooves at the snow surface can lead to specular reflections, for example, which falsify diffuse reflectance measurements when hitting the detector surface directly.

### 4.3.2 Measurement variability for snow

As for the surface-reflecting materials before, the measurement stability on snow is examined next. The relative measurement variability at one position (without moving the InfraSnow device between measurements) is below 0.5% on a snow block with a density of about  $400 \text{ kg/m}^3$  and a visibly smooth surface without cracks or indentations. The test includes the temporal stability over one hour and the influence of performing 12 measurements in rapid succession in a dark room or with ambient light, either fluorescent light in the laboratory or sunlight outdoors. This demonstrates the high reproducibility of the InfraSnow reflectance measurements and the insignificance of ambient light.

For the same snow block, a relative spatial variability of up to 5% from the mean reflectance value is measured. This is shown in Figure 4.5(a). Considering the high reproducibility of InfraSnow measurements at one position and the good inherent measurement

stability of the InfraSnow device, which was found in Section 4.3.1, this is an indication and measure for the substantial inhomogeneity of natural snow on the scale of cm. The variability of the snow microstructure cannot be recognized by a mere visual inspection.

In addition to the spatial variability, a maximum orientational variability at one measurement location of more than 4% from the mean is found in Figure 4.5(b). This means that specular reflections at the snow surface still affect the InfraSnow measurements despite the integrating sphere setup (Figure 4.1). For the probed snow block, the specular effects are not as pronounced as for the predominantly specularly-reflecting and uneven aluminum surface structures tested in Figure 4.4(b). The snow surface shows no visible unevenness. And still, the orientational variability is ten times the variability, which is found for the measurement reproducibility at one single location and orientation.

### 4.3.3 Comparison between measurements and models for snow

So far, only the measurement variability of the InfraSnow has been investigated. Now the measured reflectance values are compared to model results for the same snow block. Three different approaches to radiative transfer in snow are investigated: DISORT, FRED and AFE as they are introduced and explained in Chapters 3.2 to 3.4. All three models need as input the single-scattering parameters of optical equivalent ice spheres derived from the SSA of the true snow microstructure.

Four different snow blocks of 25 cm width and  $\sim 20$  cm thickness are used for the measurements. Their classification and characteristics are listed in Table 4.1. As input to the radiative transfer models, density and OED values are measured by micro-CT for 6 samples (with a volume of  $\sim 1$  cm<sup>3</sup>) of each snow block. The samples are taken at two locations inside the area which is covered by the InfraSnow integrating-sphere opening and at each cm for a depth of 3 cm below the snow surface. Thus, the density and OED variability measured by micro-CT yields an estimate of the natural snow variability inside the InfraSnow probing volume.

**Table 4.1:** Characteristics of 4 snow blocks for InfraSnow reflectance measurements: 2 consisting of rounded snow (rI, rII), 1 of wet and refrozen new snow (wns) and 1 of depth hoar snow (dhII). Classification according to *Fierz et al.* (2009). Given density, SSA and OED range is the range between respective minimum and maximum values determined by micro-CT measurements.

Id	Classification	Density [kg m <sup>-3</sup> ]	SSA [mm <sup>-1</sup> ]	OED [ $\mu$ m]
rI	RG	321 – 376	13.0 – 19.7	305 – 462
rII	RG	321 – 358	9.3 – 9.7	619 – 645
wns	MF	449 – 514	13.2 – 20.4	294 – 455
dhII	DH	248 – 321	8.1 – 8.4	714 – 740

#### Measurements vs. DISORT and AFE models

The presented InfraSnow reflectance measurements are subdivided into two groups for each snow block: spatial and orientational variability. To account for the spatial vari-

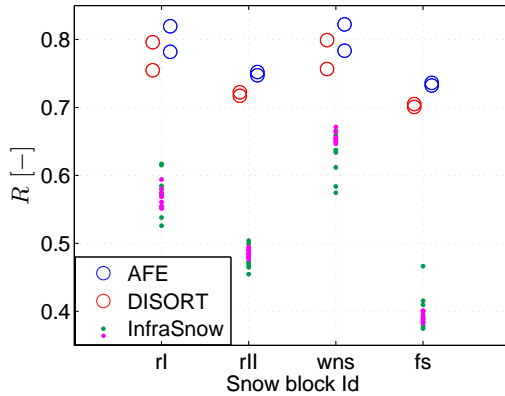


**Figure 4.6:** InfraSnow reflectance measurements, AFE and DISORT results for 4 snow blocks. Green dots denote the spatial variability and magenta dots the orientational variability of the measurements.

ability, 10 measurements are taken across a  $10 \times 10 \text{ cm}^2$  area on the snow block surface. To determine the orientational variability, 10 measurements are performed at one position but for different orientations of the InfraSnow. The measured reflectance values are compared to two reflectance simulations, one for the input parameters obtained from the snow sample with the minimum and maximum CT-measured OED, each.

Figure 4.6 shows all measured values and a comparison to the reflectance simulations by AFE and DISORT. For all snow blocks and both models the simulated reflectance differs clearly from the measured reflectance range.

Both approaches to simulate radiative transfer in snow overestimate measured reflectance by the InfraSnow device. As already explained in Chapter 3.5.3, reflectance calculations by AFE theory are higher than DISORT results at visible and NIR wavelengths and thus deviate even further from the measurements.

For all snow blocks, the measured relative orientational variability from the mean reflectance is less than 4%. The relative spatial variability is larger for all snow blocks with a maximum value of up to 18% found for the fs snow block. This shows that the natural variability of the snow microstructure across a surface area of  $10 \times 10 \text{ cm}^2$  is more significant than possible orientational effects like specular reflections (see Sections 4.3.1 and 4.3.2 for illustrations of specular effects).

Not only do measured and simulated reflectance range not overlap but the size of the range does not agree, either. This can be attributed to the natural heterogeneity of the snow microstructure and the limited number of samples taken inside the InfraSnow sampling volume, which are used as input for the reflectance simulations. Another complicating factor is the contribution of each snow subvolume to the overall reflectance. The closer the snow subvolume is to the InfraSnow opening on the snow surface the stronger the influence of its snow microstructure on the overall measured reflectance. And again, the importance of each snow subvolume varies with the snow microstructure throughout the entire sampling volume.

One property to illustrate this problem in 1D is the penetration depth. This is the snow thickness of one homogeneous snow slab, which extends infinitely to the sides, beyond which a further increase in thickness has no more effect on reflectance. This is a general

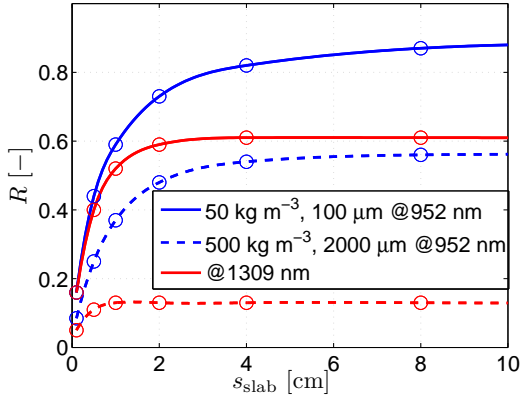


**Figure 4.7:** Reflectance  $R$  vs. snow slab thickness  $s_{\text{slab}}$ . The circles are DISORT simulation results for 2 snow types of differing density and OED at 2 NIR wavelengths. Solid and dashed lines are cubic spline interpolations.

definition and not confined to the InfraSnow geometry. A more banal formulation is: The penetration depth is the depth how far a sensor can see inside the snow cover. This property does not exist for AFE theory, as all effects due to the finite extensions of the simulated snow slab are ignored. If a snow slab is thicker than the penetration depth it is called semi-infinite. In the extreme case of AFE theory only infinite snow slabs, i.e. semi-infinite snow slabs where the light source is additionally placed deep inside the snow slabs, are considered. In general, the penetration depth depends on the snow microstructure (Zhou *et al.*, 2003a) and irradiation wavelength. Figure 4.7 illustrates this for two snow types and NIR wavelengths according to the DISORT model. The shown snow types are extreme in the sense that they are characterized by a very small OED and low density (as may be found for fresh snow) and a high density and very large OED (as may be found for large melt-freeze clusters).

At 1309 nm the reflectance plateau is reached for thinner snow slabs than at 952 nm. Depending on snow density and OED, the penetration depth at 952 nm is about two to four times larger than at 1309 nm.

Snow density and OED increase have opposing effects on the penetration depth. A higher density leads to a shallower penetration depth, as the same amount of scattering and absorption now occurs closer to the irradiated snow surface. In contrast, snow with a bigger OED is characterized by lower scattering and extinction coefficients as well as a higher asymmetry parameter (see Chapters 2.1, 2.2 and 3.5.2 for explanations and visualizations). Thus, radiation is scattered less per snow volume and can penetrate deeper into the snow cover.

Extending the concept of penetration depth to 3D, this means that the sampling volume of reflectance measurements is smaller at longer NIR wavelengths and for higher snow densities and smaller OEDs. Then, of course, each inhomogeneity inside the smaller sampling volume has a greater effect on the obtained reflectance value, too.

The 3D sampling volume in snow is also the primary reason that the InfraSnow measurement results cannot be reproduced by the AFE and DISORT models. Due to the lateral extension of the sampling volume several cm beyond the integrating-sphere opening, a great part of the eventually remitted radiation exits the snow surface beyond the

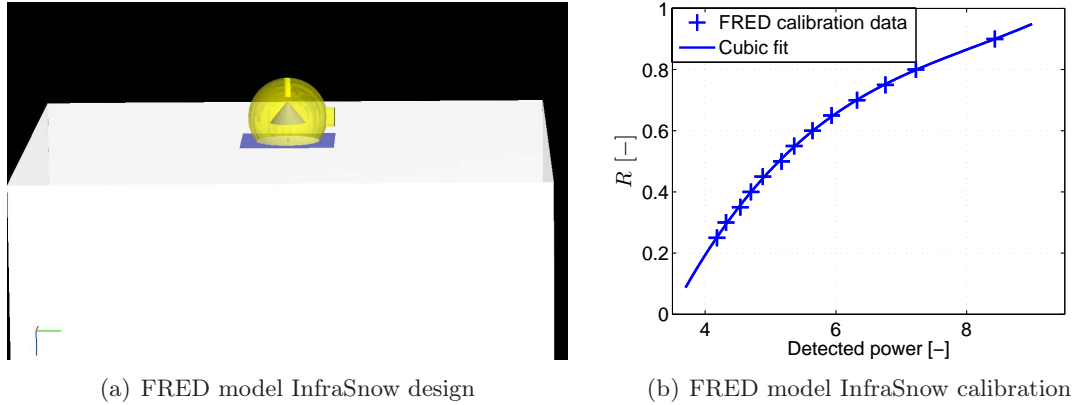


**Figure 4.8:** (a) Visualization of InfraSnow measurement model in FRED, true to scale. Snow block is rendered in white, integrating sphere and detector indentation in gold, diffusing cone baffle in gray, aluminum frame in purple around integrating-sphere opening on the snow surface. The light source is hidden inside the golden notch above the diffusing cone. (b) Calibration of the simulated detected power against 13 reflectance standards with  $R$  between 25 % and 90 %.

opening and is not captured by the InfraSnow detector. Thus, only part of the overall snow reflectance is measured, while this effect can be neglected during the calibration process (Section 4.2) on reflectance standards. As the importance of this radiation loss to the sides depends on snow microstructure, it cannot be quantified by simulations unless the exact geometry of the InfraSnow reflectance measurements on snow is considered. This is not done in AFE and DISORT approach.

### Measurements vs. FRED model

In contrast to DISORT and AFE theory, FRED offers the possibility to specify problem geometry and radiative properties of all participating media (explained in Chapter 3.3.2). In FRED the RTE is solved by Mont-Carlo ray tracing for the implemented problem. The geometry is built by surfaces with a CAD interface. Volumes can be assembled from surfaces. Optical properties are then assigned to these surfaces (e.g. reflective coatings) and volumes (e.g. refractive indices and scattering coefficients). The desired radiation source is built from surfaces and a specified ray distribution on the source surface, where the rays are then launched for the ray-trace analysis.

In this analysis, snow input parameters are Mie-theory single-scattering properties derived for the snow samples in Table 4.1. These are the same values which are also used for the DISORT and AFE models. So, a simplified snow microstructure of OED ice spheres is assumed, a priori. In addition to the snow slab, the optical measurement unit of the InfraSnow (pictured in Figure 4.1) including the aluminum frame around the integrating-sphere opening is drawn by CAD. The visualization of this model designed in FRED is shown in Figure 4.8(a).

An optical coating is assigned to each surface to describe the corresponding reflective

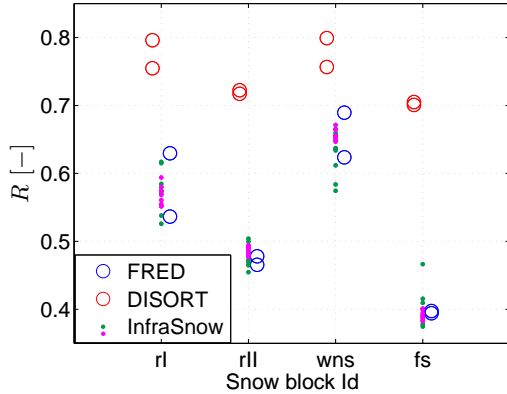


**Figure 4.9:** InfraSnow reflectance measurements, FRED and DISORT results for 4 snow blocks. Corresponding to the notation in Figure 4.6, green dots denote the spatial variability and magenta dots the orientational variability of the measurements.

and absorptive properties of the material. All golden parts have a 96 % diffusely-reflecting coating assigned to them, the white diffusing cone is 80 % diffusely reflecting and the detector surface fully absorbing. The aluminum frame has a specular reflection of 90 %. These are the values given by the manufacturers and found in the literature for the respective materials near the InfraSnow peak wavelength of 950 nm.

In FRED reflectance is modeled exactly as it is measured by the InfraSnow. This includes a calibration with modeled reflectance standards. Here, the modeled InfraSnow unit in Figure 4.8(a) is placed on a surface which is characterized by a coating with the perfectly diffuse reflectance value of the simulated reflectance standard. For reflectance values between 25 % and 90 %, 13 simulations are performed to obtain the calibration curve for simulated diffuse reflectance against detected output power shown in Figure 4.8(b).

Presented FRED model results are not highly sensitive to the optical properties assigned to the InfraSnow coatings. An absolute reduction of 5 % in reflectance for all InfraSnow coatings in the FRED model only leads to a maximum relative change of 3 % in resulting snow reflectance. This is still below the orientational variability of all snow types. Additionally, the changes are not systematic, i.e. a reduction in assigned reflectance coatings does not result in either a decreasing or increasing snow reflectance for all FRED simulations. The minor influence on the results can be understood by examining the simulation principle of the InfraSnow in FRED: a change in the assigned reflectance coatings affects the simulated detected output power substantially for both calibration and snow analysis. However, this results only in a minor change in reflectance as the calibration already accounts for a great part of the modified InfraSnow reflectance coatings.

After the calibration, InfraSnow reflectance is calculated for the same snow density and OED data as for the DISORT and AFE simulations in Figure 4.6. The simulated detected power is then converted to reflectance values according to the calibration curve. Finally, these FRED reflectance values are compared to the InfraSnow measurements. The results are shown in Figure 4.9.

Just looking at the plotted data in Figure 4.9, the FRED model is clearly a more-fitting description for the InfraSnow reflectance measurements of all four snow blocks than the DISORT (and AFE) approach. However, the calculated reflectance range in between the

two model calculations of extreme OED does not correspond with the measured reflectance range.

FRED and DISORT only differ from each other in how they solve the RTE to determine macroscopic optical properties (see introduction to Chapter 3). For FRED this is done by Monte-Carlo ray tracing for the exact problem geometry. DISORT uses the discrete ordinate technique for a plane-parallel layered geometry.

A comparison of simulations with the CTMC ray-tracing model for optical equivalent spheres and with DISORT in Chapter 3.5.3 lead to a relative difference of  $\sim 10\%$  in reflectance between the two models across the entire visible and NIR spectrum for five characteristic snow samples (see results in Table 3.4). Near 950 nm the relative difference is usually even smaller than 5%. Additionally, the reflectance results obtained from the DISORT approach are lower than the values calculated by ray tracing (Figure 3.12). So, the different methodologies to solve the RTE cannot explain the large difference between FRED and DISORT model for the InfraSnow.

Instead, including the exact InfraSnow geometry leads to an overlap and thus to a better agreement between measurements and simulation results for the FRED model. Due to the penetration depth of several cm, and thus a sampling volume extending horizontally beyond the integrating-sphere opening of the InfraSnow, a great part of the radiation which is eventually scattered back out of the snow block is not included in the detected signal. This issue is only addressed by the FRED model. Both DISORT and AFE solution yield an overall spatially unconfined reflectance, thus treating surface-reflecting standard materials and volume-scattering snow for modeling InfraSnow reflectance in the same way. This leads to the strong overestimation of measured reflectance, when the radiation loss to the sides is as substantial as for the compact InfraSnow integrating-sphere design.

The size of the reflectance range is similar for FRED, DISORT and AFE simulations since all of them use the same single-scattering properties as model input parameters. As already stated in this analysis, the different approaches in solving the RTE for the macroscopic optical properties only lead to a difference in reflectance values of up to 10%. Hence, the relative differences for snow types of similar input parameters density and OED are similar.

For the desired OED measurement, the influence of the only other model input parameter snow density has to be determined. If the influence of density on the measured reflectance is large and cannot be measured with a sufficient accuracy the effect of snow OED cannot be isolated. Consequently, snow OED cannot be obtained from InfraSnow reflectance measurements. Reflectance sensitivity to density is illustrated in Figure 4.10 for four different snow OEDs and common densities according to the FRED InfraSnow model.

As expected, modeled InfraSnow reflectance increases with increasing density due to a more compact sampling volume and thus less radiation losses to the sides. While reflectance increases monotonically with density, the trend is not the same for all OEDs. This non-uniform trend can be explained by two contrary effects whose relative importance depends on snow OED and density: (i) With increasing density and decreasing OED scattering increases and thus reflectance (see Chapters 2.1 and 3.5.2). And (ii) increasing density also leads to higher absorption per snow volume and consequently to a lower reflectance.

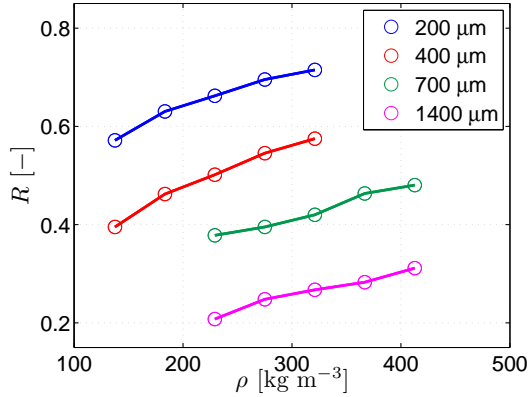


**Figure 4.10:** Reflectance  $R$  vs. snow density  $\rho$  for 4 snow OEDs. Circles denote FRED simulation results in steps of  $\sim 45 \text{ kg m}^{-3}$ , connecting lines are shown for a clearer visualization of the trend.

If snow density is fully neglected and snow OED is used as the only input parameter to analyze InfraSnow reflectance measurements, the resulting variability is much larger than the variability introduced by the natural snow inhomogeneity. For the plotted density range in Figure 4.10 reflectance shows a maximum relative variability of 25% for OED = 200  $\mu\text{m}$  up to 50% for OED = 1400  $\mu\text{m}$ . For an OED measurement method this means that only OED range can be determined within certain reflectance intervals. For natural snow,  $R > 0.7$  measured by the InfraSnow then means that OED  $\lesssim 400 \mu\text{m}$  and  $R < 0.4$  leads to an OED estimate of OED  $\gtrsim 700 \mu\text{m}$ . The range  $0.4 < R < 0.7$  can be measured for a wide range of OEDs, which are not extreme values for fine- or very coarse-grained snow. Unfortunately, within this snow type range differences in OED can already lead to significantly different snow characteristics. Thus, snow density has to be accounted for to obtain a quantitative and useful OED measurement by the InfraSnow.

Currently, snow density can be determined with an accuracy of  $\sim 50 \text{ kg m}^{-3}$  by carefully weighing a predefined snow volume or by electrical conductivity measurements. This corresponds to the resolution of the reflectance simulations plotted in Figure 4.10. The resulting absolute variability in reflectance is between 2% and 6% which translates to a relative reflectance variability of up to 18% for dense snow of OED = 1400  $\mu\text{m}$ . For all other snow types where higher reflectance values are recorded the relative reflectance variability caused by the density uncertainty is generally  $\leq 5\%$ . These values are comparable to the spatial variability caused by the natural snow inhomogeneity of the four snow blocks characterized in Table 4.1 and analyzed in Figure 4.6.

## 4.4 Conclusions and outlook

It has been shown that fast diffuse NIR reflectance measurements by a compact integrating-sphere unit, called InfraSnow, can be explained within the natural snow variability by the FRED model. The only required model input parameters are snow density and OED, derived from the true 3D snow microstructure.

The crucial point in the analysis is accounting for the exact geometry of the InfraSnow reflectance measurements. Due to the large sampling volume compared to the integrating-

sphere opening, radiation losses to the side cannot be neglected. Thus, DISORT and AFE approaches to radiative transfer do not fit the InfraSnow measurements.

In contrast to the results presented in theoretical studies by *Xie et al.* (2006) and *Picard et al.* (2009), no significant effect of grain shape is observed on the reflectance measurements in this thesis. Only a minor effect within the overall natural snow variability is imaginable. However, this possible dependance cannot be resolved in the presented analysis. This agrees with the findings of all previous experimental works on NIR snow reflectance (*Matzl and Schneebeli*, 2006; *Painter et al.*, 2007; *Gallet et al.*, 2009; *Arnaud et al.*, 2011).

Both snow OED and density determine the sampling volume and radiation loss beyond the measurement unit. *Gallet et al.* (2009) also found a significant dependance on both snow OED and density for their reflectance measurements of small sampling volumes under laser-light illumination. To eliminate the impact of density on their measurements, they chose a light source at a longer NIR wavelength to reduce the penetration depth and thus minimize snow-sample boundary effects. This solution to establish a unique correlation between reflectance and OED cannot be realized for the InfraSnow as the entire integrating-sphere opening serves as diffuse illumination source. Hence, light losses beyond the integrating-sphere opening always remain and are especially crucial if a compact design with a small measuring footprint is retained.

The analysis also reveals that the main limitations to the resolution of an eventual snow OED measurement by the InfraSnow are the natural spatial snow inhomogeneity and the currently possible resolution to measure snow density.

The spatial reflectance variability across a surface area of  $10 \times 10 \text{ cm}^2$  is found to be up to 18% due to the natural inhomogeneity of the snow microstructure. Tests on surface-reflecting materials, i.e. materials where no volume scattering occurs, have shown that the InfraSnow is also susceptible to specular highlights, which falsify the measurement interpretation as purely diffuse reflectance. This can explain the orientational variability of the InfraSnow reflectance measurements on snow of up to 4%.

Knowing snow density with an accuracy of  $\sim 50 \text{ kg m}^{-3}$  before performing InfraSnow reflectance measurements, measured reflectance can be predicted by the FRED model within the spatial variability of snow. This demonstrates the possibility to measure snow OED within the natural spatial variability by the InfraSnow once density is determined in advance. Complementing the methods of *Matzl and Schneebeli* (2006); *Painter et al.* (2007); *Gallet et al.* (2009) and *Arnaud et al.* (2011), the InfraSnow permits fast and simple snow-OED measurements in the field across a large snow-covered area by a compact portable device.

For the present InfraSnow design, a higher measurement accuracy can only be achieved if snow density is known more accurately. However, the current measurement accuracy found in this analysis is sufficient for use across large areas in the field, as the natural inhomogeneity of the snow microstructure across a small area of  $10 \times 10 \text{ cm}^2$  already leads to a comparable or even larger reflectance variability. So, an InfraSnow reflectance measurement can be regarded as a representative reflectance value for an area of  $\sim 100 \text{ cm}^2$  within the spatial variability.

To reduce the influence of specular reflections from the snow surface, a baffle could be placed in the direct path between snow surface and detector. While this aims at reducing

the orientational variability, it cannot improve the practical measurement accuracy due to the greater impact of the two main limiting factors snow inhomogeneity and density measurement accuracy.

Replacing the current LED at 950 nm peak wavelength with an LED at a longer NIR wavelength reduces the sampling volume of the InfraSnow. This can lead to a smaller effect caused by the snow inhomogeneity as a more confined snow volume is probed. However, this design change also renders the InfraSnow more sensitive to isolated inhomogeneities (like a stray snow crystal on the snow surface) inside the new smaller sampling volume.

The lack of a unique correlation between measured reflectance and snow OED can also be seen as an additional opportunity: As an extension to the presented reflectance analysis, a simultaneous measurement of snow OED and density is imaginable if 2 LEDs at different wavelengths are used inside the integrating sphere. If the measurement signals at both LED wavelengths offer a sufficient dynamic range to obtain a suitable measurement resolution, both OED and density could then be determined by the InfraSnow in combination with the FRED model.



## 5 Diffuse NIR Transmittance Measurements of Snow

In this chapter transmittance measurements are compared to the AFE, DISORT and CTMC ray-tracing methodologies. CTMC calculations were done by Sophia Haussener at the ETH Zurich. Part of the description and results have been published in: Gergely, M., Schneebeli, M., and Roth, K., 2010: First experiments to determine snow density from diffuse near-infrared transmittance, *Cold Regions Science and Technology* **64**, 81–86.

Some results have also been submitted for publication to the *Journal of Geophysical Research* together with the model results in Chapter 3.5.

Here, a more detailed description of the measurement method and experimental setup is given. Additionally, the effect of a finite snow slab thickness is analyzed for AFE and DISORT model.

Besides OED, snow density is the crucial microstructural parameter which determines radiative transfer in snow. This has already been seen for the model calculations in Chapter 3.5 and for the analysis of InfraSnow reflectance measurements in Chapter 4.

While measuring OED by optical methods has been the focus of many studies, optical density measurements have not been investigated (summary in Chapter 1.2.2). The reason for this lack of interest is that density, in contrast to snow OED, can be determined by other measurement methods, which have been easier to develop for field use. Electrical conductivity measurements on the snow surface or weighing a predefined snow volume, for example, have an accuracy of  $\sim 50 \text{ kg m}^{-3}$ .

Snow hydrologists weigh snow samples along a vertical snow profile to determine overall snow water content in the snow cover and then estimate melt-water runoff in spring. This only requires an overall snow mass and no accurate snow density measurements along the snow profile. Avalanche forecasters often do not measure snow density, at all, as resolution and accuracy of current measurement techniques are too low to permit sound conclusions on the stability of the snow cover.

If many measurements at a high spatial resolution are desired, e.g. along a vertical snow profile wall (Chapter 1.1) to identify small weak spots inside the snow cover, current density measurement techniques prove not very useful as they are time-intensive and only offer a limited resolution of several cm. The density of thin ice or weak layers, which are often crucial for radiative transfer at the snow surface or the snowpack stability deep inside a snow cover, cannot be resolved, for example.

These limitations could be overcome by a density measurement method similar to the method introduced by *Matzl and Schneebeli* (2006) to determine snow OED from NIR

photography (see Chapter 1.2.2 for details). Their method is based on the insignificance of snow density for NIR reflectance of a thick snow-pit wall. Extending their approach to transmittance measurements of an isolated snow-pit wall should yield the required dependence on snow density, if it is assumed that radiative transfer in snow can be modeled with OED and density as the sole model input parameters. This has already been found for reflectance measurements with the InfraSnow in Chapter 4. Ultimately, a combination of both photographic methods could lead to a high-resolution OED image by reflectance photography and a high-resolution density image by transmittance photography.

Translucent snow profiles, i.e. backlit snow slabs of several cm thickness which are penetrated by the incident light, have been used to visualize the inhomogeneity of the snow cover (*Good et al.*, 1991; *Harper and Bradford*, 2003). But, the differences in snow properties have never been quantified by transmittance measurements due to the inability to separate the effects of different snow properties (see Chapter 1.2.2 for details).

Here, the possibility is shown to determine snow density by diffuse NIR transmittance measurements, if snow SSA (and thus OED) is known in advance. Transmittance measurements inside a cold laboratory are compared to transmittance calculations, with model input parameters obtained from the CT-measured snow microstructure. This is the first study to directly correlate measured light transmittance with snow density experimentally, where no empirical fitting parameters or correction factors are introduced.

As for the InfraSnow reflectance measurements, a crucial difference to traditional spectroscopy measurements is that calibration measurements, and thus time and cost for validation, can be reduced to a minimum if the measurements can be described by a physical model. Once transmittance measurements can be explained and the influence of density is understood within the model, an optical method to measure snow density can be developed.

First, the measurement method, based on a home-made integrating sphere as diffuse light source and on a spectrometer as detector, is introduced in Section 5.1. Then, snow transmittance measurements are compared to different radiative transfer approaches in Section 5.2. The radiative transfer models AFE, DISORT and CTMC introduced in Chapter 3 are used for the analysis. The AFE results show that transmittance cannot be modeled if the finite extensions of the probed snow slabs are neglected. DISORT calculations, with only density and SSA needed as input parameters from the snow microstructure, do reproduce transmittance measurement results within the modeled snow variability for most natural snow samples. For highly anisotropic machine-made snow and a more stable analysis, however, the full 3D snow microstructure has to be accounted for. This is shown by a comparison to the CTMC model.

## 5.1 Measurement method and experimental setup

The theoretical background of radiative transfer in snow has been detailed in Chapter 3. AFE, DISORT and CTMC models were introduced and optical properties calculated and compared for five real snow samples. The presented transmittance measurements are analyzed by those three models, based on the knowledge gained from simulations and InfraSnow reflectance measurements in the previous Chapter 4. The respective model

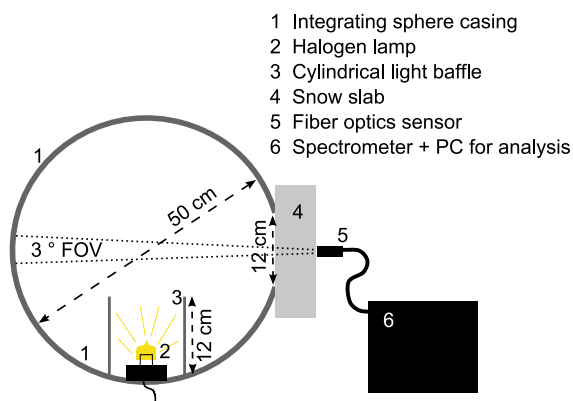


**Figure 5.1:** Sketch of diffuse transmittance measurement principle (not true to scale). Probed snow slab thickness ranges from 2 cm to 8 cm for the presented measurements.

input parameters are determined by micro-CT measurements of snow samples which are taken from the probed snow blocks.

To neglect all influences on radiative transfer caused by snow impurities, snow measurements are performed with NIR illumination (Chapter 1.2.2). Not knowing which wavelengths should be analyzed due to the lack of previous studies, the continuous spectrum of a standard 60 W halogen lamp is used as light source. This also offers the opportunity to analyze transmittance at visible wavelengths to specify the influence of snow impurities.

In order to analyze the measured transmittance spectra at different wavelengths, a high-resolution detector is necessary. For these measurements an ASD FieldSpec<sup>®</sup> VNIR spectrometer is used. It records spectra between 350 and 1050 nm, thus covering the predominantly visible and very NIR halogen lamp spectrum. The spectral resolution is 3 nm with a wavelength accuracy of 1 nm. An optical diffraction grating splits the spectra into their wavelength components and an Si photodiode serves as detector. This setup leads to a usable spectral range from  $\sim 400$  to 1000 nm.

Once again, diffuse illumination is desired to have a simple source of well-defined light available and to avoid a stronger impact on the measurements by localized inhomogeneities for spot-like parallel illumination. Similar to the InfraSnow optical measurement unit (see Chapter 4.1), an integrating sphere is built to diffusely illuminate the snow surface. In stark contrast to the InfraSnow, however, the integrating sphere serves only as diffuse light source and does not double as a crucial part of the integrating-detector design. While a diffusing coating inside the integrating sphere is required to ensure a diffuse incident radiation, a coating with a high diffuse reflectance  $R \approx 1$  is not essential.

The experimental setup is sketched in Figure 5.1. A halogen light bulb is placed inside a home-made integrating sphere. This unit diffusely illuminates an area of 12 cm diameter of a snow slab with a thickness between 2 and 8 cm by multiple-reflected light. Transmittance spectra are recorded with the VNIR spectrometer at  $3^\circ$  field of view (FOV). Measured snow slabs have a cross-section area of about  $20 \times 20 \text{ cm}^2$  perpendicular to the illumination axis.

The sampled snow slabs consist of natural snow collected in the field; only one snow sample is not collected from a natural snow cover but produced artificially in the cold laboratory. Its production process is based on the principles explained in *Nakamura*

(1978). Commonly, machine-made snow consists of small water droplets that have frozen in cold air. Instead, the used snow machine produces snow in cold air oversaturated with water vapor, similar to snow formation in nature (see Chapter 1.1). Snow crystals then form by resublimation on thin threads. This snow is sieved into a styrofoam box, compacted and stored with the other samples at  $-20^{\circ}\text{C}$  until the measurements.

Snow is a delicate and often brittle material to handle. So, positioning the spectrometer sensor accurately inside the snow slabs is very difficult. Additionally, ice crystals can be broken off the snow microstructure and accumulate in front of the sensor housing. This leads to a differing measurement signal due to the localized inhomogeneities inside a very sensitive sampling volume and thus to a faulty analysis. The chosen sensor placement just outside of the probed snow slabs avoids these problems.

The selected spectrometer settings are an integration time of  $\sim 2$  s and a sampling of 20 spectra per measurement output. Although on a much longer time scale than the InfraSnow settings (Chapter 4.1) the sampling average also guarantees a good signal-to-noise ratio  $> 10^3$ . The long integration time per recorded signal ensures a good signal strength, even at longer wavelengths and for snow slabs of several cm thickness.

Snow warming by the halogen light does not have a noticeable effect on the snow structure because of the short exposure time during one measurement of about 1 min. Longer exposure times of several minutes were also tested to assess the heat damage to the original microstructure. Micro-CT images of snow samples, taken from the illuminated snow slabs, show that only a small part next to the integrating-sphere opening is visibly affected by the heat up to a thickness of 1 to 3 mm and only for fine-grained snow samples. For those samples, part of the original snow microstructure melts and refreezes into a coarser microstructure, i.e. snow with a larger OED.

The integrating sphere itself is built of an outer casing of styrofoam with an inner coating of aluminum foil, spray-painted in flat white. The halogen lamp is glued to the bottom of the sphere, and a cylindrical baffle (once again coated by spray-painted aluminum foil) keeps light from exiting the sphere without undergoing any reflections on the walls. This is necessary to avoid non-uniform and non-diffuse illumination of the snow block. The home-made design is not of such a high quality as commercially available integrating spheres. However, it is sufficient to be used as diffuse light source. The lighting unit and the spectrometer sensor are not moved in between measurements. Consequently, the FOV of the spectrometer sensor does not change. Additionally, no measurement errors are observed which could be attributed to the imperfection of the home-made diffusely reflecting coating.

Dimensions of the lighting unit and the snow slabs are chosen with the aim to neglect boundary effects of the finite snow block and to easily detect the measured NIR transmittance signal with the spectrometer. For a big snow block faulty hand measurements and handling, like length measurements with a ruler or a non-perfectly smooth cut surface, introduce a smaller relative error than for a smaller block. With increasing snow block thickness along the illumination axis the detected signal strength weakens rapidly, e.g. according to AFE theory by exponential decay (Equation 3.18). This means a rapidly deteriorating measurement resolution at snow slab thicknesses of more than a few cm. Additionally, a thicker snow block requires greater dimensions perpendicular to the illumination axis and a larger illuminated area to keep the flux approximately diffuse

throughout the entire FOV of the spectrometer sensor.

The spatial resolution of the presented method depends on the snow type that is probed. Fine-grained snow scatters stronger than coarser snow. Denser snow scatters and absorbs more light within the same snow volume than snow with a lower density. These characteristics have already been found in Chapters 2.1 and 3.5.2 and restated for the analysis of InfraSnow reflectance measurements in Chapter 4.3.3.

The presented measurement method does not yield point measurements per se, but one measurement point represents the weighted average of the optical properties of a snow volume. The closer a snow subvolume is to the FOV of the spectrometer sensor the stronger is the influence of its microstructure on the measurement signal. *Beaglehole et al.* (1998) suggest that the diameter of the illuminated area should be about twice the snow slab thickness, when detecting the entire hemispherical diffuse flux exiting the snow block at one point.

To further minimize the impact of the snow block boundaries on the measurements, snow blocks that are larger than the mere illumination area are used, and the optical sensor has a field of view of only  $3^\circ$ . Thus, the deeper the light penetrates the snow the smaller is the cross-section area perpendicular to the illumination axis which determines the detected signal strength.

Finally, the method has to be practical, i.e. snow blocks have to be of such a size that they can be transported from the field to a laboratory and handled comfortably. Considering spatial resolution, signal strength and ensuring a diffuse flux throughout the entire FOV, snow slab thicknesses of 2 to 8 cm are chosen for the experiments.

An overview of the entire measurement setup inside the cold laboratory is shown in Figure 5.2. The integrating sphere (IS) is placed inside a supporting frame to keep it from moving during the measurements. After the snow slab is placed on the snow pedestal in front of the integrating-sphere illuminating opening, the spectrometer sensor can be positioned on the back side of the snow slab by mounting it inside an adjustable guide tube.

Originally, reflectance measurements (with the left sensor mounting on the integrating sphere) were taken simultaneously with transmittance measurements by a second spectrometer sensor. But, reflectance results proved to be too sensitive to the imperfect home-made integrating-sphere setup. They could not even be used for a qualitative analysis. A high-quality integrating sphere at this size, however, is hard to manufacture and very expensive.

For the experiments the halogen lamp is connected to a constant DC power supply. After a warm-up time of about 3 hours in the cold laboratory prior to the snow measurements the whole lighting unit has stabilized. For the next three hours the measurement signal drifts by less than 1.5 % for wavelengths of 450 to 950 nm. Within the actual measurement time for the optical transmittance measurement of one snow slab the signal drifts by less than 0.05 %. This drift can be neglected compared to the uncertainty introduced by the natural snow variability (analyzed in Section 5.2). After the measurement setup has stabilized, snow slabs with a base area of  $20 \times 20 \text{ cm}^2$  and a thicknesses between 2 and 8 cm are sawed and measured.

Transmittance is obtained by 2 separate, consecutive measurements, one with snow sample (snow signal) and one without sample (full signal) between illumination opening

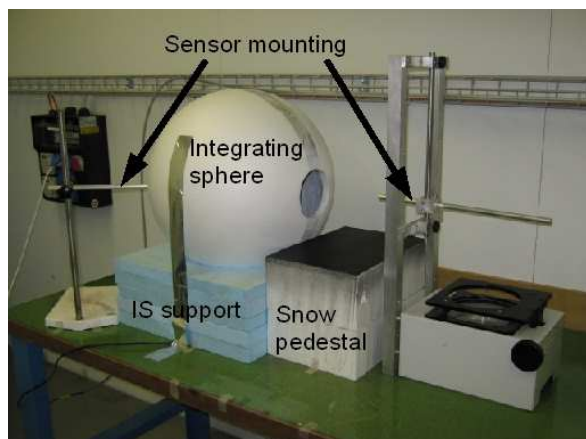


**Figure 5.2:** Image of the setup to measure diffuse transmittance of snow slabs. Snow slabs are placed on the ‘snow pedestal’ between integrating-sphere opening and right sensor mounting for spectrometer sensor (see Figure 5.1 for details on the measurement principle).

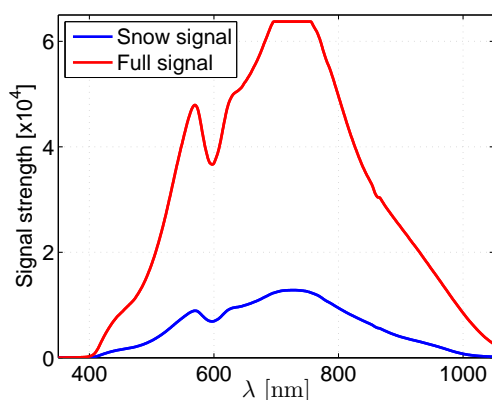


**Figure 5.3:** Raw spectra of transmittance measurement for one snow slab. The full-signal spectrum represents the radiation spectrum of the integrating-sphere light source. Transmittance is specified at each wavelength according to Equation 5.1. Detector is saturated for the full signal between  $\sim 700$  and  $750$  nm.

of the integrating sphere and spectrometer sensor. Including dark current, measured snow transmittance  $Tr$  at each wavelength is given by

$$Tr = \frac{\text{snow signal} - \text{dark current}}{\text{full signal} - \text{dark current}} . \quad (5.1)$$

One example of the two raw spectra is plotted in Figure 5.3. The shown snow signal is obtained by measuring the transmitted light for a  $\sim 3$  cm thick snow slab. Between  $\sim 700$  and  $750$  nm the detector is saturated at a signal strength of  $6.5 \times 10^4$  for the full signal.

After the optical transmittance measurements, two small sample volumes of about  $2 \text{ cm}^3$  are taken from the illuminated volume of each probed snow slab and stored in the freezer at  $-20^\circ\text{C}$ . During the week following the transmittance measurements all samples are analyzed by micro-CT to determine SSA and density. Three subvolumes of each snow sample are scanned. To estimate the effect of storage time, SSA decrease is calculated for isothermal conditions in between transmittance and micro-CT measurements. According to table 4 and equation 16 in *Flanner and Zender (2006)* SSA changes by less than 0.5% for most tested snow samples. Only SSA of snow that is stored for 20 days or less

prior to the transmittance measurements decreases by about 2.5% according to *Flanner and Zender* (2006), which is less than the natural snow variability. For similar snow, experiments by *Kaempfer and Schneebeli* (2007) show an SSA decrease of less than 1%. These small changes in SSA due to snow metamorphism are neglected in this study, as the natural SSA variability of the snow slabs has a much larger effect on transmittance results (see Section 5.2).

The resolution of micro-CT snow measurements is high enough to determine SSA (and thus OED) with an accuracy of 3% within the values measured by the reference method of methane adsorption (see Chapter 1.2.1 for details on micro-CT). The resolution of the micro-CT used in this study is high enough that the SSA can be measured up to about  $100 \text{ mm}^{-1}$  with this accuracy. *Legagneux et al.* (2002) state an overall accuracy of 12% for SSA measurements with their methane adsorption method.

The micro-CT data are used as input for transmittance model calculations. These are compared to the measured transmittance values at two wavelengths in the NIR. 830 nm and 927 nm are selected for the following reasons: Measured and calculated transmittance do not exhibit a high sensitivity to wavelength in the vicinity of these two wavelengths. Moreover, it is possible to use explicitly-calculated single-scattering properties at these two specific wavelengths from *Warren and Brandt* (2008). The resolution of their calculations in the NIR is about 20 nm. Finally, at shorter wavelengths soot has a stronger effect on radiative transfer in snow, and at longer wavelengths the signal strength weakens drastically, especially for a snow block thickness of more than a few cm.

## 5.2 Measurement results and analysis

Overall, transmittance is measured for 6 snow types and 8 different sampled snow slabs by this setup. Snow-sample characteristics are listed in Table 5.1. Six CT-scans are performed for each snow-slab Id to determine SSA and density, following the transmittance measurements. For the 8 cm thick lmf snow block a slice of 2 cm is cut from the block at the side facing the spectrometer sensor after the first optical measurement. The remaining snow block is once again measured in the same position as before. This procedure is repeated until the snow block has been cut completely. The resulting snow slab thicknesses are 8, 6, 4 and 2.5 cm. All other snow samples are measured with only one snow block thickness.

Often, SSA is also presented in  $\text{m}^2 \text{ kg}^{-1}$  in the literature. The conversion factor for the numerical values from  $\text{mm}^{-1}$  to  $\text{m}^2 \text{ kg}^{-1}$  is  $\frac{1000}{\rho_{\text{ice}}} \approx 1.1$ , with the numerical value of ice density  $\rho_{\text{ice}}$  given in  $\text{kg m}^{-3}$ .

### 5.2.1 Measurements vs. DISORT and AFE models

Modeled transmittance values are calculated for the micro-CT snow samples with an OED corresponding to the extreme SSA values in Table 5.1 (OED is obtained by Equation 1.1). For lmf snow only one CT-sample per probed snow slab is available. Additionally, density varies more between the four different sections of the snow slab than what is expected for homogeneous natural snow. To reproduce a realistic density range within each lmf snow

**Table 5.1:** Overview of measured snow slabs. Snow-type nomenclature according to *Fierz et al.* (2009): MF is short for melt forms, RG for rounded grains, MM for machine-made snow, DF for decomposing and fragmented precipitation particles, DH for depth hoar and FC for faceted crystals. SSA and density ranges are minimum and maximum micro-CT measurements for each snow slab. Numerical values of SSA in  $\text{m}^2 \text{kg}^{-1}$  are about 10% higher. For lmf snow 4 thicknesses are measured. Otherwise, thickness range is the minimum and maximum measured snow-slab thickness of the probed snow slabs.

Id	Snow type	SSA [ $\text{mm}^{-1}$ ]	Density [ $\text{kg m}^{-3}$ ]	Thickness [cm]
lmf	large MF	3.4 – 3.9	440 – 600	8, 6, 4, 2.5
mf	small MF	11.1 – 15.9	449 – 559	4.0 – 5.0
rg	small RG	13.6 – 15.6	312 – 376	4.7 – 5.0
mm	fine-grained MM	22.3 – 26.0	275 – 303	4.5 – 5.0
def	DF	37.8 – 39.8	92 – 110	2.0 – 3.0
defII	DF	34.1 – 36.0	128 – 147	2.5 – 3.5
deh	DH	8.1 – 8.4	339 – 376	2.5 – 3.5
rf	small RG and FC	17.1 – 18.0	220 – 303	2.5 – 3.0

slab, a relative variability of 15% is assumed as input for the transmittance simulations of each snow slab.

Transmittance measurement results for lmf snow are compared to calculations by both AFE theory (explained in Chapter 3.4) and the DISORT model (see Chapter 3.2) in Figure 5.4. The plots show a better agreement between DISORT calculations and measurements.

In Figure 5.4(a) the measured and the lowest calculated transmittance values differ by a factor of 2 to 5. If a snow depth of 2.5 cm (the thinnest measured snow slab) is taken as reference value for the transmittance measurements (i.e. a transmittance of 1 at a snow depth of 2.5 cm) the agreement between measured transmittance and calculated values by Equations 3.17 and 3.18 improves slightly. However, the placement of the spectrometer sensor at the snow surface and not well inside a thick snow slab (Figure 5.1) means that all light reaching the back of the snow slab is lost. This is analogous to putting a black panel (reflectance of 0) behind the probed snow slab. This clearly causes a weaker measurement signal than for the conditions to which Equation 3.17 strictly applies: placing the sensor deep inside a snow cover, as it is demonstrated by *Warren et al.* (2006). In this case, part of the light reaching the depth of the sensor is scattered backwards and, by another scattering event into the opposite direction, can then enhance the measured signal, compared to the presented experimental setup.

In Figure 5.4(b) DISORT calculations with the same model input parameters fit the corresponding measurement results a lot better. The results imply that the discrepancies between measurements and calculations by Equation 3.18 cannot be explained by inaccurate model parameters. For this experimental setup boundary effects at the front and back side of the snow slab are simply too significant to be neglected. Thus, AFE theory cannot be used to explain the shown measurement data and to determine snow density from transmittance measurements.

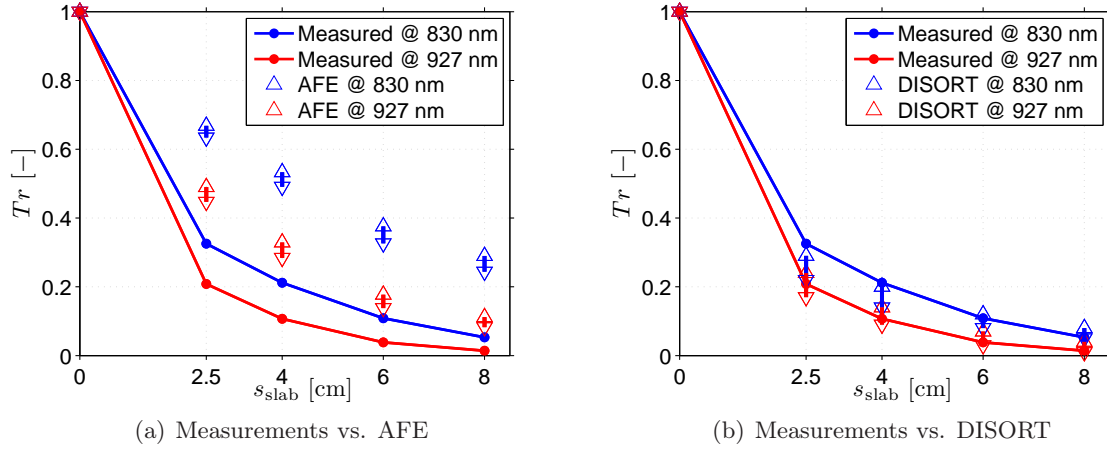


**Figure 5.4:** Transmittance  $T_r$  measurements of all lmf snow slabs of thickness  $s_{\text{slab}}$  (see Table 5.1) compared to AFE and DISORT models. Plotted  $T_r$  range for AFE calculations is the range resulting from CT-measured input parameters SSA and density to minimum calculated  $T_r$  for density and SSA variability. DISORT  $T_r$  results cover the complete range from maximum to minimum calculated  $T_r$  for density and SSA variability.

The boundary effect of finite snow slab thickness is shown explicitly in Figure 5.5. The DISORT results approach the AFE values with the same input parameters if transmittance is calculated at depth  $s_{\text{slab}}$  inside a semi-infinite snow slab instead of an overall snow slab thickness  $s_{\text{slab}}$ . This effect is stronger at 830 nm as at shorter wavelengths the penetration depth and thus the influence of the microstructure at greater snow depths is larger (explained for reflectance in analysis of Figure 4.7). The semi-infinite geometry nullifies the boundary effect of the finite snow slab extension at the sensor side. However, the remaining effect of the light-source placement outside of the snow slab, i.e. a non-infinite snow slab, is still seen in the differing transmittance values for AFE and semi-infinite DISORT simulations in Figure 5.5.

Due to this effect AFE theory overestimates transmittance of all other probed snow slabs, too, and the optical transmittance measurements of the remaining 7 snow samples are only compared to DISORT simulations in Table 5.2. Except for mm snow, measured values lie within the calculated transmittance range for the extreme cases of SSA, density and snow-slab thickness.

The poor agreement for mm snow is caused by the peculiar snow structure. This snow contains a lot of plate-like features of several mm in size. In addition to the highly anisotropic shape of these plates, micro-CT images show that they are also arranged in a parallel layering, which can be attributed to the sample preparation by sieving (see Figure 5.6(c)). The resulting snow microstructure is then too different from a collection of spheres to be treated as such in transmittance calculations. Here, using a ray-tracing code could be promising, where the true 3D snow microstructure is used as model input, instead of just the two macroscopic parameters SSA and density for DISORT. This possibility is explored by the CTMC model in the next Section 5.2.2.

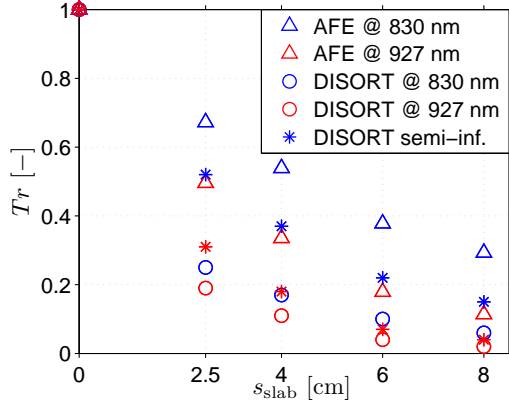


**Figure 5.5:** Boundary effect of finite snow slab thickness on transmittance  $Tr$ , calculated by AFE and DISORT for lmf snow slabs of thickness  $s_{\text{slab}}$ . Asterisks denote DISORT results for  $Tr$  inside a semi-infinite snow slab at snow depth  $s_{\text{slab}}$ .

**Table 5.2:** Comparison of transmittance measurements with DISORT calculations for mf to rf snow specified in Table 5.1.

Id	Transmittance [%]			
	@ 830 nm		@ 927 nm	
	Measured	DISORT	Measured	DISORT
mf	2.8	1.8 – 7.8	0.7	0.5 – 4.3
rg	3.6	3.6 – 6.5	1.1	1.3 – 3.8
mm	2.3	3.4 – 5.3	0.6	1.3 – 3.1
def	19.4	14.4 – 23.5	15.3	12.6 – 22.3
deffI	13.1	9.4 – 14.8	8.9	7.1 – 13.0
deh	20.1	14.0 – 21.7	12.8	9.9 – 18.2
rf	16.8	10.4 – 17.4	11.3	7.5 – 15

Additionally, Table 5.2 shows no significant difference between the agreement at 830 and 927 nm. All transmittance measurements and simulations show the same trend at both wavelengths. Nevertheless, the relative variability of the calculated transmittance at 927 nm is  $\sim 30\%$  larger than at 830 nm for all snow slabs. At 830 nm variability from the mean transmittance ranges from 21% for deh snow to 62% for mf snow and at 927 nm from 29% (deh) to 79% (mf). A general trend can be stated: the lower the transmittance the larger the relative variability.

These relative variability values are a lot higher than the reflectance variability for four snow slabs analyzed in Chapter 4.3.3. There, a maximum relative variability of 18% from the mean is found while measurements and simulations of some snow types only yield a variability  $< 10\%$ . To achieve a more confined theoretical transmittance range in this analysis, it should be possible to cut the snow slabs to a more even thickness, as the thickness variability introduces a major uncertainty for the probed snow slabs.

Finally, an analysis at different wavelengths could yield drastically different quantitative but also qualitative results. In the visible part of the light spectrum soot can have a major impact on the optical properties. At longer NIR wavelengths, where light penetration

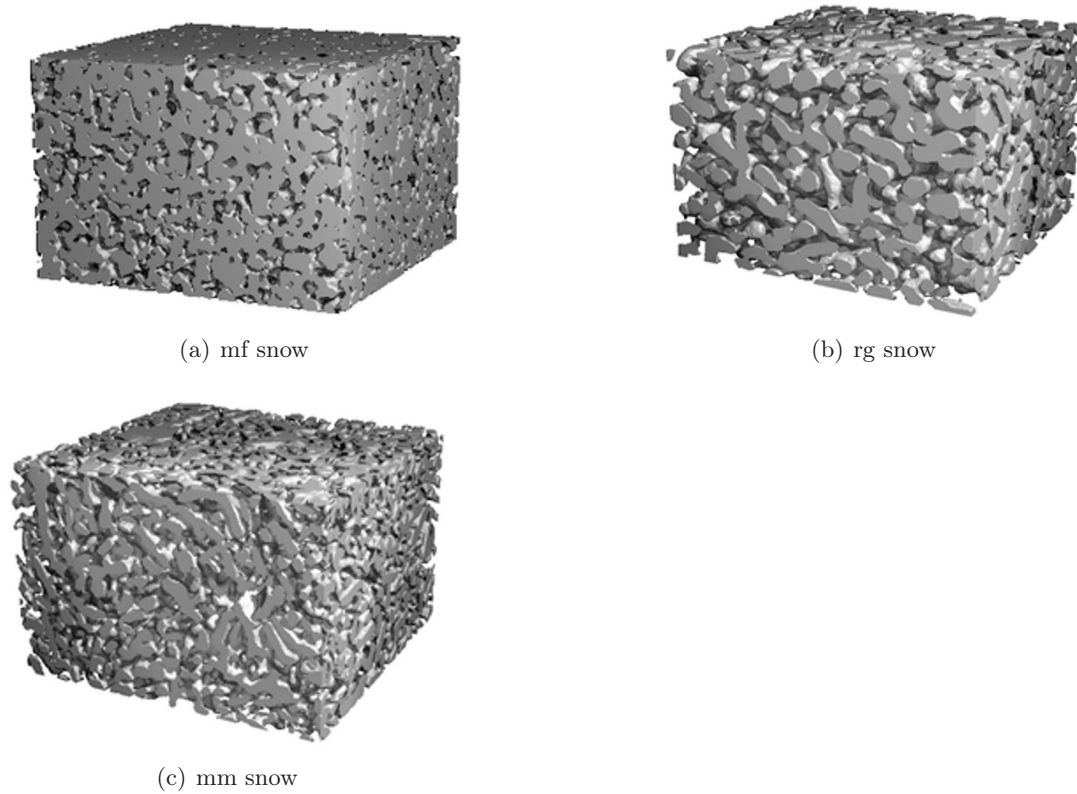


**Figure 5.6:** Snow microstructure for 3 snow samples scanned by micro-CT and used for transmittance measurements and simulations. Pictured sample size is  $6 \times 6 \times 4 \text{ mm}^3$ . Voxel size for the micro-CT scans is  $10^3 \mu\text{m}^3$ .

depth is reduced to a few mm, very localized irregularities at the snow surface can alter the transmittance signal disproportionately to their volume fraction of the entire probed snow volume.

### 5.2.2 Measurements vs. CTMC model

For three of the snow slabs which are characterized in Table 5.1 transmittance at the two NIR wavelengths is additionally analyzed by the CTMC ray-tracing model, which was introduced in Chapter 3.3.1. The slabs are indicated as mf, rg and mm snow. Their true 3D microstructure, needed as input to the CTMC particle- and pore-level optical simulations, is shown in Figure 5.6.

Transmittance measurements and calculation results by the CTMC and DISORT models are presented in Figure 5.7. The calculated transmittance range accounts for the microstructural variability between the six micro-CT subsamples and the uncertainty in slab thickness listed in Table 5.1.

Figure 5.7 indicates a better agreement between measurement and CTMC calculations at both NIR wavelengths for rg and mm snow. Only for mf snow transmittance measure-

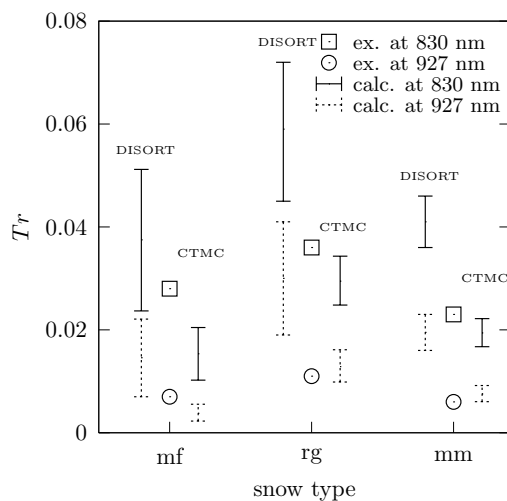


**Figure 5.7:** Comparison of transmittance calculated by DISORT (left bars), experimentally measured (middle markers) and calculated by CTMC (right bars) for 3 investigated snow slabs, which are characterized in Table 5.1. Solid bars are calculations at 830 nm, dotted bars at 927 nm. Squares and circles indicate measurements at 830 nm and 927 nm, respectively.

ments lie within the calculated transmittance range by DISORT. As found in the analysis in Table 5.2, the biggest disagreement between measurements and the DISORT-calculated transmittance range are observed for mm snow, which contains many thin ice plates with a preferentially horizontal orientation. Here, the DISORT approach to consider snow as a collection of independently-scattering OED spheres is too far removed from the original highly-anisotropic snow microstructure. In contrast to DISORT, the CTMC model uses the true 3D microstructure of the snow sample as input and thus shows a better agreement with the measurements.

For both other slabs of mf and rg snow, transmittance measurements, DISORT and CTMC calculations deviate less from each other. For these more isotropic and non-layered snow types the effect introduced by the deviation of the real snow microstructure from an equivalent microstructure of OED ice spheres is not as pronounced.

The presented analysis also confirms the findings from Chapter 3.5.3: Transmittance values calculated by DISORT are higher than the values obtained from CTMC simulations and measurements.

Furthermore, the variability of the input parameters appears to have a stronger effect on DISORT calculations, as here the resulting transmittance range for each snow slab and at both wavelengths is larger than for CTMC simulations.

### 5.3 Conclusions

Diffuse transmittance measurements and calculations have been compared at 830 nm and 927 nm for 8 snow slabs, cut from snow blocks consisting of melt forms, decomposed, rounded, faceted and machine-made snow. The experimental setup consists of a home-made integrating sphere as diffuse light source and a spectrometer as detector. After the optical transmittance measurements snow samples are taken from the probed snow slabs. The snow microstructure is then determined from these samples by micro-CT and used as model input to calculate transmittance of the measured snow slabs by AFE, DISORT

and CTMC models.

The results show that transmittance measurements and simulations for most analyzed natural snow types agree within SSA, density and thickness variability calculated by DISORT. This confirms previous experimental results of optical snow measurements, e.g. by *Warren et al.* (2006); *Matzl and Schneebeli* (2006); *Painter et al.* (2007); *Gallet et al.* (2009) and *Arnaud et al.* (2011). They have not found other parameters like grain shape to have a significant effect on their analyses, either.

The simpler AFE approach cannot reproduce the measurement results, as it strictly applies only to the limit of an infinite snow block with internal light source and detector placement. These conditions are sufficiently met in *Warren et al.* (2006), where AFE theory is applied successfully to the analysis of transmittance measurements. In contrast to their work, measured transmittance is clearly overestimated by the AFE model for the presented measurement design.

The comparison of CTMC and DISORT calculations with transmittance measurements for 3 snow slabs (melt forms, rounded and machine-made snow) shows a better agreement between measurements and CTMC model. DISORT calculations overestimate snow transmittance. This is especially true for the machine-made snow sample, which contains many large plates of several mm in length with a predominantly horizontal orientation. With the true 3D snow microstructure as its model input, CTMC can reproduce the measurements better than the DISORT approach, which is based on an equivalent snow microstructure of OED ice spheres. The extreme case of anisotropic grain shape and non-random orientation for machine-made snow shows the limit of modeling the true 3D snow microstructure as OED ice spheres in DISORT. This finding forms an experimental equivalent to *Xie et al.* (2006) and *Picard et al.* (2009), who found a major influence of grain shape on their optical simulations for collections of randomly-oriented spherical and angular grains (like cubes or prisms).

Additionally, the CTMC model is a more stable approach to analyze the presented transmittance measurements. The variability of the snow microstructure, obtained from 6 CT-samples per probed snow slab, leads to a smaller variability than for the DISORT calculations.

To facilitate the use of the presented analysis, SSA could be determined independently by simpler methods than micro-CT (see Chapter 1.2.2). While even without the need for micro-CT measurements this represents a rather laborious method to determine snow density, the analysis shows that snow density can be measured optically for natural snow within the range of natural snow variability. This could permit the development of a faster and more simple-to-use optical method to measure density in combination with SSA in the field. An outlook to such a method by a quantitative analysis of high-resolution translucent snow profiles is given in Chapter 6.



# 6 Outlook: Reflectance and Translucent Snow-Profile Photography

The presented measurements have been performed by M. Schneebeli in Antarctica in January 2011 and are analyzed with his help.

It has been shown in Chapter 5 that transmittance measurements of most investigated snow types can be explained within the natural microstructural variability calculated by the DISORT model. A detailed description of the DISORT approach to radiative transfer is found in Chapter 3.2. Only snow OED (and thus SSA by Equation 1.1) and density are needed as model input parameters. This should permit the development of a measurement method to determine snow density in the field, once OED and transmittance are known.

Here, first tests of a combined measurement method are presented to measure snow OED and density by high-resolution snow-profile photography in the field. The measurement principles and setup are introduced in Section 6.1. Then, results of a combined OED and density measurement for one snow profile in Antarctica are shown in Section 6.2.

## 6.1 Measurement method and experimental setup

The proposed measurement method involves two separate measurements of the same snow profile (see Figure 1.2 for an example of a typical snow profile). First, a reflectance image is taken of the full snow-pit wall to determine snow OED across the snow profile. Then, a slab of several cm thickness has to be isolated from the previously photographed snow-pit wall, and a transmittance image is taken of the backlit isolated snow slab. With the corresponding OED profile obtained from the reflectance image and the transmittance image available for analysis, snow density can be determined across the photographed snow profile. The two steps are explained in more detail in the following sections.

### 6.1.1 Snow OED measurement by NIR reflectance photography

Snow OED measurements roughly follow the method introduced by *Matzl and Schneebeli* (2006). Their experimental setup is shown in Figure 6.1. A picture of a snow profile is taken and snow reflectance is calibrated against reflectance standards, which are placed in the corners of the snow profile. The method is based on the unique correlation between NIR reflectance and snow SSA for snow blocks of a sufficient thickness (see penetration depth analysis and semi-infinite snow thickness in Figure 4.7). Exchanging the standard NIR-blocking filter against a visible-light blocking filter, only NIR light is detected. Thus, a spectrum from  $\sim 840$  to 940 nm is recorded by their camera CCD image sensor.

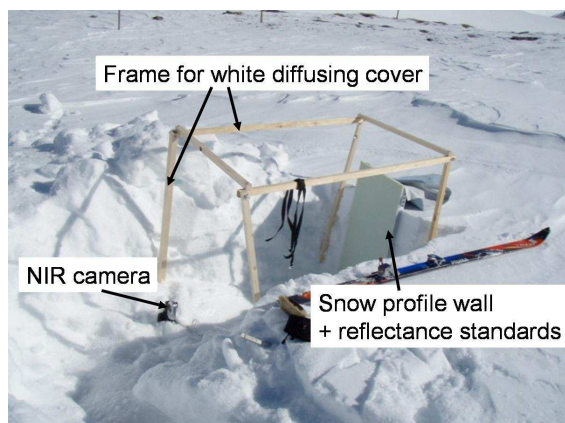


**Figure 6.1:** Setup for pure NIR reflectance photography in the field. In this picture the snow-profile frame and reflectance standards are covered by a grey foam mat. For measurements under direct sunlight a white diffusing cover is put over the frame to guarantee diffuse illumination.

Diffuse lighting under a clouded sky or created from direct sunlight by putting a white diffusing cover over the snow pit is crucial for the interpretation of the measurement results. SSA is then derived from the diffuse reflectance image by a correlation curve, which was obtained by comparing reflectance with stereological SSA measurements for 29 snow samples. Hence, this correlation strictly applies only to their own used camera. They state a spatial resolution of  $\sim 1$  mm and a measurement uncertainty of 15 % for the measured SSA. By Equation 1.1 this also translates to an uncertainty of 15 % for OED measurements. Suggested modifications to the setup should further improve the OED measurement accuracy. E.g. a reference picture of an optically-homogeneous target, which covers the entire snow profile, can identify all effects which are introduced by an inhomogeneous illumination of the snow profile.

Here, calibration measurements are minimized. Instead of a correlation between measured reflectance and SSA or OED by many calibration measurements, establishing a correlation by a physical radiative transfer model is desired. This approach demands either a well-defined light source or a detector with a high spectral resolution for accurate measurements and modeling. Keeping the high spatial resolution and easy operation offered by a digital camera, an ExoLight™ LED linear light is chosen to replace the broad illumination spectrum of sunlight. This tube-style LED light emits isotropic (diffuse) light with a peak wavelength of 940 nm. In Figure 6.2 the correlation between reflectance and OED at this wavelength is calculated by DISORT.

Additionally, the whole setup in Figure 6.1 is modified to also permit a subsequent translucent photograph of the same snow profile. A sketch of the modified setup to measure both reflectance and transmittance is shown in Figure 6.4. Compared to Figure 6.1 (i) the frame is built more sturdily and (ii) the construction allows digging a second snow pit to isolate the snow profile and analyze transmittance by backlighting. For the reflectance image, however, the original snow cover beyond the photographed snow profile is still undisturbed. This is necessary to guarantee probing a semi-infinite snow block and to permit an analysis based on the unique correlation between snow OED and reflectance.

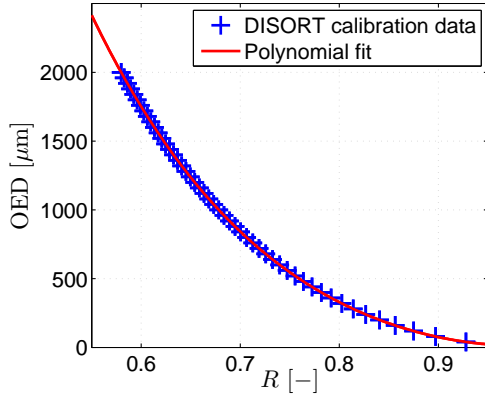


**Figure 6.2:** Snow OED vs. Reflectance  $R$  according to DISORT for diffuse illumination at 940 nm. The correlation is used to obtain OED from snow-profile reflectance images.

### 6.1.2 Snow density measurement by translucent snow-profile photography

Transmittance is measured by taking an image of a backlit snow wall. Such translucent snow profiles have been used to visualize the spatial inhomogeneity of a snow cover, but they have not been analyzed to derive quantitative microstructural parameters (e.g. in *Good et al.*, 1991; *Harper and Bradford*, 2003).

In contrast to these translucent profiles under visible illumination, translucent profiles should be analyzed at NIR wavelengths to neglect snow impurities (see Chapter 1.2.2). However, it is found that the agreement between transmittance measurements and DISORT calculations for 7 snow slabs in the previous Chapter 5.2 does not change significantly or systematically when the same measurements are analyzed at visible wavelengths. The results at 520 nm (greenish light) are included in Figure 6.3 together with the original results at two NIR wavelengths. The only snow type where the calculated transmittance variability clearly does not contain the measured values is mm snow. This is true for all three analyzed wavelengths. If snow impurities, i.e. mainly highly-absorbing soot for the probed snow samples, had an effect on the results at 520 nm it would have been expected that the DISORT calculations overestimate measured transmittance. For clean snow, as it is found in Antarctica, the influence of snow impurities can even be neglected, a priori, for wavelengths  $\lambda \gtrsim 500$  nm (*Warren et al.*, 2006).

Figure 6.3 also illustrates the advantage of analyzing snow-slab transmittance at visible wavelengths: Especially for the thicker mf, rg and mm snow slabs (4–5 cm thick) the transmittance and thus the detected signal is stronger by a factor  $> 2$  than at NIR wavelengths. Additionally, a thicker snow slab is (i) easier to isolate from the snow cover and (ii) offers a higher resolution for the analysis. Cutting or sawing the snow slab leads to an uncertainty in thickness of few mm, which translates to a smaller relative variability and thus a higher measurement resolution for a thicker snow slab.

As for the NIR light source, an ExoLight™ LED linear light, but with a peak wavelength of 530 nm, is chosen to illuminate the translucent snow profile because of its strong and isotropic light emission. Additionally, the camera which is used as light detector is most sensitive to green light across the visible spectrum.

Reflectance and translucent snow-profile images are taken by a professional-grade Nikon

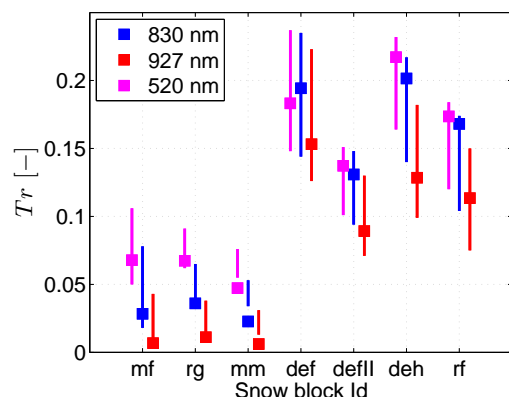


**Figure 6.3:** Transmittance  $T_r$  for 7 snow slabs at 3 wavelengths. Squares denote measurements, bars indicate the transmittance variability calculated by DISORT according to snow SSA, density and thickness variability data given in Table 5.1.

D3S digital SLR camera. This camera can record RAW-format images by a full-frame 12 megapixel CMOS image sensor. RAW images feature a higher dynamic range (14 bit uncompressed for the Nikon 3DS) than common lossy JPEG compression (8 bit compressed images). Compared to other professional-grade digital cameras capable of taking RAW pictures, the Nikon 3DS additionally offers an even wider dynamic range and better signal-to-noise ratio due to its sensor design. This is especially true for low-light conditions, where a high camera sensitivity is required. These characteristics make the selected camera a reasonable choice to test the presented translucent snow-profile photography, where slight changes in an overall low-intensity signal have to be analyzed.

The entire experimental setup for the presented method of combined reflectance and translucent snow-profile photography is illustrated in Figure 6.4. Initially, only PIT 1 is dug for the snow-profile reflectance photo and both NIR lights are turned on. As for the method presented by *Matzl and Schneebeli* (2006), a visible-light blocking filter is attached to the camera lens to prevent ambient visible light from influencing the recorded NIR signal. Ambient visible light can enter the snow pit through the surrounding snow cover due to the large penetration depth at shorter wavelengths (see Figure 4.7). A 5.8 cm thick snow-profile wall is then isolated carefully by digging PIT 2. A smooth snow wall should be obtained without cracks or collapsed regions. The green light is installed and the NIR lights are turned off. Before taking the translucent snow-profile image the visible-light blocking filter is detached from the camera.

As suggested by *Matzl and Schneebeli* (2006), an image of a homogeneous material, which covers the entire snow profile, is taken in addition to the procedure described in Section 6.1.1 to account for inhomogeneous lighting of the snow profile. Here, a foam mat is chosen. The raw snow-profile reflectance image, including the reflectance standards on the frame, is then scaled by the foam-mat photograph. Now, the homogenized reflectance image can be created by comparing each pixel intensity with the intensity of the reflectance standards. Finally, snow OED is derived for each pixel from the correlation curve plotted in Figure 6.2.

To determine transmittance across the snow profile two images are taken as well. But in contrast to NIR reflectance photography, no diffuse transmittance standards are available.

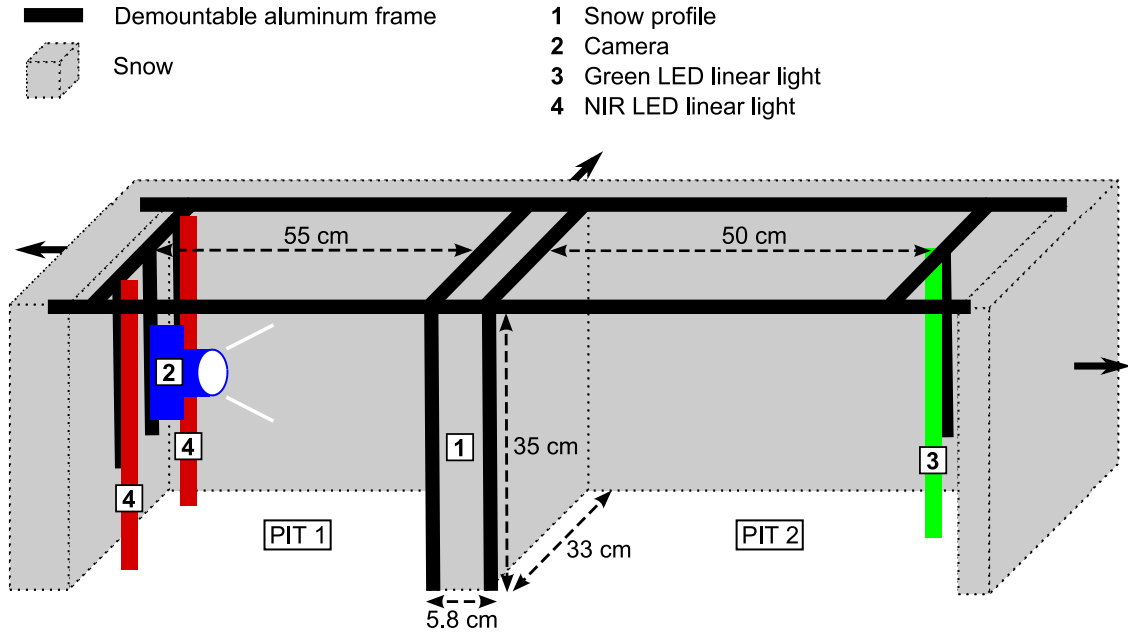


**Figure 6.4:** Sketch of measurement principle for combined reflectance and translucent snow-profile photography (slant side view, not true to scale). Arrows indicate extension of the natural snow cover beyond the drawn region. Not shown are the snow cover on the viewer’s side and possibly below the setup, the cover sheet on top of the aluminum frame and a small opening in the snow cover to the left of PIT 1 to operate the camera. First, a reflectance image is taken under NIR lighting of the snow profile in PIT 1 only. Then, PIT 2 is dug out to isolate the snow-profile wall, the green LED light is installed and the translucent snow profile is photographed.

This requires that the reference photo of a homogeneous material serves both to homogenize the raw translucent snow-profile image and as transmittance calibration. Here, a sheet of white plastic is used as reference material. Overall transmittance of the plastic is determined as  $Tr = 0.06$ . The calibration is achieved by comparing detected light intensity with and without plastic sheet for the presented setup in Figure 6.4.

For each pixel in the snow-profile photograph snow density is obtained from a look-up table, which has been calculated in advance. The table lists density values for the natural range of snow OED and transmittance data according to the DISORT model. For the presented measurement method and common natural-snow densities and OEDs the expected correlation is shown in Figure 6.5.

According to the DISORT results in Figure 6.5(a) low transmittance measurements  $Tr \lesssim 0.05$  are only expected for  $OED < 600 \mu\text{m}$  independent of snow density. Correspondingly, high transmittance values are only possible for large snow OEDs. Intermediate transmittance values around  $Tr \approx 0.2$ , however, cover a great range of snow density and OED. Thus, a high measurement accuracy of snow OED is especially crucial for fine-grained snow with low OEDs in order to accurately determine snow density.

Figure 6.5(b) illustrates the dynamic range of the presented density measurement

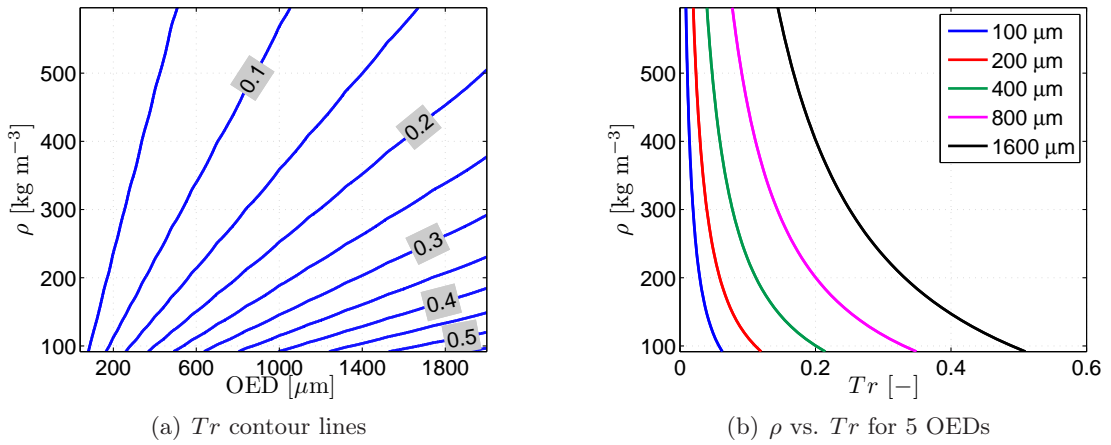


**Figure 6.5:** Correlation between snow density  $\rho$ , OED and transmittance  $Tr$  according to DIS-ORT for translucent snow-profile photography illustrated in Figure 6.4. Here,  $Tr$  is calculated at a resolution of  $\Delta\rho \approx 10 \text{ kg m}^{-3}$  and  $\Delta\text{OED} = 20 \mu\text{m}$ .

method. For snow types with large OEDs the dynamic range is wider than for snow types with smaller OEDs. For  $\text{OED} = 100 \mu\text{m}$  the transmittance range covering all densities is  $\Delta Tr = 0.05$ , while for  $\text{OED} = 1600 \mu\text{m}$  the dynamic range is  $\Delta Tr = 0.37$ . This is only true for the absolute dynamic range. Instead comparing relative transmittance variability for the five snow types, the largest relative dynamic range from the mean transmittance is found for  $\text{OED} = 100 \mu\text{m}$ . Here, the relative transmittance variability across the entire density range is  $\sim 1.4$  times the variability for  $\text{OED} = 1600 \mu\text{m}$ . In contrast to absolute dynamic range, relative transmittance variability decreases with increasing OED.

Additionally, Figure 6.5(b) reveals the importance to accurately measure low transmittance values independent of OED. The flatter the plotted correlation curve the higher is the resolution to derive snow density from transmittance. For all OEDs this indicates an increasing density measurement resolution as measured transmittance increases.

## 6.2 Results and analysis of one Antarctic snow profile

Here, reflectance and translucent snow-profile photography is tested for one snow profile in Antarctica. First results of the OED and density analysis in Section 6.1 are presented.

Figure 6.6 shows normalized reflected and transmitted light intensities, obtained from both snow-profile photographs and the two corresponding normalization images of a foam mat (in reflectance setting) and a white plastic sheet (in transmittance). For both images the same microstructural inhomogeneities within the snow cover can be recognized. However, relative intensity differences between corresponding snow-profile regions are higher in the translucent snow-profile photograph.

The pictured snow profile is typical of Antarctic snow covers: near the surface, different wind-deposited snow types can be found (identifiable by bluish colors); deeper down, the snow cover is characterized by thicker and more homogeneous layers of depth hoar. Gen-

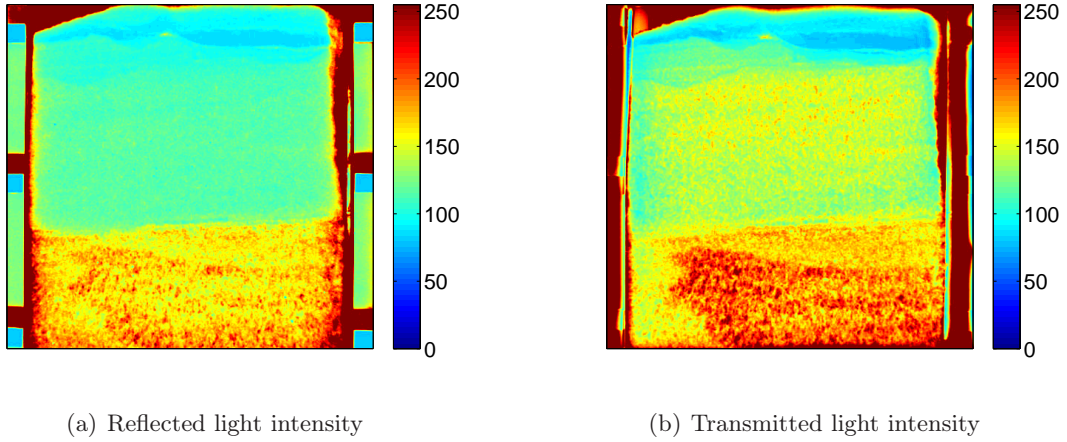


**Figure 6.6:** Normalized snow-profile images of NIR reflected and green-light transmitted intensities. Snow-profile height is 35 cm. The photographs are obtained with the setup shown in Figure 6.4. Plotted intensities are scaled linearly from 0 to 255 as indicated by the color bars. In **(a)** 6 pairs of diffuse reflectance standards ( $R = (0.99, 0.52)$  for each pair) can be seen, arranged on the frame to the left and right side of the snow profile. In **(b)** no transmittance standards are available. Instead,  $Tr$  is calibrated against the homogeneous plastic sheet used for normalization ( $Tr = 0.06$ ).

erally, each of the thicker layers represents the combined snowfall events of one Antarctic winter (colored in green to red).

Reflectance and transmittance images are obtained from the normalized intensity images in Figure 6.6 by calibrating every pixel intensity against reflectance standards and white plastic-sheet transmittance, respectively. Applying the DISORT-calculated calibration results in Figures 6.2 and 6.5 to reflectance and transmittance images, OED and density can then be derived. The results along one vertical snow-profile line are presented in Figure 6.7. No comparison to OED and density values which have been obtained by quantitative measurement methods is available, yet. So, the presented optical OED and density measurements are only compared to qualitative considerations and hand measurements, respectively.

The OED analysis in Figure 6.7(a) yields a realistic range of  $100 \mu\text{m} < \text{OED} \leq 1500 \mu\text{m}$ . Additionally, the OED trend meets general expectations for Antarctica: (i) Fine-grained snow with very low OEDs is found near the surface, as strong winds in Antarctica break apart larger snow crystals. With increasing depth, OED increases due to ongoing undisturbed snow metamorphism. The deeper inside the snow cover the longer is the duration for which the snow microstructure has coarsened toward a microstructure with larger OEDs. Finally, sharp boundaries inside the snow cover are reproduced by the calculated OED profile. Near profile positions of 120 and 300 mm a visual inspection of the background intensity image shows clear boundaries between different snow types. This is also seen by a sharp increase in OED at these positions.

In contrast to the OED profile, an analysis of the density profile in Figure 6.7(b) is not as

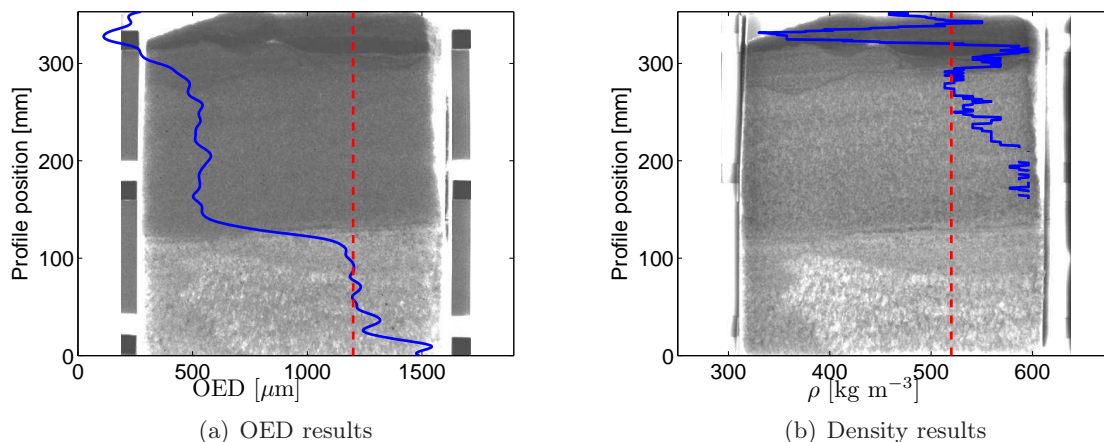


**Figure 6.7:** OED and density (blue lines) along one vertical profile line (marked by red dashed line) with background images of normalized intensity. Interruptions in the density profile line are caused by a combination of measured transmittance and calculated OED outside of the calculation domain in Figure 6.5.

straight-forward. Large parts of the profile cannot be analyzed, as the density exceeds the maximum density which was assumed for the calibration calculations  $\rho_{\max} = 600 \text{ kg m}^{-3}$  (see Figure 6.5). Nevertheless, the general density trend is as expected: Density increases toward the bottom due to snow settling with time. Contrary to the OED profile, however, where high OEDs are only found deeper inside the snow cover, very dense snow can also be observed near the surface. This can once again be explained by wind, which not only breaks snow crystals into smaller crystals but also presses the finer snow crystals into a denser snow microstructure.

Density is additionally determined by weighing four snow samples. The results of these measurements indicate a density range of  $300 \text{ kg m}^{-3} < \rho \leq 450 \text{ kg m}^{-3}$  for the analyzed snow profile. Most of the optically measured snow densities exceed this range substantially. However, density measurements by weighing are difficult to perform in Antarctica, as isolating a specified snow volume for weighing is complicated by very hard snow. Thus, a more detailed quantitative comparison does not offer a deeper understanding. More quantitative insight could be gained by comparing optical OED and density measurements with values obtained from micro-CT, for example. This has already been demonstrated for a comparison of reflectance and transmittance measurements with simulation results in Chapters 4 and 5, and is at work for the investigated profile.

A crucial point of the density analysis is the transmittance calibration. A first test by measuring transmittance of a white plastic sheet with the presented photography setup is used in this analysis. Other methods may lead to a different calibration and thus to different transmittance and density measurements. Changing the calibration transmittance of the white plastic sheet from  $Tr = 0.06$  to  $Tr = 0.08$  already leads to lower densities along the measured vertical profile line and to a smaller fraction of  $\rho > 600 \text{ kg m}^{-3}$ . Finding a more accurate and reliable method to calibrate measured normalized intensity against

transmittance is probably the most important improvement to the presented measurement method. Only then, snow density can be measured accurately together with OED by the suggested measurement principle.

## 6.3 Conclusions

First results of a combined high-resolution optical snow OED and density measurement method have been presented. Along one Antarctic snow profile, OED is determined by NIR reflectance photography. Density is then derived from green-light transmittance photographs.

Snow-slab transmittance at green-light wavelengths is not affected by snow impurities like soot for 7 probed snow slabs. Additionally, using illumination at visible wavelengths permits a higher measurement resolution and the use of thicker snow slabs, which are easier to prepare in the field.

The presented OED analysis along one vertical profile line yields realistic OED values of  $100 \mu\text{m} < \text{OED} \leq 1500 \mu\text{m}$  and qualitatively identifies snow inhomogeneities which can clearly be observed by visual inspection. A detailed comparison to OED values measured by an alternative technique is not yet available.

Snow density measurements with the presented methodology also show a reasonable trend within the snow cover. However, the derived values overestimate expected densities, which are obtained by weighing small snow samples of a known volume. Densities of  $\rho > 600 \text{ kg m}^{-3}$  are deduced from the translucent snow-profile photograph, while the expected density range is  $300 \text{ kg m}^{-3} < \rho \leq 450 \text{ kg m}^{-3}$ .

The most crucial point for a quantitative density analysis is the transmittance calibration, as no well-specified transmittance standards have been available. To implement an accurate calibration, the used method to measure overall transmitted intensity of a white plastic sheet needs further analysis. For the measured transmittance value of  $Tr = 0.06$  even small absolute uncertainties can have a great effect on resulting densities. Thus, the first step toward improving the presented optical measurement method is finding an accurate calibration process.



## 7 Summary

In this thesis radiative transfer at visible and near-infrared (NIR) wavelengths in pure snow (ice and air) is analyzed by experiments and model calculations. Different theoretical approaches to radiative transfer are applied to real snow samples and compared with measurements. The aim is to determine which simplifications to general radiative transfer theory and to the true 3D snow microstructure can be assumed to still guarantee an adequate description of radiative transfer in snow. The analysis focuses on the optical properties reflectance and transmittance and the snow microstructural parameters specific surface area (SSA, equivalent to optical equivalent snow grain size (OED)) and density.

Four different models are applied to analyze the presented snow measurements. In order of increasing complexity and capabilities, these models are: AFE, DISORT, FRED and CTMC. AFE neglects all effects caused by the finite extensions of a snow block and thus cannot explain any of the presented reflectance and transmittance measurements. DISORT considers a layered medium of specified finite thickness, which consists of spherical particles and extends infinitely to the sides. In contrast to DISORT, CTMC uses the true 3D snow microstructure as model input. Thus, CTMC transmittance calculations also agree better with measurements of highly anisotropic snow. While FRED is also based on the equivalent snow microstructure of spherical ice grains like DISORT, FRED permits implementing the complex boundary conditions of the presented reflectance measurements. Here, FRED is used to explain snow reflectance measurements with a ‘simple’ reflectometer (called InfraSnow). A detailed summary of the thesis including major results is given in the following.

Chapter 1 introduces the material snow and its bicontinuous 3D microstructure, traditional snow measurements and current quantitative measurement methods. Among these, micro-computed tomography (micro-CT) is crucial to the presented analysis, as the microstructural input parameters of all optical simulations are obtained by this technique.

In Chapter 2 the fundamental radiative transfer equation (RTE) is presented as an introduction to modeling radiative transfer. This integro-differential equation specifies the intensity change of radiation propagating inside a medium. The three fundamental effects of radiative transfer are explained: scattering, absorption and emission. At visible to NIR wavelengths scattering dominates radiative transfer in snow in contrast to the non-scattering constituents of pure snow.

An order of magnitude estimate demonstrates that

- the influence of thermal emission on radiative transfer in snow can be neglected at visible and NIR wavelengths.

Modeling radiative transfer in snow is discussed in Chapter 3. Three different approaches, which are used in four models, are presented: (i) DISORT, a model that solves the RTE for an equivalent snow microstructure of OED ice spheres and the correct density,

(ii) Monte-Carlo ray tracing based on the true 3D snow microstructure (by the CTMC model) or the equivalent snow microstructure (by the FRED model) and (iii) asymptotic flux extinction theory (AFE), which yields reflectance and transmittance for an infinite snow block of the equivalent snow microstructure of OED ice spheres. DISORT, CTMC and AFE calculations are compared for five real snow samples both on the particle and pore scale and for overall reflectance and transmittance of macroscopic snow slabs.

The most important results of the optical simulations are:

- Calculated particle- and pore-level radiative properties show qualitative similarities (like trends) but also significant quantitative differences between pore-scale CTMC simulations and single-scattering properties for DISORT and AFE, which are calculated by Mie theory.
- Comparing reflectance and transmittance results by (i) CTMC for the true microstructure and (ii) CTMC applied to an equivalent collection of ice spheres shows that the best approximation of the true snow microstructure is an equivalent collection of OED ice spheres with the correct snow density, i.e. keeping SSA and density of the original snow microstructure.
- A comparison of DISORT to CTMC reflectance and transmittance results shows the same trends and similar quantitative deviations between the two models for diffuse and collimated irradiation.
- For both diffuse and collimated irradiation, DISORT reflectance calculations agree better with CTMC results than transmittance calculations.
- The differences between DISORT and CTMC results are mainly the result of simplifying radiative transfer theory (DISORT assumes one homogeneous material described by effective radiative properties instead of two explicitly separated phases ice and air). The approximation of the snow microstructure as a collection of OED ice spheres with the correct density has a minor effect on the results.
- Reflectance and transmittance results of the AFE approach differ far more from DISORT and CTMC results than these two from each other. Compared to DISORT and CTMC, AFE theory clearly overestimates both reflectance and transmittance due to its inability to account for the finite extensions of all analyzed snow slabs.
- Calculation results for reflectance and transmittance by AFE theory show smaller variations between the five analyzed snow slabs than results obtained by DISORT or CTMC. The two latter models produce clearly distinguishable reflectance and transmittance spectra for all analyzed snow slabs consisting of different snow types.

Reflectance measurements of snow are presented in Chapter 4. Here, the InfraSnow is used to measure reflectance and investigate the possibility to derive snow OED. The InfraSnow is a novel compact device measuring diffuse NIR reflectance by an integrating-sphere detector design. Measured reflectance values of four snow slabs are compared to reflectance calculations by the DISORT, AFE and FRED models. Input parameters for

---

all three models are SSA (or OED) and density obtained from micro-CT scans of snow samples which have been taken from the probed snow slabs.

The InfraSnow analysis shows that

- specular reflections at the surface of the probed material can alter the measurements and falsify an interpretation as purely diffuse reflectance.
- DISORT and AFE theory cannot explain measured reflectance values due to the inability to specify radiation losses to the sides.
- InfraSnow reflectance measurements can be reproduced within the natural spatial variability of the probed snow slabs with the FRED model. While based on the same equivalent snow microstructure as DISORT and AFE, FRED also permits implementing the exact geometry of the InfraSnow.
- accounting for the appropriate geometrical boundary conditions in FRED, only snow OED and density are required as model input parameters to predict reflectance within the natural snow variability.
- the limiting factor of the analysis is the spatial variability of the probed snow slabs. By knowing snow density prior to the InfraSnow measurements with an accuracy of  $\sim 50 \text{ kg m}^{-3}$ , snow OED and thus SSA can be measured within the spatial variability of the probed snow slab by the InfraSnow.

In Chapter 5 transmittance measurements are compared to calculations by the DISORT, AFE and CTMC models. Diffuse transmittance at two NIR wavelengths is analyzed for eight snow types by a spectrometer. Again, micro-CT scans of the snow microstructure are used as input for the transmittance calculations of each probed snow slab.

The transmittance analysis leads to the following results:

- AFE theory cannot describe the presented transmittance measurements adequately. This is explained by the inability of this model to account for the finite extensions of the probed snow slabs.
- Both DISORT and CTMC results agree well with measured transmittance values. For most analyzed snow slabs transmittance measurements fall inside the transmittance range which is calculated by the two models, according to the natural snow variability obtained from the micro-CT snow samples.
- The only transmittance measurements which clearly cannot be reproduced by DISORT are found for a snow slab of machine-made snow. This extreme case of an anisotropic and layered snow microstructure demonstrates the limited ability of modeling the true 3D snow microstructure as a collection of OED ice spheres in DISORT.

The final Chapter 6 forms an outlook to a combined method to measure snow OED and density by reflectance and translucent snow-profile photography. Here, OED is derived from NIR reflectance of one undisturbed semi-infinite snow-pit wall in Antarctica. Density

across the same snow profile is determined by isolating a translucent snow-pit wall and taking an image of the backlit snow profile under green-light illumination. The correlation between reflectance and OED and between transmittance, OED and density is calculated by DISORT.

The major findings of this chapter are:

- The analysis of the presented transmittance measurements at green-light wavelengths instead of NIR light shows no deviation which can be attributed to snow impurities.
- Transmittance of thicker snow slabs ( $\sim 5$  cm) is substantially higher for green light than for NIR light. Thus, measurements with green light offer a better signal strength and permit analyzing a thicker snow-profile wall, which is easier to prepare in the field.
- The presented method yields realistic OED values and clearly identifies regions of different snow types.
- The obtained density profile shows a realistic trend inside the snow cover. However, quantitative results are higher than expected. This disagreement is caused by the highly sensitive calibration process, which is used to calculate transmittance from the detected intensities.
- To improve the quantitative results of the suggested density measurement method, an improvement of the calibration is paramount. Then, both OED and density can be measured optically.

# Appendix



# A Snow Characterization by Facet Number and Size from Snow-Pit Wall Photographs

This chapter describes the first attempts to characterize snow by the number and size of present facets, i.e. planar ice faces, within the snow microstructure and how to detect them by photography. Just like density and SSA, facet number and size are microstructural parameters that describe a snow type. Part of the description and results of this chapter have been published in:

Gergely, M., and Schneebeli, M., 2010: Snow characterization by facet number and size from snow pit wall photographs, In *Proceedings of the 2010 International Snow Science Workshop*, p. 380–382.

## A.1 Introduction

Snow grain type is one of the major properties recorded in a snow profile as the snow stratigraphy determines the stability or instability of the present snowpack. Persistent weak layers within a snow cover where dry slab avalanches initiate are composed of snow types with planar faces in contrast to snow with a rounded structure. Snow types that form these weak layers are faceted crystals, surface and depth hoar (*Schweizer et al.*, 2003). So, faceted snow is a good indicator for an unstable snowpack (*Schweizer and Lütschg*, 2001).

One crucial observation for avalanche forecasting is the distinction between snow which is mainly composed of facets and rounded snow grains or crusts. In recent years optical measurements of snow have been performed to quantify snow and ice properties like grain size, density and light absorption by diffuse reflectance and transmittance measurements (*Warren et al.*, 2006; *Matzl and Schneebeli*, 2006; *Gallet et al.*, 2009; *Gergely et al.*, 2010). Here, multiple scattering within the snow cover is analyzed to determine physical properties which are integrated properties over a snow volume of several  $\text{cm}^3$  depending on the wavelength of the used illumination and the snow type. However, it has not been possible to gain information on grain shape from these methods.

In this study, first steps are presented towards a snow-profile analysis using facet number and size as the discriminating factors for snow stratigraphy. The method is based on simple snow pit wall photographs. Theory and methodology are explained in the following Section A.2. Then, first test results of a snow-pit wall consisting of 3 distinct snow layers are shown. This leads to an outlook of this preliminary study, which future steps are necessary for a detailed and quantitative analysis.

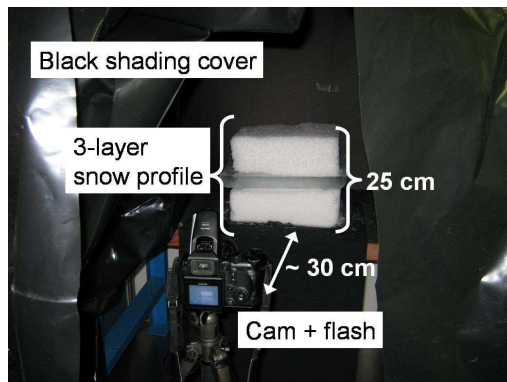


**Figure A.1:** Experimental setup in the laboratory for snow-pit wall photography. The analyzed snow-pit wall consists of 3 distinct layers: Depth hoar, solid ice and small faceted snow (top to bottom).

## A.2 Snow-pit wall photography

The presented measurement method is based on specular reflections from planar air-to-ice interfaces within the snow. These reflections are detected by a digital camera and can then be correlated to facet number and size within the snow.

### A.2.1 Background

In contrast to diffuse reflectance of snow, specular reflection highlights are caused by a mirror-like reflection of light at an air-to-ice interface. This is a single reflection event at the ice surface and not multiple scattering inside a snow volume as it has been the focus of Chapters 3 to 6.

If the angle of incident parallel light is equal to the viewing angle of the observer with respect to the reflecting surface a bright specular highlight is visible. For all other viewing directions only the diffuse white background reflectance from multiple scattering within the snow can be detected.

According to the international snow classification (*Fierz et al.*, 2009) it is expected to find more and larger specular highlights for snow types with large planar faces than for snow types consisting mainly of rounded ice structures.

### A.2.2 Method

The experimental setup in the laboratory is shown in Figure A.1. The principles of this simple construction can be easily transferred to a field measurement method: An image of a snow-pit wall is taken by a digital camera with flash while the surrounding light is blocked by a black cover.

Here, a Canon PowerShot A480 is used in automatic exposure and flash mode with ISO sensitivity set to 200. These turned out to be simple settings which produce photos with the desired accuracy for a later quantitative image analysis. Snow-layer thicknesses are chosen large enough that each layer is clearly discernable on the resulting photo and thin enough that they can still be pictured completely in a single photo. No zoom is used.

The flash serves as a source of directional light. Although a camera flash does not emit perfectly parallel light we found it to be sufficient and simple to use for our test

measurements.

For the analysis the RGB images are first converted to an intensity images. Then, an image of the diffuse background reflectance is obtained by a morphological opening of the intensity image. The size of the structure element to perform the opening is chosen manually so that the biggest visible specular highlight of the normalized image is just removed. This background image is then subtracted from the original intensity image to obtain an image which only shows the intensity differences to the diffuse multiple-scattering background.

Finally, a binary image is created by thresholding. Here, black represents the pixels of diffuse background reflectance while the specular highlights show up in white. The threshold intensity to produce a binary image from the difference image is also chosen manually from visual inspection of difference and resulting binary image. Number and size of the highlight regions in the binary image which represent specular reflections of facets can then be analyzed for different regions of interest (ROIs) of the snow-pit wall.

The image-analysis results are compared with facet measurements by micro-CT. A small snow volume located in a region corresponding to the snow area analyzed by photography is scanned in the micro-CT. Then, a facet voxel is assigned to an ice surface voxel if after smoothing both principal curvatures at this location are close to 0 below a chosen threshold.

The presented measurement method is based on the detection of planar ice faces within the snow by taking only one picture from one viewing direction. Obviously, with a single photo only a small fraction of the total number of planar faces can be detected. Nevertheless, if the distribution of these facets within the snow is isotropic one single image which shows a sufficiently large cross-sectional area of the snow can reproduce this distribution accurately.

Even for a sample of depth hoar snow, where the greatest anisotropy is expected, it is found that the planar faces are indeed distributed approximately isotropically. This isotropic distribution of facets in contrast to an anisotropic fracture strength or thermal conductivity is due to the complex vapor flux throughout the 3D snow microstructure. An exemplary micro-CT image of depth hoar with highlighted facets is shown in Figure A.2.

## A.3 Test results

Three clearly differing layers are chosen to build the test snow profile: Depth hoar (DH), a solid ice layer and fine-grained faceted snow (FC). Thus, results for all layers should differ strongly. This is important to investigate the principal effects and correlations between snow microstructure and specular highlights in this first study while subtle effects can still be ignored. DH and FC snow microstructure and characteristics are shown and listed in Figure A.3 and Table A.1.

Four parameters of the facet analysis based on the micro-CT data are presented in Table A.2. The results confirm the general expectations for these snow types. The smallest difference between DH and FC sample results is found for the ratio of facet number to ice area as both are snow types containing facets. And even here, the values differ by about 20%. The greatest degree of separation is calculated for the maximum facet area.

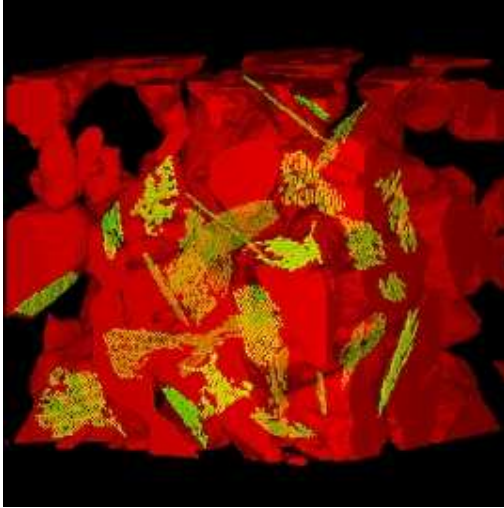
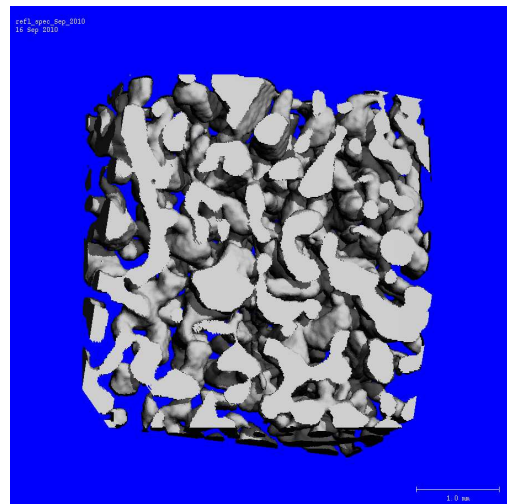


**Figure A.2:** Micro-CT scan of a  $3 \times 3 \times 3 \text{ mm}^3$  depth hoar snow sample. Ice is shown in red, facets are highlighted in green. Image created by T. Theile.



(a) Depth hoar (DH)



(b) Faceted snow (FC)

**Figure A.3:** Snow microstructure for DH and FC snow samples scanned by micro-CT. Pictured volumes have a projection area of  $12 \times 12 \text{ mm}^2$  (DH) and  $4 \times 4 \text{ mm}^2$  (FC).

**Table A.1:** Snow properties of DH and FC samples: Hand-measured grain size (see Chapter 1.1), CT-measured density  $\rho$  and SSA.

Snow type sample	Hand grain size [mm]	$\rho$ [kg m <sup>-3</sup> ]	SSA [mm <sup>-1</sup> ]
DH	1–4	270–300	8.1–8.6
FC	0.3–1	340–370	13.7–14.5

This is also readily explained as DH snow exhibits much larger ice structures and thus the potential for much larger facets than FC snow (cf. Figures A.3(a) and A.3(b)). All four parameters trivially reduce to 0 inside a perfectly solid and homogeneous ice layer.

**Table A.2:** Micro-CT facet analysis for subvolumes of DH and FC snow samples pictured in Figure A.3. Third ‘snow type’ of the snow-pit wall is a solid ice layer (all 4 parameters = 0).

Snow type sample	$\frac{\text{Facet number}}{\text{Ice area}}$	$\frac{\text{Facet area}}{\text{Ice area}}$	Mean facet area	Max. facet area
DH	4.3 mm <sup>-2</sup>	0.28	0.07 mm <sup>2</sup>	3.8 mm <sup>2</sup>
FC	5.3 mm <sup>-2</sup>	0.09	0.02 mm <sup>2</sup>	0.1 mm <sup>2</sup>

Corresponding parameters for the specular highlight analysis of the test snow-pit wall photograph are listed in Table A.3. Raw histograms of the highlight area are plotted in Figure A.4. Here, a manually chosen region of interest (ROI) inside each snow layer (DH, ice and FC) is analyzed according to the description in Section A.2.2. For the ROI of each snow type the four parameters are retrieved to characterize the specular highlights (not actual facets). The resolution of the used photography setup (shown in Figure A.1) is  $\sim 0.01$  mm<sup>2</sup> per pixel.

**Table A.3:** Highlight analysis for three ROIs corresponding to the three snow layers in the snow-pit wall photograph.

Snow ROI	$\frac{\text{Highlight number}}{\text{ROI}}$	$\frac{\text{Highlight area}}{\text{ROI}}$	Mean highlight area	Max. highlight area
DH	0.8 mm <sup>-2</sup>	0.03	0.03 mm <sup>2</sup>	1.3 mm <sup>2</sup>
Ice	0.05 mm <sup>-2</sup>	10 <sup>-3</sup>	0.03 mm <sup>2</sup>	0.4 mm <sup>2</sup>
FC	2.3 mm <sup>-2</sup>	0.09	0.04 mm <sup>2</sup>	0.9 mm <sup>2</sup>

The histograms in Figure A.4 show that for all 3 snow types specular highlight areas of 1 to several pixels are by far the most common. So, the mean specular highlight areas in Table A.3 are still within 30% of each other. Thus, this parameter is of little use to distinguish different snow types. As an extreme example, an ice layer cannot be distinguished from a DH layer in the presented analysis.

All other parameters in Table A.3, however, show clear differences for the 3 snow types. The results agree with general expectations for these snow types according to the international snow classification in *Fierz et al.* (2009). Furthermore, the values agree qualitatively

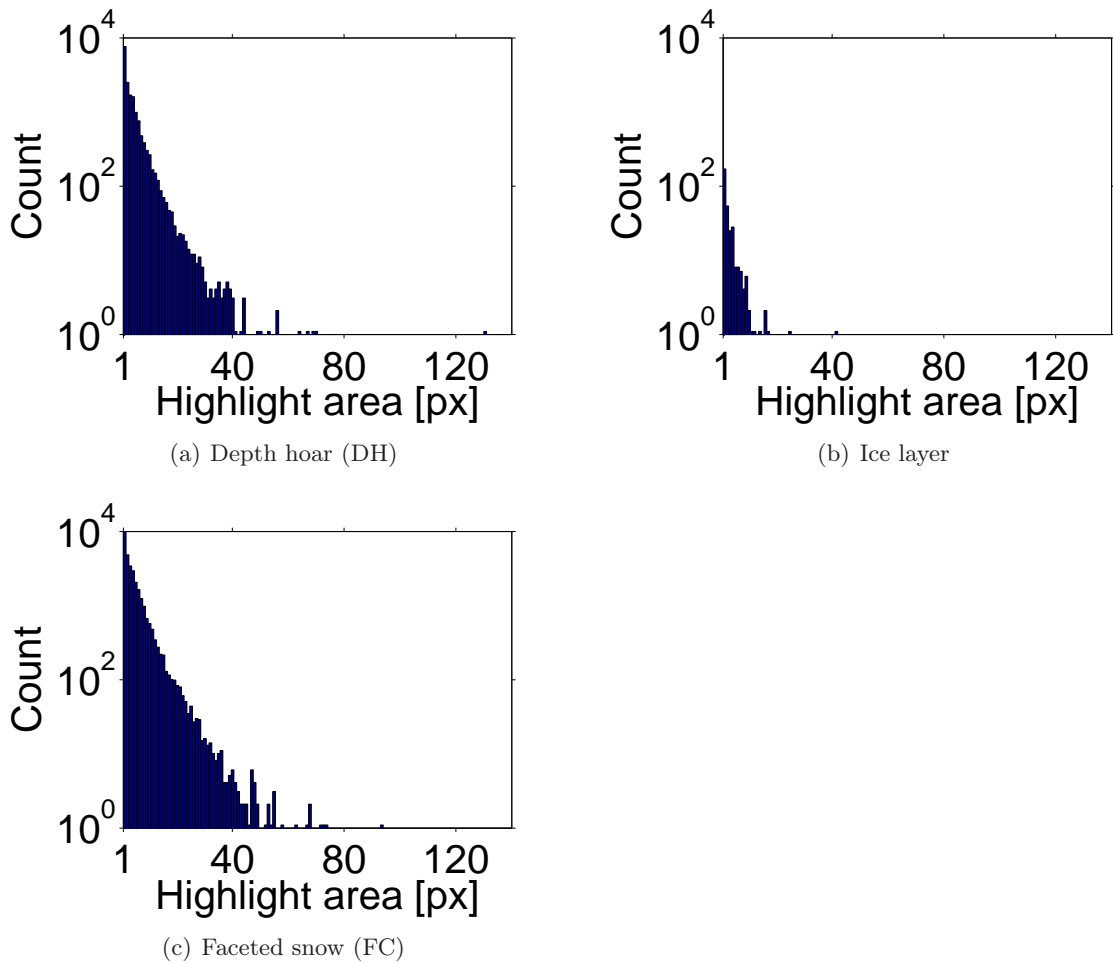


**Figure A.4:** Histograms of specular highlight area for the 3 layers of the snow-pit wall. Calculations are performed for the same ROIs as in Table A.3.

with the results from the micro-CT analysis. Due to the different sampling spaces in 2D and 3D for photo and micro-CT evaluation, respectively, and the variability introduced by manual thresholding for both analysis methods a close quantitative agreement is neither expected nor establishable. The discrepancies include the different trends between photo and micro-CT analysis for the comparison of highlight area per ROI with facet area per ice area. The fraction of specular highlights is lower for DH than for FC snow.

As expected and evident in the results of both photo and micro-CT analysis, depth hoar contains the largest detected specular highlights and facets.

Choosing other parameters which are easily derived from the area of the specular highlights like a diameter for equivalent spheres or an equivalent-ellipsoid major axis length does not alter the results significantly.

Thresholding (see Section A.2.2), however, does have a strong effect on the results. If the threshold is chosen too high to create the binary image of specular highlights

larger contiguous regions of specular highlights which can already be identified visually in the original image shrink excessively. If the threshold value is chosen too low intensity variations which are not caused by specular highlights (like variations due to small ridges and grooves in the snow-pit wall) are falsely recognized as such and thus attributed to facets which are not present in the photographed snow profile. However, in between these two extremes the choice of the threshold only has a minor effect on the parameters presented in Table A.3.

## **A.4 Conclusions and outlook**

First results of one snow-pit wall analysis for three snow types are presented to deduce facet number and size from characterizing the specular highlights in the image.

While a quantitative interpretation is not yet possible general expectations, optical and micro-CT measurements agree qualitatively for the parameters maximum facet or highlight area and facet or highlight number per ice area or ROI, respectively. Due to the domination of highlight areas of only 1 to few pixels for all snow types a more detailed analysis for the extreme values of the measured highlight area should be performed. In connection with a better understanding of ‘correct’ thresholding criteria both for photo highlight and micro-CT facet analysis this could reveal a quantitative correlation between the resulting parameters of both methods.

On the experimental side, the next step is a measurement of a snow-pit wall containing more snow types including round-grained snow. Snow samples can then again be taken and analyzed by micro-CT to compare those measurements of facet number and size to the specular highlights detected in the snow-pit wall photograph.



## B Bibliography

- Aoki, T., T. Aoki, M. Fukabori, A. Hachikubo, Y. Tachibana, and F. Nishio, 2000: Effects of snow physical parameters on spectral albedo and bidirectional reflectance of snow surface, *J. Geophys. Res.* **103**, 10,219–10,236.
- Arnaud, L., G. Picard, N. Champollion, F. Domine, J. C. Gallet, E. Lefebvre, M. Fily, and J. M. Barnola, 2011: Measurement of vertical profiles of snow specific surface area with a 1 cm resolution using infrared reflectance: instrument description and validation, *J. Glaciol.* **57**, 17–29.
- Arridge, S. R., 1999: Optical tomography in medical imaging, *Inverse Problems* **15**, R41–R93.
- Bänninger, D., P. Lehmann, and H. Flühler, 2006: Modelling the effect of particle size, shape and orientation of light transfer through porous media, *Eur. J. Soil Sci.* **57**, 906–915.
- Bänninger, D., C. S. Bourgeois, M. Matzl, and M. Schneebeli, 2008: Reflectance modeling for real snow structures using a beam tracing model, *Sensors* **8**, 3482–3496.
- Baptista, J., P. Felizardo, J. C. Menezes, and M. J. Neiva Correia, 2008: Monitoring the quality of oils for biodiesel production using multivariate near infrared spectroscopy models, *J. Near Infrared Spectrosc.* **16**, 445–454.
- Beaglehole, D., B. Ramanathan, and J. Rumberg, 1998: The UV to IR transmittance of Antarctic snow, *J. Geophys. Res.* **103**, 8849–8857.
- Boas, D. A., D. H. Brooks, E. L. Miller, C. A. DiMarzio, M. Kilmer, R. J. Gaudette, and Q. Zhang, 2001: Imaging the body with diffuse optical tomography, *IEEE Signal Process. Mag.* **18**, 57–75.
- Bohren, C. F., 1987: Multiple scattering of light and some of its observable consequences, *Am. J. Phys.* **55**, 524–533.
- Born, M., and E. Wolf, 1999: *Principles of optics*, ISBN 0 521 642221, 7th ed., Cambridge University Press.
- Brzoska, J.-B., F. Flin, B. Lesaffre, C. Coléou, P. Lamboley, J. F. Delesse, B. L. Saëc, and G. Vignoles, 2001: Computation of the surface area of natural snow 3D images from X-ray tomography: two approaches, *Image Anal. Stereol.* **20**, 306–312.
- Chandrasekhar, S., 1950: *Radiative transfer*, ISBN 0-486-60590-6, Dover Publications Inc.

- Colbeck, S. C., 1991: The layered character of snow covers, *Rev. Geophys.* **29**, 81–96.
- Colbeck, S. C., 1992: A review of the processes that control snow friction, *Monograph 92-2*, U.S. Army CRREL.
- Coléou, C., B. Lesaffre, J.-B. Brzoska, W. Ludwig, and E. Boller, 2001: Three-dimensional snow images by X-ray microtomography, *Ann. Glaciol.* **32**, 75–81.
- Domine, F., R. Salvatori, L. Legagneux, R. Salzano, M. Fily, and R. Casacchia, 2006: Correlation between the specific surface area and the short wave infrared (SWIR) reflectance of snow, *Cold Reg. Sci. Technol.* **46**, 60–68.
- Farmer, J. T., and J. R. Howell, 1998: Comparison of Monte Carlo strategies for radiative transfer in participating media, *Adv. Heat Transfer* **31**, 333–429.
- Fauve, M., H. Rhyner, A. Lüthi, M. Schneebeli, and M. Lehning, 2008: Putting snow knowledge into the development of winter sports equipment, *Sports Technol.* **1**, 145–151.
- Fierz, C., R. L. Armstrong, Y. Durand, P. Etchevers, E. Greene, D. M. McClung, K. Nishimura, P. K. Satyavali, and S. A. Sokratov, 2009: The International Classification for Seasonal Snow on the Ground, *Tech. rep.*, IHP-VII Technical Documents in Hydrology No 83, IACS Contribution No 1, UNESCO-IHP, Paris.
- Flanner, M. G., and C. S. Zender, 2006: Linking snowpack microphysics and albedo evolution, *J. Geophys. Res.* **111**, D12208.
- Flin, F., J.-B. Brzoska, B. Lesaffre, C. Coléou, and R. A. Pieritz, 2004: Three-dimensional geometric measurements of snow microstructural evolution under isothermal conditions, *Ann. Glaciol.* **38**, 39–44.
- Frost, D., 2008: Calibration, testing and design of a hand-held instrument for outdoor measurements of the grain size and the temperature of snow, Master’s thesis, Swiss Federal Institute of Technology (ETH) Zurich.
- Gallet, J.-C., F. Domine, C. S. Zender, and G. Picard, 2009: Rapid and accurate measurement of the specific surface area of snow using infrared reflectance at 1310 and 1550 nm, *The Cryosphere* **3**, 167–182.
- Gardner, A. S., and M. J. Sharp, 2010: A review of snow and ice albedo and the development of a new physically based broadband albedo parameterization, *J. Geophys. Res.* **115**, F01009.
- Gaston, E., J. M. Frías, P. J. Cullen, C. P. O’Donnell, and A. A. Gowen, 2010: Visible-near infrared hyperspectral imaging for the identification and discrimination of brown blotch disease on mushroom (*agaricus bisporus*) caps, *J. Near Infrared Spectrosc.* **18**, 341–353.
- Gergely, M., M. Schneebeli, and K. Roth, 2010: First experiments to determine snow density from diffuse near-infrared transmittance, *Cold Reg. Sci. Technol.* **64**, 81–86.

- Gibson, A. P., J. C. Hebden, and S. R. Arridge, 2005: Recent advances in diffuse optical imaging, *Phys. Med. Biol.* **50**, R1–R43.
- Good, W., 1987: Thin sections, serial cuts and 3-D analysis of snow, in *IAHS Publ. 162. Avalanche Formation, Movement and Effects*, pp. 35–48.
- Good, W., G. Krüsi, J. v.Niederhäusern, and A. Roth, 1991: Preparation and analysis of high contrast stratigraphic profiles, in *Comptes rendus: Symp. Chamonix 4.–8. Juin*, pp. 40–45, CISA-IKAR-ANENA.
- Grenfell, T. C., and S. G. Warren, 1999: Representation of a nonspherical ice particle by a collection of independent spheres for scattering and absorption of radiation, *J. Geophys. Res.* **104**, 31,697–31,709.
- Grenfell, T. C., S. P. Neshyba, and S. G. Warren, 2005: Representation of a nonspherical ice particle by a collection of independent spheres for scattering and absorption of radiation: 3. Hollow columns and plates, *J. Geophys. Res.* **110**, D17203.
- Harper, J. T., and J. H. Bradford, 2003: Snow stratigraphy over a uniform depositional surface: spatial variability and measurement tools, *Cold Reg. Sci. Technol.* **37**, 289–298.
- Haussener, S., W. Lipiński, J. Petrasch, P. Wyss, and A. Steinfeld, 2009: Tomographic characterization of a semitransparent-particle packed bed and determination of its thermal radiative properties, *J. Heat Transfer* **131**, 072701.
- Haussener, S., P. Coray, W. Lipiński, P. Wyss, and A. Steinfeld, 2010: Tomography-based heat and mass transfer characterization of reticulate porous ceramics for high-temperature processing, *J. Heat Transfer* **132**, 061201.
- Henye, L. G., and J. L. Greenstein, 1941: Diffuse radiation in the galaxy, *Astrophys. J.* **93**, 70–83.
- Hug, M., and S. Trunz, 2006: InfraSnow, unpublished thesis, abstract available at [http://www.ntb.ch/files/0/2787/2006\\_Abtract\\_SLF.pdf](http://www.ntb.ch/files/0/2787/2006_Abtract_SLF.pdf).
- Kaempfer, T. U., and M. Schneebeli, 2007: Observation of isothermal metamorphism of new snow and interpretation as a sintering process, *J. Geophys. Res.* **112**, D24101.
- Kaempfer, T. U., M. Schneebeli, and S. A. Sokratov, 2005: A microstructural approach to model heat transfer in snow, *Geophys. Res. Lett.* **32**, L21503.
- Kaempfer, T. U., M. A. Hopkins, and D. K. Perovich, 2007: A three-dimensional microstructure-based photon-tracking model of radiative transfer in snow, *J. Geophys. Res.* **112**, D24113.
- Kerbrat, M., B. Pinzer, T. Huthwelker, H. W. Gäggeler, M. Ammann, and M. Schneebeli, 2008: Measuring the specific surface area of snow with X-ray tomography and gas adsorption: comparison and implications for surface smoothness, *Atmos. Chem. Phys.* **8**, 1261–1275.

- Kokhanovsky, A. A., and T. Y. Nakajima, 1998: The dependence of phase functions of large transparent particles on their refractive index and shape, *J. Phys. D* **31**, 1329–1335.
- Kokhanovsky, A. A., and E. P. Zege, 2004: Scattering optics of snow, *Appl. Opt.* **43**, 1589–1602.
- Kolokolova, L., H. Kimura, K. Ziegler, and I. Mann, 2006: Light-scattering properties of random-oriented aggregates: Do they represent the properties of an ensemble of aggregates?, *J. Quant. Spectrosc. Radiat. Transfer* **100**, 199–206.
- Kuipers Munneke, P., M. R. van den Broeke, C. H. Reijmer, M. M. Helsen, W. Boot, and M. Schneebeli, 2009: The role of radiation penetration in the energy budget of the snowpack at Summit, Greenland, *The Cryosphere* **3**, 155–165.
- Legagneux, L., A. Cabanes, and F. Domine, 2002: Measurement of the specific surface area of 176 snow samples using methane adsorption at 77 K, *J. Geophys. Res.* **107**, 4335.
- Lipiński, W., D. Keene, S. Haussener, and J. Petrasch, 2010a: Continuum radiative heat transfer modeling in media consisting of optically distinct components in the limit of geometrical optics, *J. Quant. Spectrosc. Radiat. Transfer* **111**, 2474–2480.
- Lipiński, W., J. Petrasch, and S. Haussener, 2010b: Application of the spatial averaging theorem to radiative heat transfer in two-phase media, *J. Quant. Spectrosc. Radiat. Transfer* **111**, 253–258.
- Macke, A., and M. I. Mishchenko, 1996: Applicability of regular particle shapes in light scattering calculations for atmospheric ice particles, *Appl. Opt.* **35**, 4291–4296.
- Macke, A., M. I. Mishchenko, K. Muinonen, and B. E. Carlson, 1995: Scattering of light by large nonspherical particles: ray-tracing approximation versus T-matrix method, *Opt. Lett.* **20**, 1934–1936.
- Matzl, M., and M. Schneebeli, 2006: Measuring specific surface area of snow by near-infrared photography, *J. Glaciol.* **52**, 558–564.
- McGlone, V. A., and P. J. Martinsen, 2004: Transmission measurements on intact apples moving at high speed, *J. Near Infrared Spectrosc.* **12**, 37–43.
- Meirolid-Mautner, I., and M. Lehning, 2004: Measurements and model calculations of the solar short wave fluxes in snow on Summit, Greenland, *Ann. Glaciol.* **38**, 279–284.
- Mie, G., 1908: Beiträge zur Optik trüber Medien, speziell kolloidaler Metallösungen, *Ann. Phys.* **330**, 377–445.
- Mishchenko, M. I., 2002: Vector radiative transfer equation for arbitrarily shaped and arbitrarily oriented particles: a microphysical derivation from statistical electromagnetics, *Appl. Opt.* **41**, 7114–7134.

- Mishchenko, M. I., 2008: Multiple scattering, radiative transfer, and weak localization in discrete random media: unified microphysical approach, *Rev. Geophys.* **46**, RG2003.
- Mishchenko, M. I., L. D. Travis, and A. A. Lacis, 2002: *Scattering, absorption, and emission of light by small particles*, ISBN 0-521-78252-X, Cambridge University Press.
- Moffat, A. C., S. Assi, and R. A. Watt, 2010: Identifying counterfeit medicines using near infrared spectroscopy, *J. Near Infrared Spectrosc.* **18**, 1–15.
- Nakajima, T. Y., T. Nakajima, and A. A. Kokhanovsky, 1998: Radiative transfer through light scattering media with nonspherical large particles: direct and inverse problems, *Proc. SPIE* **3220**, 2–12.
- Nakamura, H., 1978: A new apparatus to produce fresh snow (in Japanese), in *Report of the National Research Center for Disaster Prevention*, 19.
- Neshyba, S. P., T. C. Grenfell, and S. G. Warren, 2003: Representation of a nonspherical ice particle by a collection of independent spheres for scattering and absorption of radiation: 2. Hexagonal columns and plates, *J. Geophys. Res.* **108**, 4448.
- Nolin, A. W., and J. Dozier, 2000: A hyperspectral method for remotely sensing the grain size of snow, *Remote Sens. Environ.* **74**, 207–216.
- Painter, T. H., and J. Dozier, 2004: Measurements of the hemispherical-directional reflectance of snow at fine spectral and angular resolution, *J. Geophys. Res.* **109**, D18115.
- Painter, T. H., N. P. Molotch, M. Cassidy, M. Flanner, and K. Steffen, 2007: Contact spectroscopy for determination of stratigraphy of snow optical grain size, *J. Glaciol.* **53**, 121–127.
- Petrasch, J., P. Wyss, and A. Steinfeld, 2007: Tomography-based Monte Carlo determination of radiative properties of reticulate porous ceramics, *J. Quant. Spectrosc. Radiat. Transfer* **105**, 180–197.
- Petrasch, J., S. Haussener, and W. Lipiński, 2010: Discrete vs. continuum level simulations of radiative transfer in semitransparent two-phase media, in *Proceedings of the 6th International Symposium on Radiative Transfer*, p. 10.
- Picard, G., L. Arnaud, F. Domine, and M. Fily, 2009: Determining snow specific surface area from near-infrared reflectance measurements: numerical study of the influence of grain shape, *Cold Reg. Sci. Technol.* **56**, 10–17.
- Pielmeier, C., and M. Schneebeli, 2003: Stratigraphy and changes in hardness of snow measured by hand, ram sonde and micro penetrometer: a comparison with planar sections, *Cold Reg. Sci. Technol.* **37**, 393–405.

- Pinzer, B., 2009: Dynamics of temperature gradient snow metamorphism, Ph.D. thesis, Swiss Federal Institute of Technology (ETH) Zurich.
- Reiweger, I., J. Schweizer, J. Dual, and H. J. Herrmann, 2009: Modelling snow failure with a fibre bundle model, *J. Glaciol.* **55**, 997–1002.
- Roesch, A., M. Wild, R. Pinker, and A. Ohmura, 2002: Comparison of spectral surface albedos and their impact on the general circulation model simulated surface climate, *J. Geophys. Res.* **107**, 4221.
- Schneebeli, M., and S. A. Sokratov, 2004: Tomography of temperature gradient metamorphism of snow and associated changes in heat conductivity, *Hydrol. Process.* **18**, 3655–3665.
- Schneebeli, M., C. Pielmeier, and J. B. Johnson, 1999: Measuring snow microstructure and hardness using a high resolution penetrometer, *Cold Reg. Sci. Technol.* **30**, 101–114.
- Schneebeli, M., S. Trunz, M. Hug, J. Jütz, and M. Staudenmann, 2009: Patent CH-698701, Verfahren und Gerät zur Messung der Schneebeschaffenheit.
- Schuster, A., 1905: Radiation through a foggy atmosphere, *Astrophys. J.* **21**, 1–22.
- Schweizer, J., and M. Lütschg, 2001: Characteristics of human-triggered avalanches, *Cold Reg. Sci. Technol.* **33**, 147–162.
- Schweizer, J., J. B. Jamieson, and M. Schneebeli, 2003: Snow avalanche formation, *Rev. Geophys.* **41**, 1016.
- Stamnes, K., S. C. Tsay, W. Wiscombe, and K. Jayaweera, 1988: Numerically stable algorithm for discrete-ordinate-method radiative transfer in multiple scattering and emitting layered media, *Appl. Opt.* **27**, 2502–2509.
- Tancrez, M., and J. Taine, 2004: Direct identification of absorption and scattering coefficients and phase function of a porous medium by Monte Carlo technique, *Int. J. Heat Mass Transfer* **47**, 373–383.
- Theile, T., D. Szabo, A. Lüthi, H. Rhyner, and M. Schneebeli, 2009: Mechanics of the ski-snow contact, *Tribol. Lett.* **36**, 223–231.
- Ungut, A., G. Grehan, and G. Gouesbet, 1981: Comparisons between geometrical optics and Lorenz-Mie theory, *Appl. Opt.* **20**, 2911–2918.
- van de Hulst, H. C., 1957: *Light scattering by small particles*, John Wiley & Sons, Inc., N.Y. Reprint: 1981, Dover Publications, ISBN 0-486-64228-3.
- Warren, S. G., 1982: Optical properties of snow, *Rev. Geophys.* **20**, 67–89.
- Warren, S. G., and R. E. Brandt, 2008: Optical constants of ice from the ultraviolet to the microwave: A revised compilation, *J. Geophys. Res.* **113**, D14220.

- Warren, S. G., and W. J. Wiscombe, 1980: A model for the spectral albedo of snow. II: Snow containing atmospheric aerosols, *J. Atmos. Sci.* **37**, 2734–2745.
- Warren, S. G., R. E. Brandt, and T. C. Grenfell, 2006: Visible and near-ultraviolet absorption spectrum of ice from transmission of solar radiation into snow, *Appl. Opt.* **45**, 5320–5334.
- Wielaard, D. J., M. I. Mishchenko, A. Macke, and B. E. Carlson, 1997: Improved T-matrix computations for large, nonabsorbing and weakly absorbing nonspherical particles and comparison with geometrical-optics approximation, *Appl. Opt.* **36**, 4305–4313.
- Wiscombe, W. J., and S. G. Warren, 1980: A model for the spectral albedo of snow. I: Pure snow, *J. Atmos. Sci.* **37**, 2712–2733.
- Xie, Y., P. Yang, B.-C. Gao, G. W. Kattawar, and M. I. Mishchenko, 2006: Effect of ice crystal shape and effective size on snow bidirectional reflectance, *J. Quant. Spectrosc. Radiat. Transfer* **100**, 457–469.
- Zhou, X., S. Li, and K. Stamnes, 2003a: Effects of vertical inhomogeneity on snow spectral albedo and its implication for optical remote sensing of snow, *J. Geophys. Res.* **108**, 4738.
- Zhou, X., S. Li, and K. Stamnes, 2003b: Geometrical-optics code for computing the optical properties of large dielectrical spheres, *Appl. Opt.* **42**, 4295–4306.



# Acknowledgments

This thesis would not have been possible and definitely not as much fun without the support from a lot of people: my parents, everyone at the WSL Institute for Snow and Avalanche Research SLF in Davos and all my friends. I would like to take this opportunity to thank all of you for helping me in many scientific discussions, for the help I received with all my computer-related problems, and last but not least, for making me enjoy the past 3.5 years as much as I did.

I would like to thank the following persons in particular:

- *Dr. Martin Schneebeli* who gave me the great opportunity to do a PhD thesis on this exciting topic as part of the snow-physics research team at the SLF. Thank you for always taking the time for many discussions and for important input to this thesis, while always giving me the freedom to follow my own ideas and concepts.
- *Prof. Kurt Roth* for accepting to be my supervisor at the Institute of Environmental Physics at Heidelberg University. Despite the geographical distance he was always available for comments and input on my work by email, phone or in person, when I visited Heidelberg. Thank you for commenting on my work from the perspective of a physicist who had not been exposed to snow physics before.
- *Prof. Bernd Jähne* who agreed to be the second referee for my thesis.
- *Dr. Sophia Haussener* at the ETH Zurich for the collaboration and applying the CTMC ray-tracing model to various snow samples.
- *Richard Brandt* at the Atmospheric Science Department of the University of Washington for sending his results of single-scattering Mie calculations, which are used as input to multiple-scattering calculations throughout this thesis.